ISBN 978-82-326-4628-9 (printed ver.)
ISBN 978-82-326-4629-6 (electronic ver.)
ISSN 1503-8181

Abbas Lotfi

Doctoral thesis

Doctoral theses at NTNU, 2020:140

Abbas Lotfi

Off-core Magnetic Flux Paths in Power Transformers

Modeling and Applications

NTNU
Norwegian University of Science and Technology
Thesis for the Degree of
Philosophiae Doctor
Faculty of Information Technology and Electrical Engineering
Department of Electric Power Engineering

Doctoral theses at NTNU, 2020:140

NTNU

NTNU
Norwegian University of
Science and Technology

NTNU
Norwegian University of
Science and Technology

Abbas Lotfi

Off-core Magnetic Flux Paths in Power Transformers

Modeling and Applications

Thesis for the Degree of Philosophiae Doctor

Trondheim, May 2020

Norwegian University of Science and Technology
Faculty of Information Technology and Electrical Engineering
Department of Electric Power Engineering

NTNU
Norwegian University of
Science and Technology

NTNU
Norwegian University of Science and Technology

Thesis for the Degree of Philosophiae Doctor

Faculty of Information Technology and Electrical Engineering
Department of Electric Power Engineering

ISBN 978-82-326-4628-9 (printed ver.)
ISBN 978-82-326-4629-6 (electronic ver.)
ISSN 1503-8181

Doctoral theses at NTNU, 2020:140

Printed by NTNU Grafisk senter

Preface and Acknowledgement

This dissertation is submitted for the degree of philosophiae doctor at the Norwegian University of Science and Technology (NTNU) in Trondheim. The research described herein was conducted under the supervision of Professor Hans Kristian Høidalen in the Department of Electric Power Engineering, NTNU, between April 2012 and October 2015.

The PhD work has been a part of the KMB project 'Electromagnetic Transients in Future Power Systems' supervised by SINTEF Energy Research and financially supported by Norwegian Research Council and the partners including Dong Energy (Denmark), Nexans Norway, Edf (France), EirGrid (Ireland), Hafslund Nett (Norway), National Grid (UK), RTE (France), Statkraft (Norway), Statnett (Norway) and Vestas Wind systems (Denmark).

A special debt of gratitude is owed to my supervisor, Professor Hans Kr. Høidalen, for his trust in giving me this opportunity and his excellent guidance and insightful supervision during my doctoral studies.

I also wish to thank the KMB project partners' representatives for helpful comments during my presentations held in regular workshops of the project. I would like to mention the project manager Dr. Bjørn Gustavsen (chief scientist at SINTEF Energy Research) for his wonderful cooperation.

I was fortunate enough to have a visit to Møre Trafo AS, a manufacturing company located in Sykkyven in Møre og Romsdal, to discuss on the tank design, and to learn about the typical structural steels used in power transformers. I would like to take this occasion to acknowledge Mr. Nemanja Grubor from the technical department of the Møre Trafo AS for valuable discussions and for providing me with samples of typical tank steels.

I must also express my particular thanks to Professor Arne Nysveen, Professor Bruce Mork (guest professor from Michigan Technological University, USA) and Dr. Ebrahim Rahimpour (R&D principal engineer and project manager at ABB AG) for their generous help and insightful comments.

I also benefited from debating issues with my friends and fellow PhD students at the electric power engineering department specially Dr. Edris Agheb; Thank you for all our useful discussions.

My parents as well as my brother and sisters deserve a particular note of thanks: your wise counsel and kind words have, as always, served me well.

Finally, and by no means last, I would express my heartfelt thanks to my beloved wife, Zohreh, for her endless love, unwavering support, patience and understanding.

Trondheim, May 2020

Abbas Lotfi

To:

My Father

who was always inspiring and supporting me to pursue my studies. He passed away when I was at year 3 of my PhD study. Dad… I accomplished my mission,

THANK YOU for everything

My Mother

whose love, encouragement and prayers of day and night have made me able to achieve such success and honor

Abstract

Zero sequence (ZS) characteristics of transformers are of great importance in some circumstances including unbalanced and DC biased operations. Any unbalanced condition in the voltage supplying a transformer or in the load to be supplied can result in ZS currents assuming that at least one of the windings is Y-connected and grounded. An example of DC biasing conditions is a transformer subjected to geo-magnetically induced current (GIC) because of geo-magnetic disturbances of the earth's magnetic field due to solar activities. In the case of 3-phase, 3-legged transformers, the ZS flux takes the path off the core including the oil gaps, structural steels and the tank walls.

The tank is made from mild steel, which is several hundred times more magnetically permeable than the oil. This means that the tank's presence will disturb the flux distribution in the oil gap depending on its relative proximity to the active part. The flux reaching the wall will enter and exit through continuously distributed points making it complicated to determine the wall's effective height and thickness. In addition, the losses in the tank may increase the temperature and thus affect the electric conductivity of the tank steel, leading to a negative feedback on the losses and positive feedback on the magnetic penetration depth.

Although there have been extensive advancements in the core and the windings modeling, the off-core flux path has not been properly represented in the dual circuit models of 3-phase, 3-legged power transformers. Differences between the ZS impedances seen from different windings of a transformer, as reported in the experimental results, have not been considered in the models presented so far. As repeatedly reported in the literature, there has been a lack of information on the electromagnetic properties of the tank steel including the electric conductivity and magnetic characteristics. As mentioned, the temperature rise in the tank affects both the ZS impedance and the losses; however, thermal models presented in the literature primarily address the oil and the winding temperature rises with much less focus on the tank. Furthermore, considerations on the tank design such as the use of magnetic shunts, magnetic shields, and choosing from plain and corrugated walls that influence the off-core flux path, have not been discussed properly in the previous works. In cases when the tank losses are not of interest, the tank can be represented with proper boundary conditions. Which of the flux-normal or flux-tangential boundary conditions is more accurate in the representation of the tank has also not been discussed in the previous research works.

The main contribution of the current PhD thesis is to address the abovementioned challenges and research gaps in the off-core flux path modeling. The thesis has introduced an electromagnetic/thermal model for the off-core flux path. The electromagnetic model consists of linear inductances (representing the oil gap) and non-linear R-L branches (representing the tank). The non-linear branches are Cauer-like equivalent circuits obtained from finite difference approximation of the magnetic diffusion equation. The thermal model is based on the thermal network method assuming that the temperature drop across the tank thickness is negligible. Hence, the tank is considered as a thermal node connected to non-linear thermal resistances representing convective and radiative heat transfer from the tank.

All the equations governing the electromagnetic and thermal equivalent circuits are implemented in MATLAB-SIMULINK. However, to simulate target applications including transformers under unbalanced conditions and transformers subjected to the GIC, the equivalent circuits are drawn in ATPDraw and are solved with the EMTP-ATP program.

Difficulties in the calculation of the model parameters are discussed in detail using finite element analysis (FEA) of simple 2D models of the off-core flux path. The FEA provides an advantage that the different parameters can be thoroughly studied without influence from unknown factors. For example, the temperature impact may not be considered adequately when studying the model parameters based only on experimental results. In addition, the significance of the tank walls, cover and bottom as well as the temperature can be separately studied under controlled case studies. As investigated in the thesis, the wall and bottom are significant for the off-core flux path; however, the cover can be neglected when its distance to the core is large and typically more than 2.5 times the distance from the wall to the core. At high off-core flux, when the wall becomes magnetically saturated, the open-circuit ZS impedance starts decreasing due to the reduction in the magnetic permeability. However, the temperature rise in the wall will affect the electric resistivity, thus having an increasing impact on the impedance. In some cases such as the corrugated walls (where the wall resistance is relatively higher than the plain walls), the temperature impact may keep the open-circuit ZS impedance almost constant.

It is shown that the effective tank height, the wall thickness and electric conductivity and the linear inductances (representing the oil gap) need to be tuned in order to reproduce the impedance and losses measured on a 3-phase 3-legged 300 kVA sample transformer. These tuning factors are identified by fitting the circuital model to either test or FEM results. As demonstrated in the thesis, there is no need to re-tune the parameters when the temperature of the tank elements varies in a practical range as observed in the actual operations.

Characterization of the electromagnetic properties of the tank steel in terms of the magnetization curves and the losses is performed using extensive magnetic measurements as a part of the PhD work. As discussed in the thesis, classical eddy current loss is the dominant component for the tank steels thicker than 4 mm. However, the excess losses must also be considered in the thinner walls, which are normally used in corrugated tank walls.

In cases the tank losses are not of interest, and in order to reduce the model complexity, lossless variations of the proposed model can be used. In the lossless variations, the tank is excluded and proper boundary conditions are set instead. As investigated, the corrugated walls as well as the walls equipped with magnetic shunts can be assumed as a flux-normal boundary condition. The plain walls as well as the walls equipped with magnetic shields can be assumed as a flux-tangential boundary condition. The bottom as a base of transformer is made from relatively thick steel that can be considered as a flux-tangential boundary condition.

The difference between ZS impedances seen from HV and LV depends on the behavior of the tank walls. As discussed in the thesis, the ZS impedance difference can be small in corrugated walls as well as walls equipped with magnetic shunts, but it is large for plain walls and even larger in cases where the walls are equipped with magnetic shields.

Table of Contents

Preface and Acknowledgement ..... **i**

Abstract ..... **v**

Table of Contents ..... **vii**

List of Symbols ..... **xi**

List of Figures ..... **xv**

List of Tables ..... **xxi**

Introduction **1**

1.1 Motivations 1

1.2 Scope of work 4

1.3 Research context 5

1.4 Thesis structure 5

1.5 List of publications 7

Background **9**

2.1 Method of symmetrical components 9

2.2 Dual circuit model of transformer, the off-core flux path 11

2.3 Thermal modeling of the tank walls 14

2.4 Research gaps in the off-core flux path models 14

Modeling of the off-core flux path **15**

3.1 Electromagnetic modeling 15

3.1.1 Electrical equivalent circuit of the tank wall 17

3.1.2 Implementation of the tank model in MATLAB-SIMULINK 19

3.1.3 Excess losses 21

3.2 Thermal modeling 23
3.2.1 Thermal equivalent circuit 23
3.2.2 Calculation approach of the thermal characteristics 25
Tests and measurements 31
4.1 Electric and magnetic measurements on tank steel 31
4.1.1 DC energy losses 33
4.1.2 Dynamic losses 34
4.1.3 Electrical conductivity measurements 37
4.1.4 Analytical formula for excess losses 38
4.1.5 Characterization of the dynamic losses 39
4.1.6 Temperature impact on the conductivity 44
4.1.7 The wall corrugation impact on the conductivity 44
4.2 Zero sequence impedance tests on Unit 1 and Unit 2 45
Evaluations and discussion on the parameters 49
5.1 Parameters of the oil gaps (Linear inductances) 49
5.1.1 Calculation of L_1 50
5.1.2 Calculation of L_2, L_3, L_4 and L_5 50
5.1.3 Calculation of the terminal inductances ($\boldsymbol{LT}, \boldsymbol{i}$) using 3D-FEM 50
5.1.4 Considerations on the off-core terminal inductances 51
5.1.5 Considerations on the off-core inductances - Case 2 56
5.1.6 Impact of the tank presence 57
5.2 Parameters of the tank model 62
5.2.1 Considerations on the wall parameters 63
5.2.2 Considerations on the bottom parameters 68
5.2.3 Temperature impact 73
5.3 Winding radial position: impact on the off-core inductance 75
Benchmarking of the off-core model of Unit 1 77
6.1 OC-ZS characteristics 77
6.1.1 Lossless variations 77
6.1.2 The complete model 79
6.2 SC-ZS characteristics 85
Applications 89
7.1 DC biased operation of transformers 89

7.1.1 The wall magnetization - AC excitation with DC offset 89
7.1.2 Simulation of Unit 1 subjected to GIC 92
7.2 Unbalanced operation of 3-phase transformers 100
7.2.1 Unbalanced simulation of Unit 1 102
Conclusions and future works 107
8.1 Conclusion 107
8.2 Future works 111
Bibliography 113
Appendix 1 123
Appendix 2 125
Appendix 3 129

List of Symbols

$2D$	Two-dimensional
$3D$	Three-dimensional
A	Cross sectional area of heat transfer
AC	Alternating current
B	Flux density
B_a	Space average flux density
B_i	Magnetic flux density at the i^{th} layer
B_m	Maximum flux density
B_r	Residual flux density
CCP	Common connection point
c_p	Specific heat capacitance of the tank
C_t	Thermal capacitor of the tank
DC	Direct current
E	Electric field intensity
e_i	Voltage of the i^{th} node
f_{BH}	B-H Normal curve (single value)
F_{f-surr}	Reflection factor
FEA	Finite element analysis
FEM	Finite element method
$g(B)$	Excess losses coefficient (microscopic)
$g'(B)$	Excess losses coefficient (macroscopic)
g	Acceleration due to the gravity
GIC	Geo-magnetically induced current
Gr	Grashof number
GMD	Geomagnetic disturbances
h	Thickness of the wall sub-divisions
H_C	Coercive force (demagnetization flux intensity)
h_{corr_conv}	Convective heat transfer coefficient of corrugated wall
h_{conv}	Convective heat transfer coefficient
H_f	Height of the fins in corrugated walls
H_{exc}	Excess losses flux intensity
H_{a_exc}	Macroscopic magnetic field of excess losses
H_i	Magnetic flux intensity at i^{th} layer

$\bar{H}_s$	Ratio between the fin height and the fin spacing
h_t	Wall height (effective)
h_r	Radiation coefficient of plain plate
$h_{r,fin}$	Radiation coefficient of corrugated plate
HV	High voltage winding
i_{cl}	Classical eddy current
i_{exc}	Excess losses current
i_i	Current induced in layer i^{th}
i_t	Current induced in the tank
K_h	Hysteresis coefficient
L_{0t}	Inductance of air beyond the wall
$L_1, \dots L_s$	Linear inductances of the off-core path
L_c	Characteristic length
L_{LH}	Leakage inductance between windings
L_{LC}	Inductance of the space between the inner winding and the core
$\bar{L}_s$	Ratio between the characteristic length and the fin spacing
$L_{T,i}$	Off-core terminal inductance for Case *i*
l_t	Length of the tank wall
LV	Low voltage winding
n	Number of the wall thickness subdivisions
N	Turn number of the winding
Nu	Nusselt number
Nu_V	Nusselt number of vertical wall
Nu_s	Nusselt number of corrugated wall
n_f	Number of the fins
OC-ZS	Open-circuit zero sequence
P_{dyn}	Dynamic losses
P_{hys}	Hysteresis losses
Pr	Prandtl number
P_t	Tank losses
P_{tot}	Total losses
Q	Heat dissipated
$Q_{amb_{conv}}$	Convective heat dissipated from the wall to the ambient
$Q_{amb_{rad}}$	Radiative heat dissipated from the wall to the ambient
Q_{fin}	Radiative heat dissipated from each radiator
$Q_{oil_{conv}}$	Convective heat dissipated from the wall to the oil

R	Resistance of the layer i^{th}
ℜ	Magnetic reluctance
$ℜ_{ot}$	Magnetic reluctance of the air beyond the wall
Ra	Rayleigh number
Ra_S	Rayleigh number of the fins
rms	Root mean square
S	Fins separation of corrugated walls
SST	Single sheet measuring sensor
SC-ZS	Short-circuit zero sequence
T_{amb}	Ambient temperature in K
t_d	Tank wall thickness
T_t	Tank temperature in K
T_{or}	Radiative thermal resistance-outer surface of the wall
T_{oc}	Convective thermal resistance-outer surface of the wall
T_i	Convective thermal resistance-inner surface of the wall
V_t	Voltage induced in the tank walls
Vol_t	Volume of the tank
ZS	Zero sequence
α_{20}	Temperature coefficient of electric conductivity at 20 °C
β	Coefficient of thermal expansion
γ	Kinematic viscosity
ϵ	Emissivity
θ_{amb}	Ambient temperature in °C
θ_f	Fluid temperature in °C
θ_m	Average wall-ambient temperature in °C
θ_{oil}	Oil temperature in °C
θ_t	Tank wall temperature in °C
k	Thermal conductivity
λ_i	Flux-turn in the layer i^{th}
μ	Magnetic permeability
μ_0	Permeability of the free space
℘	Magnetic permeance (inverse of the reluctance)
ρ	Density of the coolant
ρ_t	Density of the tank steel
σ	Electric conductivity
σ_B	Stefan-Boltzman's constant

φ_{0t}	Magnetic flux beyond the tank wall
φ_w	Magnetic flux into the wall
ω	Angular frequency

List of Figures

Figure 2.1 Topologically correct equivalent circuit of 3-phase 3-legged transformers based on duality transformation 11
Figure 3.1 Off-core flux path, equivalent dual circuit development 16
Figure 3.2 Overall dual circuit model of a 3-phase, 3-legged transformer including the off-core flux path model 16
Figure 3.3 Electric and magnetic field orientation assumed for the tank walls 17
Figure 3.4 Realization of: a) inner b) middle, and c) outer layer of the discretized tank wall 19
Figure 3.5 Detailed equivalent circuit of the tank elements 19
Figure 3.6 Implementation of the discretized model of the tank in MATLAB-SIMULINK, 'sigma' is the tank steel conductivity denoted with σ in the formulations 21
Figure 3.7 Equivalent circuit of the tank wall including the excess losses model 23
Figure 3.8 Heat transfer through the wall, the θoil and $\theta amb$are the oil and ambient temperatures 24
Figure 3.9 Thermal equivalent circuit of the wall 24
Figure 3.10 Implementation of thermal model in MATLAB-SIMULINK, Left: the overall block, Right: the governing equations implementation inside the Thermal Model block 25
Figure 3.11 Convection heat transfer from the wall surface 26
Figure 3.12 Heat transfer coefficient for vertical wall cooled-off with air-natural convection 28
Figure 3.13 Radiation heat transfer coefficient, markings: calculated values, dashed trace: fitted by $aeb\Delta\theta$ with parameters $a = 5.475$ and $b = 0.0049$. 29
Figure 3.14 Computation of initial wall temperature based on oil and ambient temperature inputs 30
Figure 4.1 Specimens of the tank steels with thicknesses of 1.25 mm (Left), 4 mm (Middle) and 6 mm (Right) 31
Figure 4.2 The equipment used for the measurements: a) the tester MPG 100D, and b) the SST 32
Figure 4.3 Hysteresis loops: Left: static, Right: dynamic (50 Hz), for the 1.25 mm thick sample 32
Figure 4.4 Hysteresis loops, Left: static, Right: dynamic (50 Hz) for the 4 mm thick sample 33
Figure 4.5 Magnetic normal curves, Left: the 1.25 mm thick sample, Right: the 4 mm thick sample 33
Figure 4.6 Static hysteresis loops of the 1.25 mm (dashed trace) and the 4 mm (solid trace) samples 34
Figure 4.7 Energy losses corresponding to static hysteresis loops, measured values and fitted curves 34
Figure 4.8 Dynamic hysteresis loops for the 4 mm thick sample 36

Figure 4.9 Total losses, Left: for the 4 mm thick sample, Right: for the 1.25 mm thick sample 36
Figure 4.10 The ratio between the dynamic losses and the total losses 36
Figure 4.11 Temperature of the specimens during magnetic measurements, Left: for the 1.25 mm sample Right: for the 4 mm sample 37
Figure 4.12 Conductivity measurement, Right: test setup, Left: V-I characteristics measured for the 4 mm thick sample 37
Figure 4.13 Excess losses for the 4 mm samples (Left) and the 1.25 mm sample (Right) - 'Fitted 1' is based on $Pexc = kBmn/(1 + aBm + bBm2)$, 'Fitted 2' is based on $Pexc = kBmn$ 38
Figure 4.14 Simple model of the SST for reproducing the measured dynamic losses 40
Figure 4.15 Distribution of the flux density across the half thickness of the 4 mm sample at frequency 50 Hz, black solid trace is the average flux density (Ba) across the sample thickness 41
Figure 4.16 Classical eddy current losses calculated for the 4 mm sample, markings are the total dynamic losses from the measurement, dashed trace is the losses with no conductivity temperature correction, solid trace is the eddy current losses with the conductivity corrected by temperature 41
Figure 4.17 Classical eddy current losses calculated for the 1.25 mm sample, blue-markings are the total dynamic losses measured; green-dashed trace is the losses with no conductivity temperature correction; red-solid trace is the eddy current losses with the conductivity corrected by temperature 42
Figure 4.18 Total dynamic losses of the 1.25 mm sample at 50 Hz, blue-markings are the measured losses 42
Figure 4.19 Excess losses coefficient as a function flux density for the 1.25 mm sample at 50 Hz, red-markings are from simulation results, blue-dashed line is the fitted by $aBm2 + bBm + c$ 42
Figure 4.20 The total dynamic losses, measured against the simulated losses components of the 1.25 mm sample at 50 Hz, blue-markings are the measured and the red-dashed trace is the simulated 43
Figure 4.21 Left: The excess losses coefficient gB as a function of induction where red-markings are simulated and blue-dashed is the fitted, Right: Total dynamic losses, blue-markings are the measured and the red-dashed trace is the simulated for the 4 mm sample at 50 Hz 43
Figure 4.22 Wall steel conductivity as a function of temperature 44
Figure 4.23 The corrugated tank wall, the path of current induced in the wall 45
Figure 4.24 Test circuits for zero-sequence impedance measurements [23] 46
Figure 4.25 OC-ZS impedance and losses of Unit 1 measured at the LV side (Right) and HV side (Left) 47
Figure 4.26 OC-ZS inductance seen from the LV side (solid trace) and HV side (referred to LV and shown as dashed trace) of Unit 1 47
Figure 4.27 SC-ZS impedance seen from the HV side (LV short-circuited) - Unit 1 47
Figure 5.1 The off-core equivalent circuit 49
Figure 5.2 Left: 3D model of Unit 2, Right: the meshing of the model 52

Figure 5.3 The relative difference (%) between the off-core inductances seen from HV and LV sides 53
Figure 5.4 Flux lines for each simulation case and excitation side 54
Figure 5.5 The FEM model for investigating radial displacement of the winding 55
Figure 5.6 The results for radially displaced winding simulations (Figure 5.5) 55
Figure 5.7 The model used for studying the winding thickness 55
Figure 5.8 The off-core inductance versus winding thickness for each simulation case 56
Figure 5.9 The flux paths for LV and HV sides in Case 2 and their geometrical difference 56
Figure 5.10 The off-core circuit improved for Case 2 57
Figure 5.11 The off-core inductance (reference to model Figure 5.5 with the wall set to impedance boundary condition as well as the bottom and cover to flux-tangential boundary condition) versus the wall relative permeability at different wall electric conductivity ($\sigma_1>\sigma_2 \ldots>\sigma_7$) 58
Figure 5.12 The off-core inductance (reference to model Figure 5.5 with the wall set to impedance boundary condition as well as the bottom and cover to flux-tangential boundary condition) versus relative permeability for the tank steel conductivity at different temperatures (reference to Table 5.4 and Table 5.5) 59
Figure 5.13 Left: definition of $ratio_{cw}$ defined as *ds*/*(Core height-Winding height)*, Right: the off-core inductance versus the wall permeability at different tank wideness ratios, $ratio_{cw1}<ratio_{cw2}<ratio_{cw3}<ratio_{cw4}$ (at a sample conductivity of 6410 kS/m) 60
Figure 5.14 Upper (wall is set to flux-normal boundary condition) and lower (wall is set to flux-tangential boundary condition) limit inductances versus of $ratio_{tw}$ defined as *ds*/(*Core height-Winding height*) 60
Figure 5.15 The off-core inductance at various Core-Cover relative gap 61
Figure 5.16 The off-core inductance as a function of relative permeability of the bottom at a sample conductivity of 6410 kS/m; the wall is set to normal boundary condition 62
Figure 5.17 The off-core inductance as a function of the wall's relative permeability, σw is the wall conductivity, the bottom relative permeability is 200 (red-dashed trace) and 1000 (blue-solid trace), $ratio_{cw}$=0.3 (Left) and $ratio_{cw}$=0.8 (Right). 62
Figure 5.18 Flux enters and exits through several points 63
Figure 5.19 Simple 2D model including the wall as non-linear steel 64
Figure 5.20 The off-core equivalent circuit of the model shown in Figure 5.19 64
Figure 5.21 Implementing of the circuital equations of Figure 5.20 in MATLAB-SIMULINK 65
Figure 5.22 Impedance seen from LV side, $ratio_{cw}$=0.3, the wall conductivity: 6410 kS/m 65
Figure 5.23 Losses seen from LV side, $ratio_{cw}$=0.3, the wall conductivity: 6410 kS/m 65
Figure 5.24 Impedance seen from LV side, $ratio_{cw}$=0.3, red markings: from FEM, dashed traces: from equivalent circuit results with ht= 0.57 m at different wall conductivity 66
Figure 5.25 Losses seen from LV side, $ratio_{cw}$=0.3, red markings: from FEM, dashed traces: from equivalent circuit results with ht= 0.57 m at different wall conductivity 66
Figure 5.26 Impedance seen from LV side, $ratio_{cw}$=0.3, red markings: from FEM, dashed trace: from equivalent circuit results with ht= 0.7 m and L_2 is increased by a factor of 1.15 67

Figure 5.27 Losses seen from LV side, $ratio_{cw}$=0.3, red markings: from FEM, dashed trace: from equivalent circuit results with ht= 0.7 m and L_2 is increased by a factor of 1.15 67
Figure 5.28 The impedance and losses (LV side) at wall conductivity of 6410 kS/m, wider variation, red markings: from FEM, dashed trace: from equivalent circuit results with ht=0.65 m and L_2 increased by a factor of 1.15..... 68
Figure 5.29 The impedance and losses (LV side) as function of wall conductivity, wider variation at voltage 30 V, red markings: from FEM, black-dashed trace: from equivalent circuit results with ht = 0.65 m and L_2 increased by a factor of 1.15 68
Figure 5.30 The simple 2D model including the bottom 69
Figure 5.31 Equivalent circuit of the model shown in Figure 5.30, the cover is short-circuited due to the tangential boundary condition 70
Figure 5.32 The off-core impedance (Left) and losses (Right) as a function of voltage, the model of Figure 5.30 - Variation 1 (see Table 5.9)..... 70
Figure 5.33 The off-core impedance (Left) and losses (Right) as a function of voltage, the model of Figure 5.30 - Variation 2 (see Table 5.9)..... 70
Figure 5.34 The tank bottom's influence on the off-core impedance and the losses for Variation 1, electric conductivity of 996 kS/m for Wall and 6410 kS/m for Bottom, dashed trace: Bottom thickness is 4 mm, solid trace: Bottom thickness is 10 mm, dotted-dashed trace: no Bottom..... 71
Figure 5.35 The tank bottom's influence on the off-core impedance and losses for Variation 2, electric conductivity of 996 kS/m for Wall and 6410 kS/m for Bottom, dashed trace: Bottom thickness 4 mm, solid trace: Bottom thickness 10 mm, dotted-dashed trace: no Bottom 72
Figure 5.36 The tank bottom's influence on the off-core impedance and losses for Variation 1, electric conductivity of 6410 kS/m for both Wall and Bottom, dashed trace: Bottom thickness 4 mm, solid trace: Bottom thickness 10 mm, dotted-dashed trace: no Bottom 72
Figure 5.37 The tank bottom influence on the off-core impedance and losses for Variation 2, electric conductivity of 6410 kS/m for both Wall and Bottom, dashed trace: Bottom thickness 4 mm, solid trace: Bottom thickness 10 mm, dotted-dashed trace: no Bottom 72
Figure 5.38 Hear transfer coefficient of Left: Ambient air convection coefficient (solid curve), Radiation from Wall outer surface (dashed curve) Right: Transformer oil convection coefficient 73
Figure 5.39 The off-core impedance and losses of the model Figure 5.19, $ratio_{cw}$=0.3 taking the thermal model into calculation, solid trace: no thermal model included, dashed trace: Oil temperature is 55 °C, dotted-dashed: Oil temperature is 30 °C 73
Figure 5.40 Dynamic response of Wall temperature at Voltage of 30 V and Oil temperature of 55 °C (dashed trace) and 30 °C (solid trace)..... 74
Figure 5.41 The off-core impedance and losses for the model Figure 5.19, $ratio_{cw}$=0.3 with Wall conductivity of 996 kS/m, solid trace: no thermal model included, dashed trace: thermal model included with Oil and Air temperature of 55 °C and 20 °C, respectively..... 74

Figure 5.42 Relative inductance of the displaced winding based on inductance at $dx = 0$, for the wall conductivity of 996 kS/m (dashed trace) and 6410 kS/m (solid trace) 75
Figure 5.43 Upper (wall is set to flux-normal boundary condition) and lower (wall is set to flux-tangential boundary condition) limit inductances versus of $ratio_{tw}$ defined as *ds*/(*Core height-Winding height*) for the case where the excited winding is radially shifted by 50% towards the wall 76
Figure 6.1 Off-core inductances of the lossless models in comparison to the OC-ZS inductance measured at the LV-side of Unit 1 78
Figure 6.2 Off-core inductances of the lossless models in comparison to the OC-ZS inductance measured at the HV-side of Unit 1 79
Figure 6.3 An illustration of bottom dimension and average path of the induced current 80
Figure 6.4 Heat transfer of each surface of the wall and the bottom 82
Figure 6.5 Heat transfer coefficients of the wall, Left: Outer surface, Right: Inner surface .. 83
Figure 6.6 Heat transfer coefficients of the bottom, solid trace: Inner surface, dashed trace: Outer surface 83
Figure 6.7 The model results in terms of the off-core impedance (Left) and losses (Right), LV side 83
Figure 6.8 Temperature of the wall (Right) and the bottom (Left), LV side 84
Figure 6.9 Influence of the oil temperature on calculated impedance and losses - LV side, the oil average temperature equals to 20 °C for both wall and bottom thermal models (solid traces), the oil average temperature is 55 °C for the wall thermal model and the bottom oil temperature is 40 °C for the bottom thermal model (dashed curve) 84
Figure 6.10 The model results in terms of the off-core impedance (Left) and losses (Right), HV side 84
Figure 6.11 Illustration of SC-ZS impedance seen from LV, the off-core path connects parallel to the HV winding resistance (colored red) 85
Figure 6.12 Illustration of SC-ZS impedance seen from HV, the off-core path connects parallel to series impedance of the leakage inductance and the LV winding resistance (colored red). 86
Figure 6.13 SC-ZS impedance seen from HV side (LV short-circuited) - Unit 1 87
Figure 7.1 The circuit (top) considered for DC magnetization of the wall and its implementation (bottom) in MATLAB-SIMULINK 90
Figure 7.2 Wall magnetization current (Left), Wall eddy current induced - Inner surface (Right) at B_m=1 T, GIC=15 A, Conductivity=6410 kS/m 91
Figure 7.3 Wall magnetization current (Left), Wall eddy current induced - Inner surface (Right) at B_m= 0.1 T and GIC = 15 A, Conductivity = 6410 kS/m 91
Figure 7.4 Wall losses at different GIC and B_m amplitudes (Left). Variation of the losses at different GIC frequencies when GIC is considered as a sinusoidal voltage source with an amplitude of 20 A positively shifted to give a DC component of 20 A, and B_m = 1 T (Right) 91
Figure 7.5 System topology used in the simulations 92
Figure 7.6 Left: Foster equivalent circuit, Right: AC resistance of the LV winding vs. frequency 93

Figure 7.7 Left: Core equivalent circuit, Right: Magnetization characteristics of the core (Unit 1) 93
Figure 7.8 The dual circuit model implemented in ATPDraw for GIC simulations 94
Figure 7.9 Magnetizing current at different levels of GIC 95
Figure 7.10 The effective (rms) values of magnetizing current as a function of GIC levels 95
Figure 7.11 Harmonic content of the transformer magnetizing current 96
Figure 7.12 Distribution of voltage (Bottom) and current (Top) induced in the walls at GIC=100 A 96
Figure 7.13 The wall and the bottom magnetizing current - Innermost layer at GIC=100 A 97
Figure 7.14 The current induced in the wall and bottom - Innermost layer at GIC=100 A 97
Figure 7.15 Frequency spectrum of the wall magnetizing (Blue bars) and eddy currents (Red bars) in the innermost layer, GIC=100 A 98
Figure 7.16 Currents of the inductors L_1 (Left) and L_2 (Right) 98
Figure 7.17 Reactive power of Unit 1 versus GIC 99
Figure 7.18 Magnetizing current (rms) versus GIC 99
Figure 7.19 Active power seen from LV side versus GIC 99
Figure 7.20 Apparent power seen from LV side at different GIC levels 99
Figure 7.21 The ZS flux path depending on which winding drives the ZS current, Left: Inner winding supplies the ZS current, Right: Outer winding supplies the ZS current 100
Figure 7.22 The model of Unit 1 implemented in ATPDraw - Only the wall and the bottom are considered since the cover has no impact (as discussed in Chapter 5) 103
Figure 7.23 Single phase to ground short circuit at the primary side, I0_Primary (green dotted-dashed) and I0_Secondary (red-dashed) compared to the off-core path current (blue solid) 104
Figure 7.24 Single phase to ground fault at the secondary side, I0_Primary (green dotted-dashed) and I0_Secondary (red-dashed) compared to the off-core path current (blue solid) 104
Figure 7.25 Zero sequence currents of the primary (dotted-dashed) and secondary (dashed) sides compared to the off-core path current (solid), Left: single-phase half-load, Right: Single-phase half-voltage 105
Figure 7.26 The off-core path currents in scenarios half-load (solid red) and half-voltage (dashed blue) 105
Figure 8.1 Future developments of the off-core model proposed in the thesis to include the core clamps, tie bars, magnetic shields and magnetic shunts 112

List of Tables

Table 4.1 Fitting parameters of the hysteresis losses function 33
Table 4.2 Coefficients of the Excess Loss found by fitting 38
Table 4.3 Fitting parameters for excess losses coefficients 43
Table 4.4 Characteristics of the sample transformers 46
Table 5.1 Calculation formulas of linear inductances 50
Table 5.2 Energy error obtained in 3D-FEM simulations 52
Table 5.3 The off-core terminal inductances 53
Table 5.4 Summary of electric conductivity for the 4 mm thick steel sample 58
Table 5.5 Summary of electric conductivity for the 1.25 mm thick steel sample 59
Table 5.6 Transition relative permeability from tangential-like to normal-like wall 61
Table 5.7 Linear inductances for different variations of the model shown in Figure 5.19 64
Table 5.8 Tuning factors of the circuit parameters of the model shown in Figure 5.19 68
Table 5.9 Off-core inductances seen from LV side of the model in Figure 5.32 69
Table 5.10 Linear inductances of the off-core equivalent circuit 69
Table 5.11 The tuning factors of the equivalent circuit parameters 71
Table 6.1 Linear inductances of the off-core path for Unit 1 79
Table 6.2 Physical and structural data of Unit 1 to be used in the modeling of off-core flux path 80
Table 6.3 Heat transfer equations used for different surfaces of the tank 82
Table 6.4 Tuning factors resulting from fitting to measurements of LV and HV sides 83
Table 6.5 SC-ZS impedance calculated with the equivalent circuit for Unit 1 86
Table 6.6 Comparison of SC-ZS inductances calculated with 3D-FEM and equivalent circuit 87
Table 7.1 Zero sequence current path for loaded transformer, the HV (outer winding) side is considered secondary connected to the load, and LV side (inner winding) is considered primary connected to the network through Z_S 101

Chapter 1

Introduction

1.1 Motivations

Transformers experience different mechanical, electrical and thermal stresses during normal operations as well as abnormal undesirable conditions in their lifetime. Appropriate modeling of transformers is essential in order to

- optimize transformer design against the stresses they experience during the lifetime;
- simulate the consequences of undesirable conditions prior to their occurrence and consider proper measures of protections.

Three-phase power transformers are basically designed to operate with symmetrical 3-phase voltages applied to the primary windings and 3-phase symmetrical load connected to the secondary windings [1] [2]. With this design principle, the magnetic flux is supposed to be confined in the core as a high magnetically permeable material at no-load condition, and in the leakage channel between primary and secondary windings at loading condition. However, there is always some fringing flux taking off-core paths beyond the outermost winding through the oil-gap and the tank walls. This so-called off-core flux is considerably higher in 3-legged core design as well as when symmetry assumptions for the voltage applied (primary side) or the load supplied (secondary side) are no longer valid.

Both the primary-side voltage unbalanced and the secondary-side load unbalanced conditions can result in zero sequence (ZS) currents, which are equal in magnitude and synchronized, if there is a return electric path for them that can be provided through

grounded Y-connected windings. The ZS flux generated due to the ZS currents in each leg of the core has the same amplitude and direction. Hence, the flux does not complete its path inside the 3-legged core and is forced to flow outside through the off-core path. The off-core flux has undesired thermal effects on the transformers due to the losses in the metallic parts of the path including the tie bars, core clamps and the tank walls that must be taken into consideration in the ZS modeling.

Besides this, physical location of the winding (that can be inner or outer winding) driving the ZS current as well as magnetic coupling between the phases through the tank walls affect the off-core flux, which complicates the modeling of transformers from the ZS point of view.

It is worth mentioning that asymmetric earth faults (such as single line to earth fault) occurring on either primary or load sides, are of extreme cases of primary-side or secondary-side unbalanced conditions, respectively. In order to obtain a reasonably accurate calculation results for transformers under the earth faults, a proper electromagnetic/thermal representation of the off-core flux path is of great importance.

In addition, the off-core flux can be induced from a secondary (normally unwanted) voltage source connected to either winding. An example of this situation is Geo-magnetically Induced Current (GIC) from a Geo-Magnetic Disturbances (GMD) [3] [4] [5] [6] [7]. GMD is basically due to the highly energetic charged particles ejected from the sun's activity (which is called Coronal Mass Ejection CME) traveling in the surrounding space. This jet of plasma hits the earth and can distort the earth's magnetic field. This fluctuations of the earth's magnetic field is a slow phenomenon; however, the time varying nature will induce electric potential on the earth's surface (and any manmade loop of conductors such as electric transmission lines). The electric potential difference between two locations on the earth's surface causes a near-DC current that is so-called GIC. GIC varies up to hundreds of amps and has relatively low frequency typically in the order of 0.1 Hz to 0.001 Hz [7].

GIC affects systems in the regions near to the earth's magnetic poles (higher latitude countries) and follows the 22-year solar cycle with peaks once during the 11-year half cycle [8] [9]. GIC will flow into the transmission lines through the grounded points of Y-connected transformer windings. The magnitude of the GIC depends on the magnitude of the induced surface electric potential, the orientation of the transmission line and the DC (resistive network) characteristics of the power system. It has been repeatedly reported that the transformers are the most vulnerable equipment in a power system subjected to GIC.

GIC will affect transformer operation, as explained in the following.

1. The quasi-DC current of GIC will generate DC flux in the core. The magnitude of the DC flux depends on the GIC magnitude and the reluctance of the DC flux path. Since the GIC is in the same direction at the all phases, the DC flux path is in fact the same as the ZS flux path.

2. The DC flux will be superimposed to the AC flux causing an offset of the main flux.

3. Shifting the main flux on the magnetization characteristics, the core is saturated in the half cycle of the frequency. As an example, only a few Amps of GIC in 5-legged cores can easily lead to half cycle saturation due to the low reluctance of ZS flux path.

4. Half cycle saturation causes number of issues, including:

   a) Flux leak into the tank. Although all core types see some degree of flux leakage into the off-core paths (including the tank), this may be an issue in 3-legged 3-phase cores where ZS flux path is not completed in the core.
   b) Reactive power loss increases. Due to the saturation in the core, the magnetization current increases considerably (hundreds of times the normal magnetizing current).
   c) Harmonics injected into the network increase. Highly distorted magnetization current due to half cycle saturation causes a significant amount of harmonics.

The flux leak may lead to the metallic parts heating up, such as tie bars, core clamps and the tank walls [7]. The duration of the GIC and the thermal time constant are key factors in the heating and the overall temperature rise [3] [7] [10] [11].

Reactive power loss leads to voltage instability in the power network due to the lack of reactive power generation [3]- [12].

Harmonics injected may lead to the windings extra heating, incorrect operation of protection systems, interference in operation of reactive power compensators (SVCs and capacitor banks) and finally voltage and angle instability in the power system [3] [13] [14].

The overheating in the tank walls and the other structural parts such as tie bars and the core clamps may not be considered as a risk of potential thermal danger during GICs as reported in [15], [16], [17] and [18]. However, as concluded in [19], "*it is important to recognize that identifying a transformer in this study as being at risk of potential thermal damage does not suggest a high probability of immediate failure. Rather, it signals that the transformer may be at risk of possible thermal damage and that further analysis is needed using information that is specific to a given transformer and system*".

It is worth mentioning that if the GIC is combined with an unbalanced condition, the heat generated in the tank walls and the structural parts will no longer be negligible.

Furthermore, even if the heating of the tank walls (and other metallic parts) does not pose a threat to transformer failure, it would influence the off-core inductance, reactive power consumed and magnetizing current drawn [14] [20].

Simulation of transformers subjected to the GIC and investigation of the consequences require an accurate electromagnetic and thermal representation of the off-core flux paths.

There has been a tremendous volume of research performed and papers published on transformer modeling, from developing new ideas to modifying and improving existing models. The models developed can be categorized into two large groups of black box and white box models. The black box models consider the transformer responses at the terminals and are more suitable for high frequency transients. The white box models are in fact physical models based on the transformer structure requiring design information and material properties. The white box models are more suitable for low frequency transients (including the asymmetrical operation and DC biased situation) where better representation of the topology and the non-linear magnetization characteristics of the core and the tank walls are of great significance. The details of the white box models depend on the area of

applicability, varying from simple equivalent circuits to rather complex circuital and numerical models.

The previous attempts in the white box modeling have covered different aspects of transformers including the core magnetization and losses, the multi-windings' arrangement and losses, leakage inductance and capacitive coupling between the windings and the core.

The varieties of topologically correct dual circuit models of transformers are of the most recent advances. In these models, the core equivalent circuit is obtained from the flux paths using duality transformation. Each flux path is represented with an inductor in its simplest lossless form, and with a ladder R-L circuit (with saturable/hysteretic characteristics) in the most complex and loss included form. As an advantage of the topologically correct core dual electric circuit, the magnetic losses can be represented in the correct location.

Both the core and the winding sections of such dual circuits have been improved substantially in the representation of the electromagnetic behavior of transformers as well as their parameters identification methods, as reviewed in Chapter 2. Examples of such improvements include a hybrid dual circuit model, dynamic hysteresis models to represent the core branches, topologically correct eddy current models of the windings, considerations on the multi-winding cases, etc.

Despite of the advancements in the core and the winding sections, the off-core flux paths beyond the outermost winding including the tank walls have not been sufficiently considered in previous works. Additionally, a proper thermal model of the tank walls coupled to the electromagnetic equivalent circuit is also missing in the literature.

1.2 Scope of work

In order to improve the existing dual circuit models in terms of zero sequence characteristics and the off-core flux path representation, the emphasis of this PhD work is put on the following aspects.

- The ZS modeling of 3-phase 3-legged transformers

Open-circuit zero-sequence (OC-ZS) and Short-circuit zero-sequence (SC-ZS) characteristics of 3-phase 3-legged transformers (without magnetic shields or shunts) are addressed in the thesis. Since the off-core magnetic path is the only return path of the ZS flux, the ZS modeling can be reduced to the off-core flux path modeling. Discussions on the differences between the ZS impedances seen from different windings are highlighted through the equivalent circuit developed in the thesis.

- Developing an equivalent circuit for the off-core flux paths

Using the duality principle, a topologically correct electric equivalent circuit is proposed for the off-core flux paths including the tank walls, bottom and cover. The parameters of the circuit are described, and calculation approaches are presented.

The metallic parts including the tie-bars and the core clamps as well as magnetic shunts and magnetic shields are out of scope in the modeling.

- Thermal modeling of the tank walls

In order to investigate the heat transfer capability of the tank walls during unbalanced conditions, a thermal equivalent circuit for the tank with non-linear convective and radiative thermal resistances is proposed that is coupled to the electric equivalent circuit.

- Magnetic characterization of the tank steel

As a part of the research work, the magnetic properties of sample steels, which are used in the transformer tank, are measured in terms of the B-H characteristics and magnetic losses. In addition, different mechanisms of the dynamic losses including classical eddy current and excess losses are investigated on the steels considered.

- Applications

As applications of the off-core path model proposed in this thesis, two main situations are considered where the ZS characteristic of transformers is of importance, which are as follows:

  - Transformers subjected to GIC during geomagnetic disturbances
  - Transformers under asymmetrical operation/faults

1.3 Research context

This PhD work is a part of a larger co-operative project (between electrical utilities, TSOs, industry, and the Research Council of Norway) entitled 'Electromagnetic Transients in Future Power Systems', which was a "Knowledge-building project with user involvement" (KMB) in the terminology of the Research Council of Norway. The focus of the KMB project was put on the development of computational tools and procedures covering several key components that were considered to be essential in the future power systems, including power transformers, cables, circuit breakers and instrument transformers.

The present PhD work falls under 'Non-linear and hysteretic transformer modeling' sub-project (of the KMB project) where the original objective was to enhance the modeling of power transformers for the simulation of low-frequency transient in EMTP-type simulation tools. A dual circuit model of transformers including its different variants was considered for further improvements in terms of non-linear and hysteretic core model as well as zero sequence and the off-core flux paths modeling. The latter is the topic of this PhD work.

1.4 Thesis structure

The thesis is structured in eight chapters as stated in the following:

Chapter 1 Introduction

Zero sequence modeling of transformers and its importance in power system analysis are reviewed in this chapter. The scope of this current work and the structure of the thesis with a summary of publications resulted from the research work are given in this introductory chapter.

Chapter 2 Background

This chapter reviews the literature with respect to the previous attempts in zero sequence modeling of the transformers. In addition, the motivations for further works on the topic are presented and discussed.

Chapter 3 Modeling of the off-core flux path

The model proposed for the off-core flux path is presented in this chapter. This model includes electric and thermal equivalent circuits, which are coupled through the losses generated in the wall. The electric circuit is topologically correct, as obtained from the magnetic circuit of the off-core flux paths using duality transformation.

Chapter 4 Tests and measurements

The electric and magnetic measurements performed on the steel specimens of the tank walls are presented in this chapter. It then provides with the results of ZS impedance tests performed on sample transformers, which are used for benchmarking of the model presented in Chapter 3.

Chapter 5 Evaluation and discussion on the parameters

This chapter presents evaluations and discussions on the model parameters through simple 2D-FEM simulations. A number of tuning factors are introduced in order to fit the model to the FEM simulation results. These tuning factors are of key importance, which result from describing the wall with one-dimensional magnetic diffusion equation.

Chapter 6 Benchmarking of the off-core model

The model described and discussed in the previous chapters is used to be benchmarked by a sample transformer, which is fully experimentally identified in terms of zero sequence impedances and losses, as presented in Chapter 4.

Chapter 7 Applications

This chapter presents the use of the off-core model in the simulation of two main applications targeted in this thesis including transformers subjected to DC biasing, and transformers operation under unbalanced conditions.

The impact of the off-core flux paths on the consequences of a GIC event is discussed through the simulation results (in terms of harmonics, reactive power consumption, losses, and magnetizing currents) of a sample transformer.

In addition, unbalanced operation of transformers with a detailed model for the off-core flux path is studied through the simulation results of a sample transformer; considering two unbalanced situations for the primary and secondary sides.

Chapter 8 Conclusions and future works

This chapter concludes the research work performed in this thesis, highlighting important results of the simulations and discussions.

It follows with suggestions for the future works that can further improve the model in terms of the calculation of parameters and extension of the model.

1.5 List of publications

List of papers presenting the results of this work including conference and journal papers are as follows:

- **Conference proceedings**

1. **Abbas Lotfi**, Hans Kr. Høidalen, N. Chiesa, E. Rahimpour, 'Calculation of Off-core Inductances in dual-circuit model of transformer', Power System Computational Conference (PSCC), 2014, Wroclaw, Poland.

This paper presents a calculation approach based on 2D-FEM for the off-core inductances assuming that the tank steel has linear magnetic properties. The approach proposed can be used for calculation of linear inductances representing the oil gap between the active part and the tank. Reducing the computational burden of the 3D-FEM by means of equivalent 2D-FEM analysis has been excluded from the scope of the work; thus, the method of calculation discussed in this paper is not included in the current thesis. However, the approach based on 3D-FEM for calculation of the off-core inductance, which was used to verify the results obtained from adopting a 2D-FEM based approach, is presented in the current PhD thesis.

My contribution to the aforementioned paper includes:

- Making 3D-FEM based model of a 300 kVA 3-phase, 3-legged transformer (as a case object) and doing simulations to obtain inductance matrix
- Implementing the required routine and code in MATLAB to calculate the off-core inductance from the inductance matrix obtained from 3D-FEA
- Making 2D-FEM based models of the case object to be used in calculation of the off-core inductance
- Implementing the required routine and code in MATLAB to calculate the off-core inductance using the simulation results of 2D-FEM

2. N. Chiesa, **Abbas Lotfi**, Hans Kr. Høidalen, B. Mork, Ø. Rui, T. Ohnstad, 'Five leg transformer model for GIC studies', International Power System Transient conference (IPST), 2013, Vancouver, Canada.

The main purpose of this paper is to study the GIC impact on 5-legged 3-phase transformers in terms of reactive power losses, magnetizing current and its harmonics as well as the false operation of the protection relays. The transformer is simulated with the use of a hybrid transformer model where the off-core inductance is considered with a linear inductor. The sensitivity of the results to the off-core inductance is studied. As the results show, the off-core inductance has an influence on the reactive power consumed and maximum magnetizing current.

My contribution to this paper includes:

- Making a 3D-FEM model for a 5-legged 3-phase transformer used as the case object of the paper

- Implementing the required routine and code in MATLAB to calculate the off-core inductance using the simulation results of 3D-FEM

- **Journal Papers**

1. **Abbas Lotfi**, Hans Kr. Høidalen, N. Chiesa, 'Effect of DC biasing in 3-legged 3-phase transformers taking detailed model of off-core path into account', Electric Power System Research, Vol. 138, 2016.

This paper presents the detailed off-core path model as proposed in this thesis (excluding the thermal model of the tank) for simulating of a 3-phase, 3-legged transformer subjected to GIC (based on Chapters 3 and 7 of the current thesis). In addition, a comparison is made between the presented model and a simpler model with only a single linear inductor.

My contribution to this paper includes:

- Making a 3D-FEM based model of a 300 kVA 3-phase, 3-legged transformer (case object) and doing simulations to obtain the inductance matrix
- Implementing the required routine and code in MATLAB to calculate the off-core inductance using the inductance matrix obtained from 3D-FEA
- Implementing the proposed dual circuit model of the case object including a detailed off-core flux path model in ATPDraw and doing the simulations

2. **Abbas Lotfi**, Hans Kr. Høidalen, E. Agheb, A. Nysveen, 'Characterization of the magnetic losses in the transformer tank', IEEE Trans. Magnetics, Vol. 52, Issue 5, 2015.

This paper presents a version of Chapter 4 of the current thesis including magnetic measurements performed on the tank steel samples. Different loss mechanisms are studied through experimental and calculations results.

My contribution to this paper includes:

- Performing electric and magnetic measurements on the tank steel samples using the measurement system of MPG 100D, AC–DC and a single-sheet tester specifically designed for the flat and thick (up to 6 mm) samples
- Implementing the required routine and code in MATLAB/SIMULINK to calculate the classical and excess losses

Chapter 2

Background

2.1 Method of symmetrical components

In order to analyze transformers in unbalanced operations, the traditional method of symmetrical components with phase sequence characteristics of 3-phase transformers is used [21] [1]. In this concept, three single-phase equivalent circuits of positive sequence (PS), negative sequence (NS) and zero sequence (ZS) are identified that are interconnected for a specific unbalanced situation [22]. Using symmetrical equivalent circuits (constructed with symmetrical impedances), symmetrical components of voltages and currents are calculated, from which the actual phase currents and voltages can be obtained. Based on the flux paths of each phase sequence, PS and NS impedances are equal but differ from ZS impedances. The single-phase equivalent circuits based on the symmetrical impedances as seen from the windings are the simplest low frequency models of transformers.

Two types of ZS impedances are distinguished as magnetizing (termed as Open Circuit Zero Sequence OC-ZS impedance) and short circuit (termed as Short Circuit Zero Sequence SC-ZS impedance) impedances. Winding connections and core construction determine ZS impedances [2]. From the winding perspective, Y-connected winding with grounded neutral point can only carry a ZS current that returns through the ground conductor. D- and Y-connected (with no grounded neutral point) windings lead to an open circuit in the lines. However, the ZS current can circulate in the D-connected windings when there is a ZS driving voltage induced from the other winding [1]. In this case, the D-connected winding is in fact a short circuit from the ZS point of view.

From the core perspective, 5-legged core design provides a return path for the ZS flux in the core through the outer legs leading to a low reluctance and thus high magnetizing ZS impedance in the same range as magnetizing PS impedance.

There is no such return path in the 3-legged core design, where the ZS flux path is closed through the off-core paths. Hence, the reluctance is relatively higher, leading to lower magnetizing ZS impedance [1] [2]. Since the off-core flux path involves the tank walls, considerations on the tank wall design including magnetic shunts and magnetic shields will also affect the magnetizing ZS impedances [1]. Magnetic shunts are made of core steel laminations that provide a low reluctance path bypassing the tank walls. Magnetic shields are made of electric conductors such as copper that can be considered as a one turn winding encompassing all three phases. The current induced in the shield by the resultant off-core flux will balance the amp-turn and the flux will be confined between the excited windings and the shield.

In the ZS impedance test setup, the terminals of the windings from which the test is performed (either HV or LV where possible) are connected together (common connection point CCP) and a single-phase voltage is applied between the CCP and the neutral point. Measuring the current at the common point, the impedance is calculated [23] [24]. It must be noted that the ZS test voltage level should be controlled to prevent any temperature rise in the metallic parts and the tank from exceeding the maximum permissible values, particularly in a 3-legged core design. This ensures no thermal issues in the insulations of transformers during the ZS tests. Considerations of transformers with different vector groups as well as the influence of the tertiary D-connected winding on the ZS impedance measurements are discussed in [25], [26], [27] [28], [29], [30], [31], and [32].

Calculation and evaluation of ZS impedances, as used in the method of symmetrical components, have been the topic of many papers published in journals, conference proceedings and technical reports. As investigated, numerical methods have been the most useful approaches in the calculation of ZS impedances. The validity of the finite element method (FEM) was investigated in [33] (3D-FEM), [34] (2D- and 3D-FEM) and [35] (2D-FEM) as compared to measurements. In [36], [37] and [38], 2D-FEM model of transformers and reactors including the tank was built for ZS analysis in terms of impedance calculation and heating analysis in the walls.

In addition, estimation approaches for ZS impedance determination based on the extensive test results have been presented and discussed in the literature [2] [25] [39].

Discrepancies in the ZS impedances seen from different sides of a transformer due to the arrangement of the windings and thus different flux paths are comprehensively addressed in [40] [39] [41].

Generally speaking, models of transformers based on the method of symmetrical components are the most beneficial for use in system-level analysis. However, the calculation of ZS impedances is complex and requires numerical methods. These models normally include linear ZS impedances resulting from the tests report or the calculations at one single point of excitation and ambient condition. Therefore, they are not topologically

correct and some important issues such as magnetic coupling between the phases and the tanks, actual location of the losses in the electric equivalent circuit, effect of temperature and the non-linearity of the ZS flux paths are missing, which leads to a loss of accuracy.

As suggested in the literature, equivalent circuits based on topologically correct representation of the magnetic structure of transformers are the most suitable models for low frequency transient studies including unbalanced operations and non-linear behaviors [42] [43] [44] [45]. Figure 2.1 depicts a dual circuit model for 3-phase 3-legged 2-winding transformers where the black boxes represent the core legs and yokes, linear inductances of L_{CL} represents the gap between the innermost winding and the core, L_{LH} represents the leakage channel between the two windings, and $L_{Off\text{-}core}$ the off-core flux paths.

Using a dual circuit similar to Figure 2.1 with a proper representation of the off-core flux path, ZS characteristics of transformer can be studied for different situations of windings connections and arrangements. The following section reviews dual circuit models in the literature, with an emphasis on the off-core flux path representation.

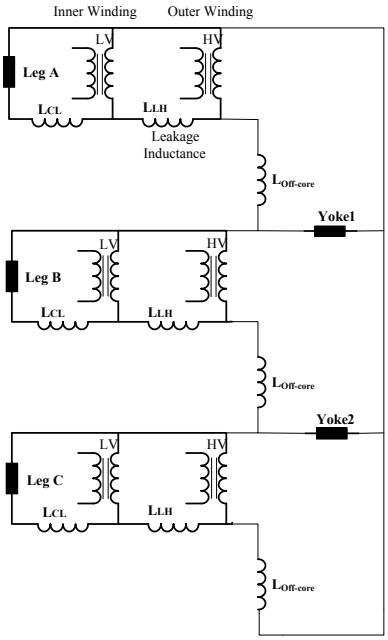

Figure 2.1 Topologically correct equivalent circuit of 3-phase 3-legged transformers based on duality transformation

2.2 Dual circuit model of transformer, the off-core flux path

Dual circuit models have had extensive development from the first ideas [46] [47] [48] to the advanced variations presented in the recent years [49] [50] [51]. Key research works in topology-based transformer modeling published before 2005 are reviewed in [44].

Overviewing those works shows that the off-core flux path is introduced as a non-linear branch; however, to simplify the models based on the intended applications it is either

neglected or represented as a linear inductor (which is normally identified through the OC-ZS impedance test) [52] [45] [53] [54] [55] [56] [57] [58].

In the papers published since 2005, different aspects of the dual circuit models are extensively improved as briefly summarized in the following:

- Hybrid transformer model is introduced by B. Mork, et al. in the two-part paper [59] and [60] that was later implemented in ATPDraw and called XFMR [61]. The model consists of a short-circuit network (that includes winding resistances and inverse leakage inductances detailed in [62] and [63]) connected to the topologically correct core dual circuit through fictitious infinitely thin windings at the surface of the core legs. The frequency dependent resistances are described with Foster circuits. The capacitive effects are described with a capacitance matrix at the windings terminals. Further developments are performed on the core and the short-circuit sections, as presented in [64] and [65]. The off-core path is considered to be as a linear inductor in this model without taking into account the tank. Furthermore, the off-core inductor is connected to the innermost fictitious windings at the core surface instead of its true place, the outermost windings.
- To overcome the numerical instability issue caused by negative inductance in the equivalent circuit of the 3-winding transformers, a circuit derived from the principle of duality is presented in [66].
- A dual reversible single phase transformer model is presented in [67] where the off-core flux path is first introduced with a non-linear inductor; however, the circuit is later simplified in the paper and unified with the non-linear inductor of the yoke.
- A duality-based model of 3-phase transformer including eddy current effects in the windings is presented in [68]. The off-core flux path is considered imprecisely with linear and non-linear inductors for both the tank walls and the oil gaps, and there is no attempt to detail them.
- The paper [69] presents an interesting approach in the representation of the zero sequence characteristic of 3-legged, 3-phase transformers in the recent years. The model is based on the magnetic circuit of the transformer where each flux path is represented with proper linear reluctances for leakage channels and non-linear reluctances for the core and tank wall. The off-core path consists of three components; the leakage off-core reluctance representing the gap between the active part and the tank wall, the reluctance linking the core to the wall, as well as the tank wall. The first two are linear reluctances and the last is non-linear. It is assumed that the flux enters/exits the wall through single points and flows in the vertical direction. The tank wall is considered as being a belt of steel encompassing the active part. In the magnetic formulation of the wall, a static hysteresis model [70] is used to relate flux density (B) to flux intensity (H) in each subdivision of the wall thickness. The off-core model inputs include magnetic/electric characteristics and dimensions of the tank steel. The linear inductances are estimated through fitting the model to the given OC-ZS impedance test results.

The tank losses, temperature influence of the wall, the precise effect of the multiple flux entrance points, the tank cover and bottom potential effects are not discussed in the presented model.

Further development of this model to include the magnetic shunts is presented in [71].

- The model presented in the two-part paper [72] and [73] introduces a detailed model of off-core flux path including the tank, the oil gap, structural parts and the magnetic shunts for different types of transformers. Interesting discussions are presented regarding the equivalent flux-current characteristics of the off-core path at high saturation condition as well as normal operation. The flux fringing when approaching the walls is explained and analytical calculations are given to include them in the linear inductors of the oil gaps.

  In order to ease the estimation of parameters, a simplified version of this complex off-core network is used later in the paper where the walls, the cover and the bottom are merged and represented with a non-linear inductor in parallel to a non-linear resistance and a linear inductor. This leads to missing of the topologically true features of the tank model and loss of accuracy when the walls, bottom and cover have different electric, magnetic or thermal properties. Furthermore, the magnetic coupling between the phases through the walls encompassing the active part is neglected. The temperature influence is not taken into account in the presented model, which could affect the losses and the ZS impedance, particularly at higher excitations. This may lead to an inaccuracy when simulating situations other than the test results, which are used for the model identification. Although the fringing of the linking air flux when approaching the tank walls has been comprehensively discussed, the formulas developed for the effective length and effective area of the oil gap are based on infinite magnetic permeability for the wall without considering the effect of the wall's electric conductivity in the flux distribution. It must be noted that the magnetic permeability and electric conductivity of the tank steel both influence the flux fringing near the wall.

  It is concluded that the curve of the ZS impedance versus voltage at lower voltages is primarily due to the structural metallic parts that saturate at noticeably lower excitations. This should be carefully considered and should be extended to all transformers. As will be shown in this thesis, even with no structural steels like tie-bars and the core clamps, the ZS impedance is given a similar peaked shape (increasing at lower and decreasing at higher voltages), which is due to the field dependent magnetic characteristics of the tank steel at lower voltages.
- Complementary guidelines are given in [50] on the off-core flux path modeling, paying special attention to the tank effects based on the major works of [69], [72] and [73]. The discrepancies in the conclusion on the significance of the tank and the structural steels in ZS characteristics of transformers are addressed. Some other issues such as the need for testing of the models in terms of the zero sequence losses and the models adequacy at the higher frequencies are also discussed.

2.3 Thermal modeling of the tank walls

A comprehensive overview on thermal modeling of power transformers can be found in the CIGRE technical brochure 659 [74] and in the review paper of [75]. A thermal network model is one of the widely used approaches in the thermal analysis of transformers where a thermal equivalent circuit is built with lumped elements corresponding to the heat transfer paths. This concept is based on the thermal-electrical analogy, namely resistors representing the thermal resistance, capacitors representing the thermal capacitance, voltage sources representing the temperature, and current sources representing the heat sources (losses). The complexity of the models depends on the intended application and the tank is not separately considered in most dynamic thermal models such as hot spot temperature and top oil temperature models [75].

In a few thermal circuit models, the tank is considered as being a thermal node connected to the either sides through linear thermal resistances [76] [77]. However, the losses generated in the tank walls as well as the coupling of heat transfer problem to the electromagnetic problem are not considered.

2.4 Research gaps in the off-core flux path models

As explained, only two major works have been presented in representation of the off-core flux path [69] [72] and further investigations are still required to bridge the following gaps in the existing models.

- Zero sequence losses in 3-legged 3-phase transformers
  Although it is repeatedly mentioned that the losses in the tank (and other metallic parts) are of importance, this is not properly considered in the dual circuit models yet.
- Differences between the ZS impedances as seen from different windings of a transformer and its potential influence on the dual circuit parameters are not considered in the past works.
- In the papers reviewed, there has been a lack of data regarding the electromagnetic properties of the tank steel necessitating comprehensive magnetic tests on typical tank steels.
- Thermal effects of the tank walls in the ZS characteristics of transformers and their modeling considerations are lacking in previous research.
- Influence of tank wall design such as plain walls and corrugated walls on the ZS characteristics of transformers is not properly discussed in the literature.
- How to consider the walls as a boundary condition if it is decided to skip the walls in the modeling process? How close is the behavior of the tank walls to the flux-tangential boundary condition or to the flux-normal boundary condition?

The model presented in this PhD thesis is a development of the model proposed in [69] in order to address the issues listed above.

Chapter 3

Modeling of the off-core flux path

3.1 Electromagnetic modeling

Since ZS flux does not have a return path inside the core, it leaves the core and returns via the tank and the non-magnetic oil gap. Figure 3.1-a shows the physical structure of these off-core flux paths. The magnetic circuit of the physical paths and its electric dual are shown in Figure 3.1-b and Figure 3.1-c where the magnetic reluctances $\Re_1$ through $\Re_5$ with their electric duals of the inductors L_1 through L_5 represent the paths Φ_1 through Φ_5. The non-linear branches representing the tank wall, cover and bottom are composed of Cauer-like ladder circuits that will be developed in the following sub-sections.

The tank encompassing the active part is magnetically coupled to the windings. This is considered in Figure 3.1-c with ideal transformers (with turn ratio of one) connecting each tank element to the linear inductors of the oil gap.

Figure 3.2 shows the overall model (of a 3-legged transformer) where the off-core equivalent circuit is added to the conventional dual circuit of the windings and the core. As can be seen, the tank wall is coupled to the phases and connected in delta (this also applies the tank cover and bottom). To make the figure readable, the circuit of cover and bottom is not shown. In the overall circuit, the L_{CL} represents the gap between the innermost winding and the core leg and the L_{LH} represents the leakage inductance between two windings. The core branches shown with black boxes can be modeled with varieties of parallel R-L equivalent circuits or more complex hysteretic inductor [78] [70].

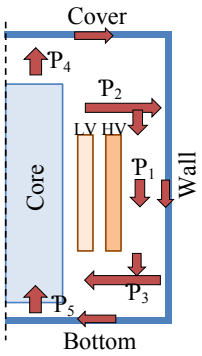

a) Physical flux paths

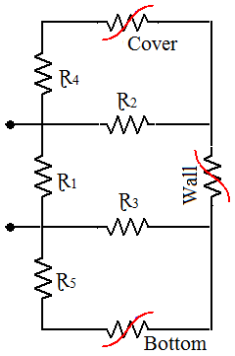

b) Magnetic circuit

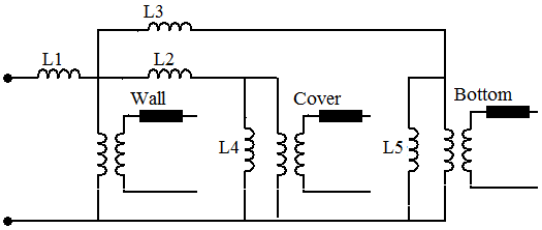

c) Electric equivalent circuit, ideal transformers have turn ratio of one

Figure 3.1 Off-core flux path, equivalent dual circuit development

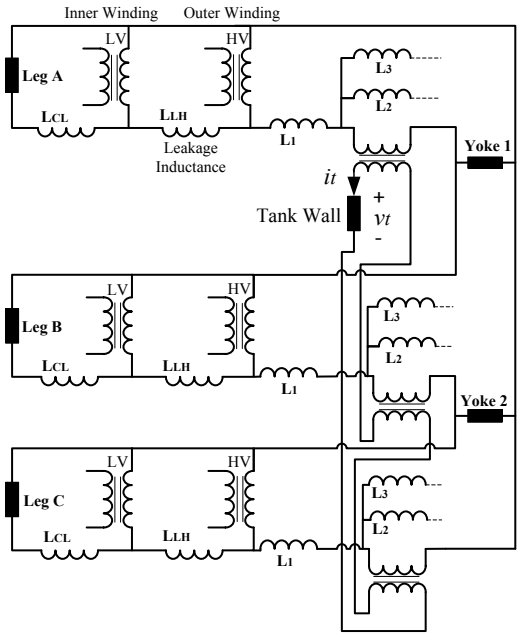

Figure 3.2 Overall dual circuit model of a 3-phase, 3-legged transformer including the off-core flux path model

3.1.1 Electrical equivalent circuit of the tank wall

Considering the wall as a base study, a Cauer-like equivalent circuit is developed to represent the tank steel of the wall replacing the black box in Figure 3.1-c. The bottom and cover will have similar circuits obtained in the same fashion. The voltage v_t induced in the wall is considered as being the electric input driving the current i_t considered as to be the electric output of the circuit (see Figure 3.2).

Assuming that the flux enters and exits the tank walls through single points and flows in one direction, the magnetic diffusion equation is reduced to one dimension, as stated in (3.1) [79]. To obtain the equivalent circuit, this one-dimensional form of magnetic diffusion equation is solved using finite difference method. Figure 3.3 shows the tank wall and the coordinate system used to formulate the equations. The electric (E_i) and magnetic fields (H_i) are attenuated along the *x*-axis from inner to outer surfaces.

$$\frac{\partial^2 H}{\partial x^2} = \sigma \frac{\partial B}{\partial t} \tag{3.1}$$

where σ is the conductivity and x is the penetration direction of H (magnetic flux intensity), and B is the magnetic flux density.

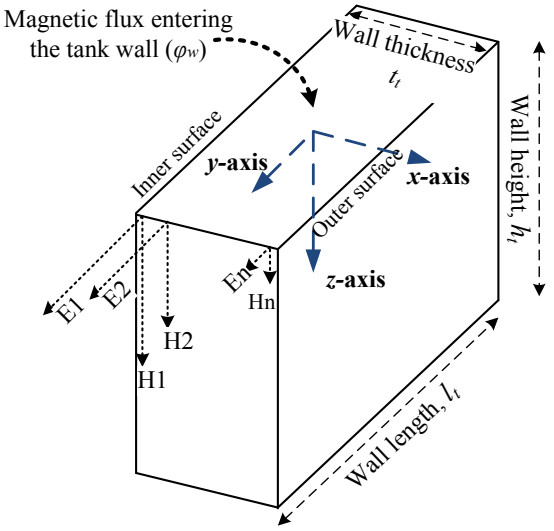

Figure 3.3 Electric and magnetic field orientation assumed for the tank walls

The wall thickness (t_t) is discretized into $(n-1)$ layers in which the flux density is uniformly distributed. Relation of H and B in each internal layer is described by (3.2) using second-order central difference for the space derivative [69].

$$\frac{dB_i}{dt} = \frac{H_{i-1} - 2H_i + H_{i+1}}{\sigma \Delta x^2}, i = 2, \ldots, n-1 \tag{3.2}$$

where B_i and H_i are respectively the magnetic flux density and flux intensity at layer *i*, and Δx is the thickness of each layer ($\Delta x = \frac{t_t}{n-1}$). Using the Neumann boundary condition at the

inner surface, the electric (E_1) and magnetic (H_1) fields can be expressed by (3.3).

$$\sigma E_1 = -\frac{\partial H_1}{\partial x} = \frac{H_1 - H_2}{\Delta x} \rightarrow H_1 = (\sigma \Delta x) E_1 + H_2 \tag{3.3}$$

where H_2 is the magnetic field at layer 2. Using the relation $E_1 = v_t / N l_t$, it follows:

$$H_1 = \frac{\sigma \Delta x}{N l_t} v_t + H_2 \tag{3.4}$$

where l_t is the length of the current path (as an example, for the wall of plain type, it is equal to the wall circumference), v_t is the voltage induced in the tank and N is the turn number of the winding from which the tank is seen.

In the same fashion as used for E_1, the electric field at the outer surface (E_n) can be expressed by:

$$\sigma E_n = -\frac{\partial H_n}{\partial x} = \frac{H_{n-1} - H_n}{\Delta x} \tag{3.5}$$

Moreover, E_n can be associated with the flux beyond the tank wall through (3.6) [69]:

$$E_n = \frac{1}{l_t}\frac{d\varphi_{0t}}{dt} = \frac{1}{l_t}\frac{d}{dt}\left(\frac{h_t H_n}{\Re_{0t}}\right) = \frac{1}{l_t}\frac{h_t}{\Re_{0t}}\left(\frac{dH_n}{dt}\right) \tag{3.6}$$

where φ_{0t} is the flux beyond the tank and $\Re_{0t}$ is the reluctance of that flux path given by classical equation of $\Re_{0t} = h_t / \mu_0 t_t l_t$ [69] whereas μ_0 is the magnetic permeability of free space.

Substituting (3.5) in (3.6), the other boundary equation is obtained as (3.7).

$$\frac{dH_n}{dt} = \frac{\Re_{0t}}{\sigma \Delta x}\frac{l_t}{h_t}(H_{n-1} - H_n) \tag{3.7}$$

Based on the equations given above, an equivalent circuit can be realized to be used in EMTP-like programs. Starting with $i_i = H_i \cdot h_t / N$ for each discretized layer, (3.4) can be re-written as circuital form:

$$v_t = \frac{N^2 l_t}{\sigma \Delta x h_t}(i_1 - i_2) = R(i_1 - i_2) \tag{3.8}$$

where $i_1 = i_t$ is the current induced in the wall. It is explicit that $R = N^2 l_t / (\sigma \Delta x h_t)$ is the electric resistance of each layer referred to the side of the winding excited. (3.8) can be realized by a circuit, as shown in Figure 3.4-a.

Multiplying both sides of (3.2) by $l_t \cdot \Delta x$ and doing some manipulation, the flux of each layer can be expressed as follows:

$$\begin{aligned} &\frac{d\varphi_i}{dt} = \frac{l_t \cdot \Delta x}{\sigma \Delta x^2}(H_{i-1} - 2H_i + H_{i+1}) \rightarrow \frac{d\lambda_i}{dt} = \frac{N^2 l_t}{\sigma \Delta x \cdot h_t}(i_{i-1} - 2i_i + i_{i+1}) \\ &= R(i_{i-1} - 2i_i + i_{i+1}) \end{aligned} \tag{3.9}$$

Realization of the flux φ_i with an inductor, giving the voltage notation of e_i and e_{i+1} to the nodes of inductors and assuming that R is connected between each node and the circuit common node, (3.9) can be re-written as:

$$\frac{d\lambda_i}{dt} = R(i_{i-1} - i_i) - R(i_i - i_{i+1}) = e_i - e_{i+1} \tag{3.10}$$

An equivalent circuit synthesized from (3.9) and (3.11) is shown in Figure 3.4-b. The $\lambda - i$ characteristic of the non-linear inductances is expressed by:

$$\lambda_i = N \cdot \Delta x \cdot l_t \cdot f_{BH}(\frac{N}{h_t} i_i) \tag{3.11}$$

where f_{BH} describes the relationship between *B* and *H*.

Finally, multiplying both sides of (3.7) by h_t, the circuital relation of (3.12) is obtained which is realized by the circuit shown in Figure 3.4-c.

$$\frac{N^2}{\Re_{0t}} \frac{di_n}{dt} = \frac{N^2 l_t}{\sigma \Delta x \cdot h_t}(i_{n-1} - i_n) \rightarrow L_{0t} \frac{di_n}{dt} = R(i_{n-1} - i_n) \tag{3.12}$$

where L_{0t} is corresponding to $\Re_{0t}$.

Connecting all sub-circuits together, the equivalent circuit of the tank wall is obtained as shown in Figure 3.5.

The tank cover and bottom will have similar equivalent circuit with, however, different dimensional parameters and material properties.

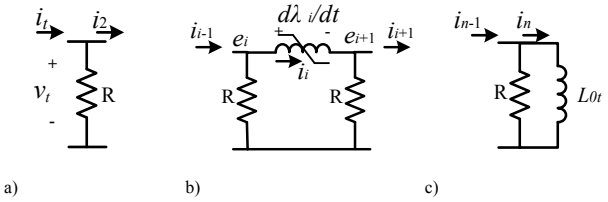

Figure 3.4 Realization of: a) inner b) middle, and c) outer layer of the discretized tank wall

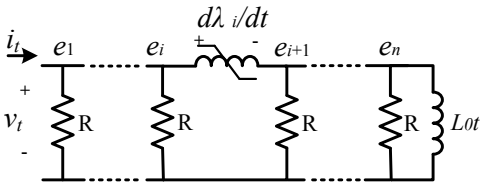

Figure 3.5 Detailed equivalent circuit of the tank elements

3.1.2 Implementation of the tank model in MATLAB-SIMULINK

The model of the tank wall stated in 3.1.1 is implemented in MATLAB-SIMULINK as explained in the following (see Figure 3.6). SIMULINK as a graphical environment for time domain simulation of dynamic systems enables rapid construction of multi-discipline models. It provides an easy-to-present advantage using the blocks building up the model and the signals flow paths. All input parameters and non-linear characteristics can be called from an m-file to SIMULINK environment that makes the sensitivity analysis to be as easy as scripting approaches.

1. As previously explained, the v_t is the voltage induced in the tank which drives the current i_t in the tank, both referred to the winding excited.
2. The voltage v_t is an electric input and the current i_t (as well as time derivative of i_t: di_t/dt) is an electric output of the model. In addition, distribution of the magnetic flux density (*Bdis*) and flux intensity (*Hdis*) across the wall are of magnetic outputs (Figure 3.6-a).
3. The first layer block diagram and how the inputs and outputs are connected to the rest parameters are shown in Figure 3.6-b and Figure 3.6-f.
4. Block diagrams of the last layer with the respective equation implementation are shown in Figure 3.6-c and Figure 3.6-e.
5. Implementation of (3.2) for the inner layers is shown in Figure 3.6-d. The look-up table relating B and H contains the single-value B-H normal curve of the wall steel.

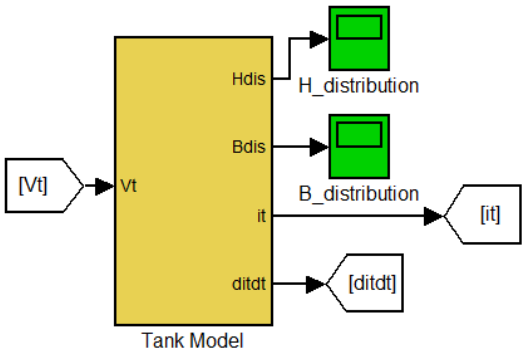

a) The model block, inputs and outputs

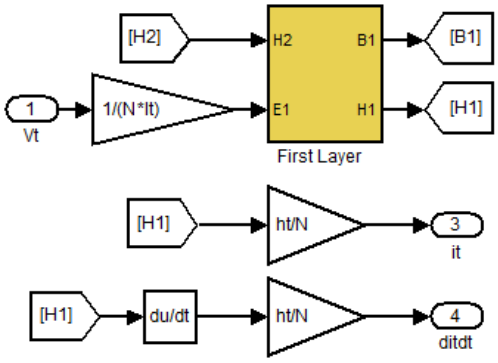

b) The first layer and connection points

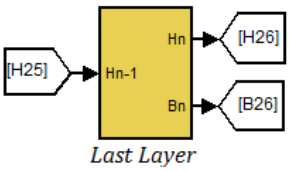

c) The last layer, inputs and outputs

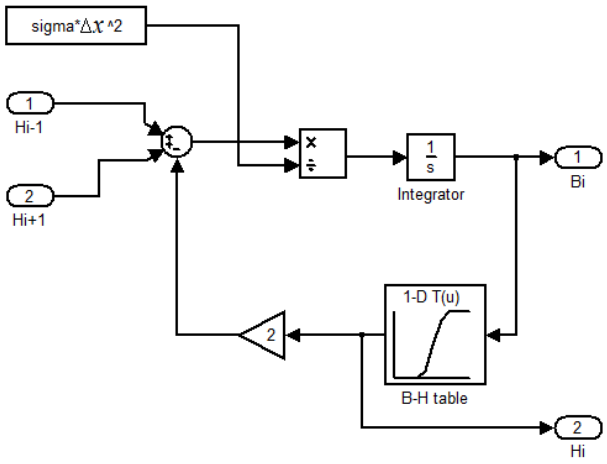

d) Implementation of (3.2)

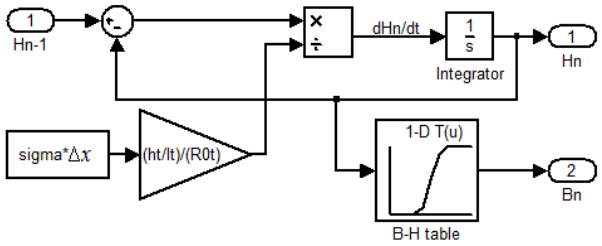

e) Implementation of (3.7)

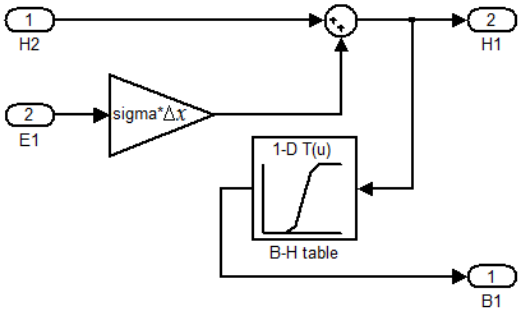

f) Implementation of (3.3)

Figure 3.6 Implementation of the discretized model of the tank in MATLAB-SIMULINK, 'sigma' is the tank steel conductivity denoted with σ in the formulations

3.1.3 Excess losses

The equivalent circuit in Figure 3.5 is developed from a Maxwell equation assuming that the magnetic material is homogeneous containing no grains or magnetic domains. The loss calculated from this equivalent circuit so-called classical eddy current loss is normally lower than the measured value even if an accurate hysteresis model is used to relate B and H in the formulations. The difference between the measured loss and calculated classical eddy current loss is called excess loss (anomalous loss) [80] [81] [82].

The magnetic field corresponding to the excess losses can be expressed by (3.13) [83] [70].

$$H_{exc} = g(B)\left|\frac{dB}{dt}\right|^{0.5} \tag{3.13}$$

where H_{exc} is the magnetic field representing the excess losses, $g(B)$ is the fitting parameter that is a function of magnetic flux density. The $g(B)$ can be determined from the magnetic measurements as presented in Section 4.1.4.

In a macroscopic perspective, space average magnetic flux density (B_a) is used in (3.13) instead of pointwise B. The B_a is related to the voltage v_t through (3.14).

$$B_a = \frac{1}{Nl_t h_t}\int v_t\, dt \rightarrow \frac{dB_a}{dt} = \frac{v_t}{Nl_t h_t} \tag{3.14}$$

Using (3.13) and (3.14), it follows:

$$H_{a\_exc} = \frac{g(B_a)}{(Nl_t h_t)^{0.5}}|v_t|^{0.5} \tag{3.15}$$

where H_{a_exc} is the macroscopic magnetic field of excess losses that can be related to its electric dual (i_{exc}) through $H_{a\_exc} = \frac{N}{h_t} i_{exc}$. Substituting in (3.15), follows that:

$$i_{exc} = g'(B)|v_t|^{0.5} \tag{3.16}$$

where $g'(B_a) = \left(\frac{h_t}{Nl_t}\right)^{0.5} \frac{g(B_a)}{N}$.

The equation (3.16) can be realized with a non-linear resistance at the terminal of the equivalent circuit, as shown in Figure 3.7-a. The equations (3.14) and (3.16) are implemented in MATLAB-SIMULINK as shown in Figure 3.7-b. The classical eddy current is denoted with i_{cl}, excess current with i_{exc} and the total current becomes $i_t = i_{cl} + i_{exc}$.

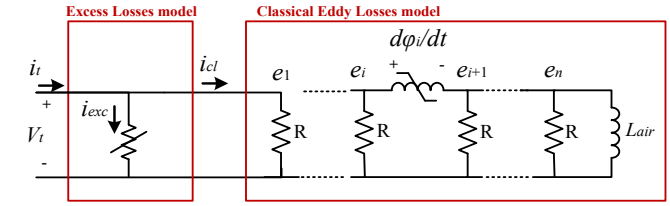

a) Equivalent circuit

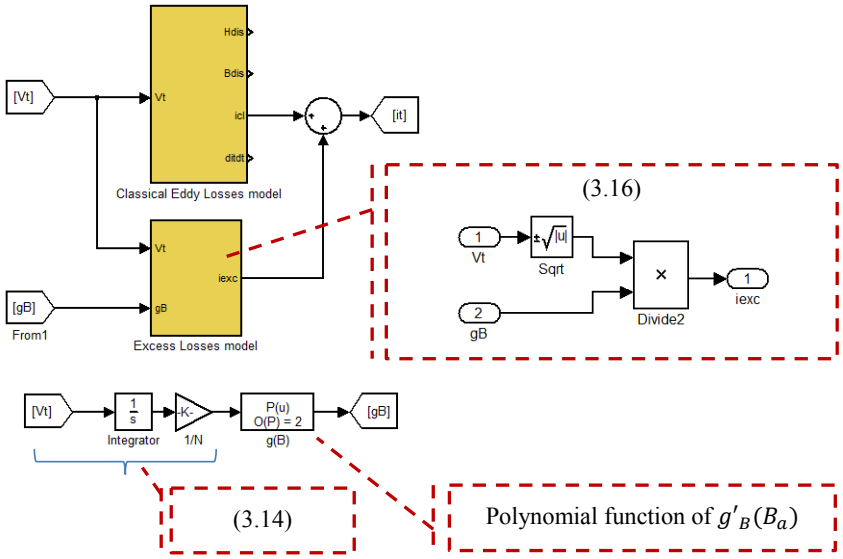

b) Implemented in MATLAB-SIMULINK

Figure 3.7 Equivalent circuit of the tank wall including the excess losses model

3.2 Thermal modeling

As repeatedly discussed in previous sections, higher the off-core flux, greater the voltage, which is induced in the wall driving a large amount of current into the wall. This generates Joule losses that can lead to considerable temperature rises in the tank steel. This temperature can easily reach beyond 100℃ in power transformers [84] [85]. As a result of such high temperatures, the electric conductivity of the tank steel decreases dramatically compared to the cold condition influencing the magnetic behavior of the wall in terms of flux penetration depth and losses. This necessitates thermal modeling of the tank walls, as presented in the following section.

3.2.1 Thermal equivalent circuit

Figure 3.8 illustrates the heat transfer from the plain wall where P_t is the heat generated in the wall due to the Joule losses. Since the heat P_t is not distributed uniformly in the wall, the temperature may vary from the inner to outer surface. However, the Biot number, which is defined as the ratio of heat convection from the wall surface to the heat conduction through

the wall, is normally very small due to relatively high convective heat transfer coefficient at both inner and outer surfaces, high thermal conductivity of the steel and small characteristic length of the wall [86]. The characteristic length is defined as ratio of the volume to the area normal to the heat transfer direction. For the plates (like the tank walls), this is equal to the plate thickness. The temperature difference across the plate thickness can be neglected for the Biot numbers less than 0.1 (which is normally the case for the tank walls) [87]. This means that the wall can be considered as a thermal node.

As an example, for a wall with characteristic length of 3 mm, the convective heat transfer coefficient of 5 W/(m^2.K) and thermal conductivity of 43 W/(m.K), the Biot number becomes 3.5×10^{-4}.

Figure 3.9 shows a thermal equivalent circuit for the model of Figure 3.8. The quantity T_i represents the convective thermal resistance to the oil. The T_{oc} and T_{or} represent the convective and radiative thermal resistances to the ambient. The θ_{oil}, θ_{amb} and P_t together with physical properties of the air, oil and the wall steel are considered as inputs. The oil temperature can be further calculated from a detailed thermal model including the winding and core losses that is out of scope of this thesis. In this thesis, the oil temperature is considered constant as an average of top-oil and bottom-oil temperatures for the wall thermal model, as bottom-oil temperature for the bottom thermal model, and top-oil temperature for the cover thermal model. The thermal resistances are non-linear, temperature dependent as will be further discussed in 3.3.2.

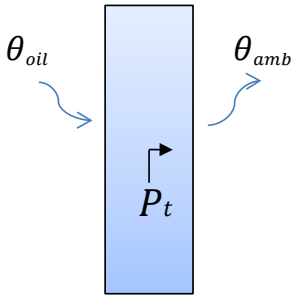

Figure 3.8 Heat transfer through the wall, the θ_{oil} and θ_{amb} are the oil and ambient temperatures

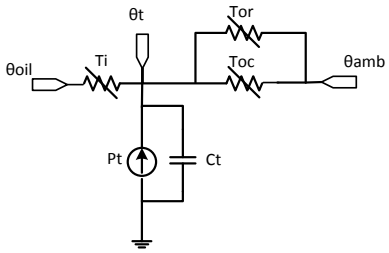

Figure 3.9 Thermal equivalent circuit of the wall

The circuit of Figure 3.9 can be implemented in MATLAB-SIMULINK, as shown in Figure 3.10 (that is based on nodal heat conservative equation), where the look-up tables contain the heat transfer characteristics as curves of the oil-wall and the air-wall temperature

differences versus the heat dissipated due to the convection and the radiation mechanism. Calculation approaches of these thermal characteristics are stated in Section 3.2.2.

The presented thermal model is also appropriate for use for the corrugated walls as well. The impact of the corrugation is primarily on the thermal resistances due to the extension of the wall surface facilitating the heat transfer to the ambient.

There is a two-way coupling between the thermal circuit (Figure 3.9) and the electric equivalent circuit (Figure 3.7) through the wall losses (P_t) and the wall temperature (θ_t) as explained in the following:

1. The circuits start with an initial θ_t which is calculated with $P_t = 0$ assumption. This initial value is set in the integrator block as seen in Figure 3.10 (Right).
2. Once P_t is generated in the wall, θ_t starts increasing, which is used to update the wall steel conductivity.
3. The electric and thermal circuits run simultaneously and the temperature, losses and electric conductivity of the wall are updated at each time step of simulation.

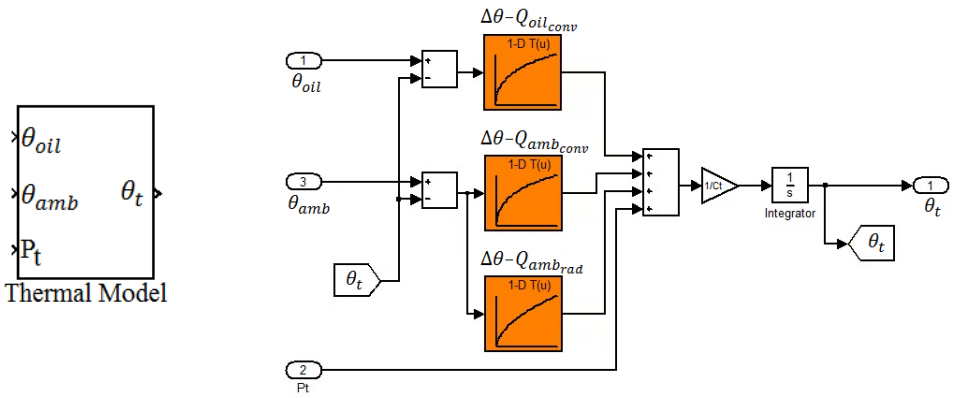

Figure 3.10 Implementation of thermal model in MATLAB-SIMULINK, Left: the overall block, Right: the governing equations implementation inside the Thermal Model block

3.2.2 Calculation approach of the thermal characteristics

3.2.2.1 Convective heat transfer

The focus of the thermal model introduced in Section 3.2.1 is only on the heat transfer from the wall to both the internal and external sides. Only natural convection is considered for the wall regardless of the oil cooling system, since:

- For small and medium power transformers, there is no forced cooling system for both internal (the oil) and external coolants (the air).
- For large power transformers, the cooling of the oil is an independent process where the oil is pumped out of the tank and is cooled off through external radiators. The influence of the external cooling system is considered in the oil temperature, which is considered as an input in the wall thermal model.

Figure 3.11 provides an illustration of heat transfer from the wall surface due to convection. The wall temperature θ_t drops down to the fluid temperature θ_f dissipating Q amount of heat as described with (3.17).

$$Q = h_{conv} A \Delta\theta \tag{3.17}$$

where h_{conv} is the convective heat transfer coefficient, A is the area normal to the heat flow and $\Delta\theta$ is the temperature difference of the wall and the fluid ($\theta_t - \theta_f$).

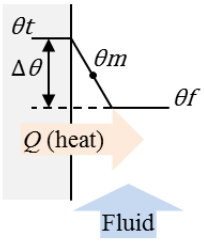

Figure 3.11 Convection heat transfer from the wall surface

The convective heat transfer coefficient is a function of many different parameters including the fluid physical and thermodynamic properties (which are calculated at $\theta_m = \frac{\theta_t + \theta_f}{2}$) as well as the flow type (laminar or turbulent).

To determine h_{conv}, empirical correlation between dimensionless numbers of Nusselt number (Nu) and Rayleigh number Ra (defined as multiplication of Prandtl number (Pr) and Grashof number (Gr)) is used.

The Nusselt number is the ratio of convective to conductive heat transfer across the wall surface defined with (3.18) [86].

$$Nu = \frac{h_{conv} L_c}{k} \tag{3.18}$$

where L_c is the characteristic length, k is the thermal conductivity of the fluid. For vertical plates, the L_c is equal to the plate height. For the horizontal plates, the L_c is calculated as (Plate area)/(Plate perimeter).

The Prandtl number describes the relationships between momentum diffusivity and thermal diffusivity defined with (3.19) [86].

$$Pr = \frac{\gamma \rho c_p}{k} \tag{3.19}$$

where c_p is the specific heat, k is thermal conductivity, γ is kinematic viscosity, ρ is the density of the fluid.

The Grashof number is the ratio of the buoyancy to viscous force acting on a fluid defined with (3.20) [86].

$$Gr = \frac{\beta g \rho \Delta\theta}{\gamma^2} {L_c}^3 \tag{3.20}$$

where β is the coefficient of thermal expansion of the fluid and g is acceleration due to the earth's gravity.

There are different empirical correlations for vertical, horizontal and parallel walls in different fluid flow regimes. The walls can be in the form of either plain or corrugated vertical walls; however, the bottom and cover are considered as horizontal plates.

- **Vertical wall**

For vertical walls with laminar flow regime, the Nusslet number can be expressed by (3.21) [86]. As previously mentioned, the Ra is defined as $Gr \cdot Pr$.

$$Nu_V = 0.678 Ra^{0.25} \left(\frac{Pr}{0.952+Pr}\right)^{0.25} \tag{3.21}$$

where Nu_V denotes the Nusselt number for vertical wall. Once the Nu_V is calculated with (3.21), the convective heat transfer coefficient is obtained by using (3.18).

- **Corrugated vertical wall**

For corrugated walls, the correlation between the Nusselt number (Nu_s) and the Rayleigh number (Ra_s) is expressed by (3.22) [88] [89].

$$Nu_s = \left[\left(\frac{24}{Ra_s}\right)^2 + \left(\frac{1}{0.59 {Ra_s}^{0.25}}\right)^2\right]^{-0.5} \tag{3.22}$$

whereas $Ra_s = \frac{\rho c_p g \beta \Delta\theta S^3}{k\gamma(\bar{L}_s)}$, $\bar{L}_s$ is defined as $\frac{L_c}{S}$ and S is the distance between the fins. Once Nu_s is calculated, the convection coefficient (h_{corr_conv}) is obtained with $Nu_s = \frac{h_{corr\_conv} S}{k}$. The extra area due to the fins can be considered in the factor of $(1 + 2\bar{H}_s)$ where $\bar{H}_s = \frac{H_f}{S}$ and H_f is the fin height. Multiplying $(1+2\bar{H}_s)h_{corr\_conv}$ by the wall area under the fins and temperature difference, the convective heat transferred from the fins is calculated. The wall area under the fins is $(n_f - 4)SL_c$ where n_f is total number of fins on 4 sides of the walls.

- **Horizontal plate**

Correlation between the Nusselt number and the Rayleigh number for horizontal plate is expressed by (3.23) for upward-facing, and with (3.24) for downward-facing convection [90].

$$Nu_{up} = 0.54 Ra^{0.25} \tag{3.23}$$

$$Nu_{down} = 0.27 Ra^{0.25} \tag{3.24}$$

where Nu_{up} and Nu_{down} are the Nusselt numbers in upward and downward convections, respectively.

The outer surface of the bottom and inner surface of the cover are of downward-facing convection type. In contrast to this, the inner surface of the bottom and outer surface of the cover are of upward-facing convection type.

Once the Nusselt number is calculated with either (3.23) or (3.24), the convective heat transfer coefficient is calculated with (3.18) using appropriate characteristic length.

The convection coefficient varies with temperature since the physical thermal parameters of the coolant fluid are temperature dependent. It can be represented with an exponential function such as $a\Delta\theta^b$, and, the heat transferred can be expressed as:

$$Q_{conv} = a\Delta\theta^b \cdot A \cdot \Delta\theta = a \cdot A \cdot \Delta\theta^{b+1} \tag{3.25}$$

As an example, Figure 3.12 shows the h_{conv} calculated with (3.21) and the fitted to $a\Delta\theta^b$ ($a = 1.87$, $b = 0.23$) for the air-cooled vertical wall with a height of 0.4 m. The air physical properties are calculated at the mean temperature of θ_m as given in Appendix 1.

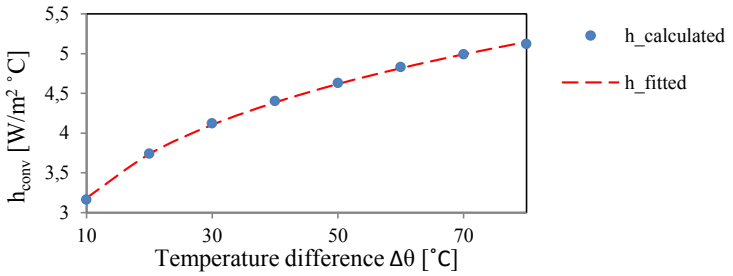

Figure 3.12 Heat transfer coefficient for vertical wall cooled-off with air-natural convection

3.2.2.2 Radiative heat transfer

Radiative heat transfer is an energy exchange between surfaces having different temperatures through electromagnetic waves.

The radiation is more important when temperature difference between surfaces is sufficiently high and the medium in between is sufficiently transparent. In the oil-immersed transformers, the radiation within the tank can be neglected; however, from the outer surfaces of the tank, it can be significant as calculated with the following formulas.

- **Plain wall**

The heat transferred from the plain wall by the radiation is expressed by (3.26) [86].

$$Q_{rad} = \epsilon \cdot \sigma_B \cdot A \cdot (T_t^4 - T_{amb}^4) \tag{3.26}$$

where ϵ is the emissivity of the tank surface and σ_B is the Stefan-Boltzman's constant (5.7×10^{-8} W/m^{2}K^4) T_t and T_{amb} are the tank wall and ambient absolute temperatures in K.

Expanding the term $(T_t^4 - T_{amb}^4)$, (3.26) can be re-written as:

$$Q_{rad} = \epsilon \cdot \sigma_B \cdot A \cdot \left(T_t^2 + T_{amb}^2\right)(T_t + T_{amb})(T_t - T_{amb}) \tag{3.27}$$

Defining the radiative heat transfer coefficient as $h_r = \epsilon \cdot \sigma_B \cdot \left(T_t^2 + T_{amb}^2\right)(T_t + T_{amb})$, the above equation can be re-written as:

$$Q_{rad} = h_r \cdot A \cdot \Delta\theta \tag{3.28}$$

The emissivity ϵ depends on the surface paint color and polishing, and is in the range of 0 to 1. For tanks and radiators painted with gray color, the emissivity is assumed 0.95 [91].

- **Corrugated wall**

When the wall is of corrugated type, the reflections from the inner surfaces of the fins influence the radiation heat transfer from the wall that is considered in a parameter, i.e. the so-called 'view factor' denoted as F_{f-surr} and calculated with (3.29) [92].

$$F_{f-surr} = 1 - \frac{2\bar{H}_s(1+\bar{L}_s^{\,2})^{\frac{1}{2}}-1)}{2\bar{H}_s\bar{L}_s+(1+\bar{L}_s^{\,2})^{\frac{1}{2}}-1} \tag{3.29}$$

where $\bar{H}_s$ and $\bar{L}_s$ are defined under the (3.22).

The heat emitted from each radiator (Q_{fin}) is then calculated with (3.30) [93] [94].

$$Q_{fin} = \sigma_B \cdot \frac{(1+2\bar{H}_s)}{\frac{1-\epsilon}{\epsilon}+\frac{1}{F_{f-surr}}} \cdot S \cdot L_c(T_t^4 - T_{amb}^4) \tag{3.30}$$

from which the radiative coefficient is obtained as $h_{r,fin} = \frac{\sigma_B(1+2\bar{H}_s)(T_t^2+T_{amb}^2)(T_t+T_{amb})}{\frac{1-\epsilon}{\epsilon}+\frac{1}{F_{f-surr}}}$.

Multiplying the Q_{fin} by $(n_f - 4)$ (or multiplying the $h_{r,fin}$ by wall area under the fins and temperature difference), gives total heat emitted from the wall fins.

As an example, Figure 3.12 shows a typical h_r as a function of $\Delta\theta$ for $T_{amb} =$ 20 °C (293 K) and $\epsilon = 0.95$. The curve is well fitted to an exponential function of $ae^{b\Delta\theta}$ (a and b are fitting parameters) with $a = 5.475$ and $b = 0.0049$.

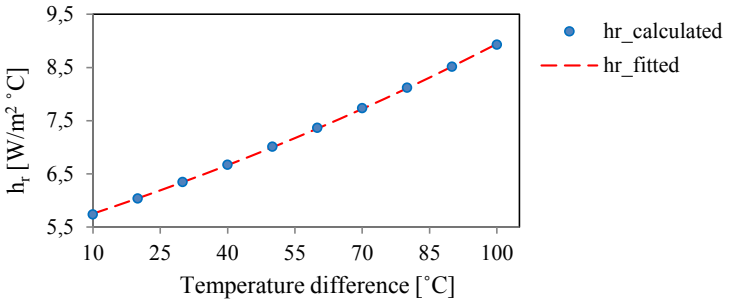

Figure 3.13 Radiation heat transfer coefficient, markings: calculated values, dashed trace: fitted by $ae^{b\Delta\theta}$ with parameters $a = 5.475$ and $b = 0.0049$.

3.2.2.3 Thermal capacitance of the wall steel

Thermal capacitance of the tank steel is calculated with (3.31) [86].

$$C_t = \rho_t \cdot c_p \cdot Vol_t \tag{3.31}$$

where ρ_t is the steel density, c_p is the specific heat capacity and Vol_t is the steel volume.

3.2.2.4 Calculation of initial temperature of the wall

As can be seen in Figure 3.10, there is an integrator through which the wall temperature is computed. Initial condition of this integrator is in fact the initial temperature of the tank that can be calculated through a nonlinear equation of (3.32), which is obtained from Figure 3.9 at steady state assuming that the heat generated in the wall is zero ($P_t = 0$).

$$Q_{oil_{conv}}(\theta_t - \theta_{oil}) + Q_{amb_{conv}}(\theta_t - \theta_{amb}) + Q_{amb_{rad}}(\theta_t - \theta_{amb}) = 0 \tag{3.32}$$

where $Q_{oil_{conv}}$ represents convective heat transfer from the oil to the wall, $Q_{amb_{conv}}$ and $Q_{amb_{rad}}$ represent, respectively, convective and radiative heat transfer from the wall to ambient. Each of these terms is stated with graphs as a function of temperature differences as presented in Sections 3.2.2.1 and 3.2.2.2.

Equation (3.32) is solved iteratively for θ_t when θ_{oil}, θ_{amb} and the heat transfer graphs ($Q_{oil_{conv}}$, $Q_{amb_{conv}}$, $Q_{amb_{rad}}$) are given as inputs. Figure 3.14 shows an implementation of this equation in MATLAB-SIMULINK.

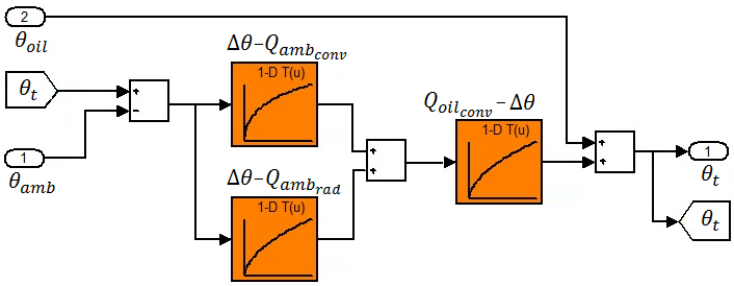

Figure 3.14 Computation of initial wall temperature based on oil and ambient temperature inputs

Chapter 4

Tests and measurements

4.1 Electric and magnetic measurements on tank steel

Three typical steels, which are used in transformer tank, with thicknesses of 1.25 mm, 4 mm and 6 mm, are selected as shown in Figure 4.1. All samples are 50 mm width and 150 mm length. The 1.25 mm thick steel is identified by the manufacturer code of DC01 (cold-rolled) and two others are of Laser Plus 250C (hot-rolled) corresponding to standard codes of ST1203 (DIN 1623) and S235J2C (EN 10025-2), respectively [95] [96].

Figure 4.1 Specimens of the tank steels with thicknesses of 1.25 mm (Left), 4 mm (Middle) and 6 mm (Right)

Both DC and AC measurements are performed on these samples by means of a commercial measuring system, namely MPG 100D, AC–DC [97] and using a single-sheet tester (SST), which has been specially ordered from Brockhaus Measurements to design and build for a 50×150 mm sample dimension complying with IEC 404-3 (see Figure 4.2) [98]. Both primary and secondary windings have 150 turns. The frequency in the quasi-DC measurements is about 0.125 Hz, thus ensuring minor skin effects in the thick samples. Figure 4.3 and Figure 4.4 show static and dynamic (at 50 Hz) hysteresis loops at various excitations for the 1.25 mm and 4 mm thick samples, respectively. As can be seen, the hysteresis loops become wider due to the dynamic losses including classical eddy current and excess losses. Figure 4.5 shows the B-H normal curves. The initial part of the B-H characteristics is more realistically represented by means of the normal curve rather than the anhysteretic curve. Since the magnetic flux involving the tank walls varies in a wide range from very low to high values, the normal curve is a proper representation of the tank steel. Insufficient capability of anhysteretic curve in reproducing open-circuit zero sequence impedance particularly at lower excitations is also shown in [69].

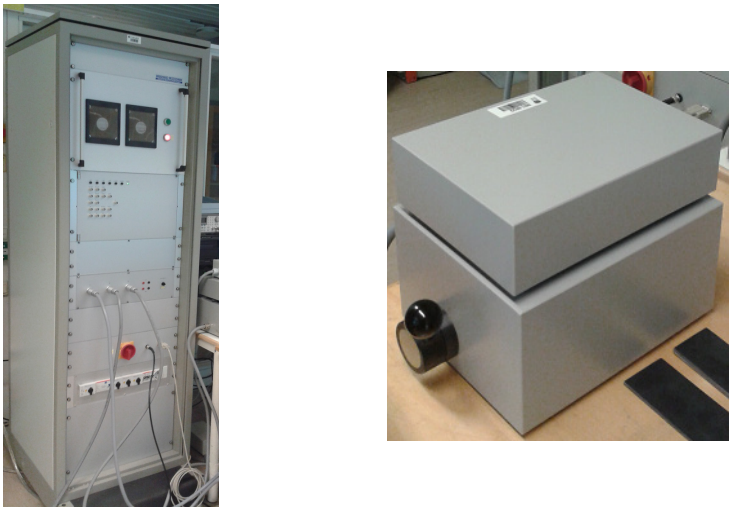

a) b)

Figure 4.2 The equipment used for the measurements: a) the tester MPG 100D, and b) the SST

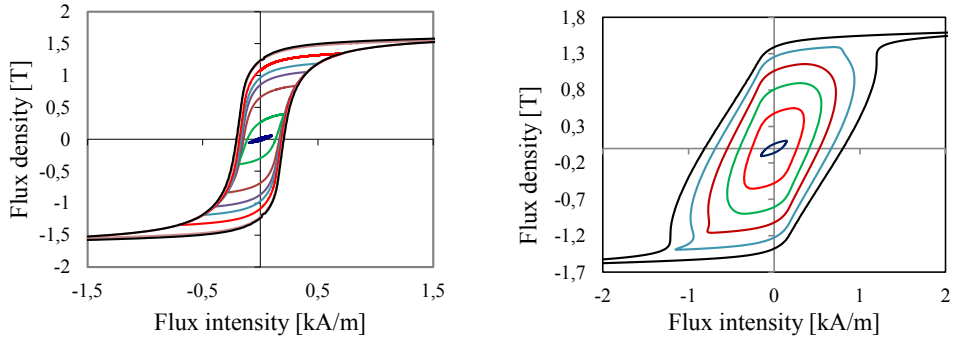

Figure 4.3 Hysteresis loops: Left: static, Right: dynamic (50 Hz), for the 1.25 mm thick sample

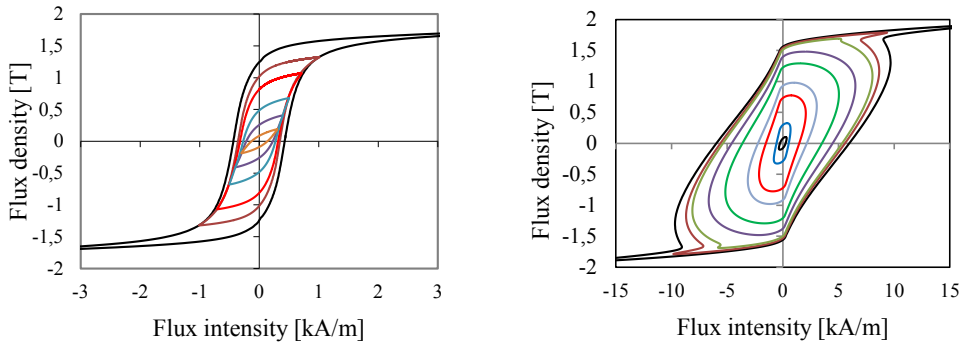

Figure 4.4 Hysteresis loops, Left: static, Right: dynamic (50 Hz) for the 4 mm thick sample

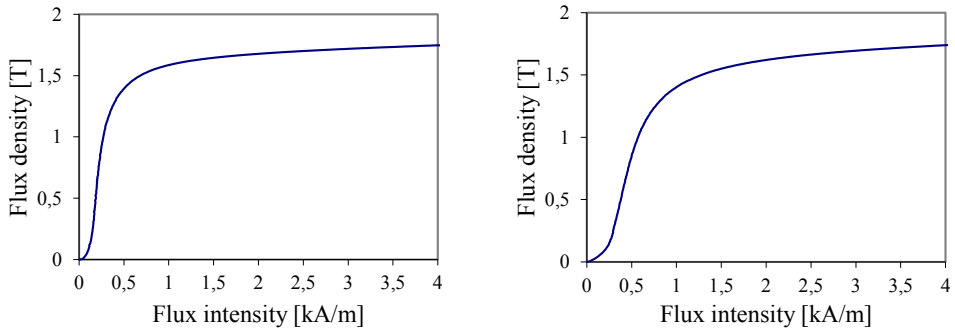

Figure 4.5 Magnetic normal curves, Left: the 1.25 mm thick sample, Right: the 4 mm thick sample

4.1.1 DC energy losses

Figure 4.6 shows the major static hysteresis loops measured for the 1.25 mm and 4 mm samples. As can be seen, the coercive force (H_c) of the thicker material is about twice that of the thinner one; however, the residual flux (B_r) is identical for both samples. The energy losses of hysteresis corresponding to the static hysteresis loops at different inductions are shown in Figure 4.7.

In order to characterize the hysteresis loss, the classical formula of $E = K_h B_m^n$ with constant K_h and induction-dependent exponent (n) is examined. Through using a non-linear least square method, the best fit is obtained when the exponent n is a third-degree polynomial expression of $a + bB_m + cB_m^2 + dB_m^3$, as shown in Figure 4.7. The fitting parameters obtained for the samples are given in Table 4.1.

Table 4.1 Fitting parameters of the hysteresis losses function

Sample / Coefficients	K_h	a	b	c	d
1.25 mm	83.3	1.8	-2.1	2.8	-0.9
4 mm	142.2	1.81	-1.1	1.14	-0.31

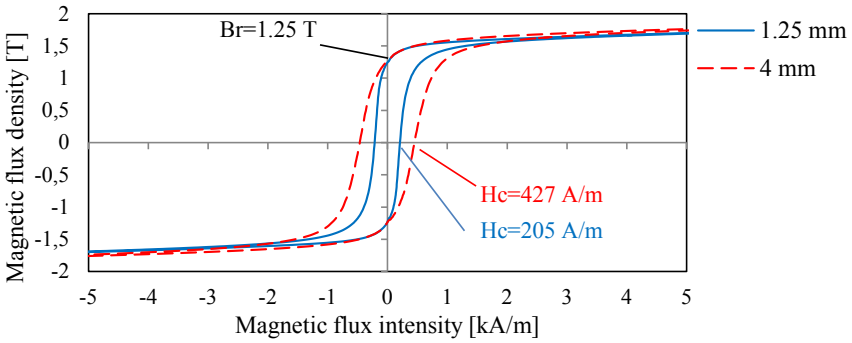

Figure 4.6 Static hysteresis loops of the 1.25 mm (dashed trace) and the 4 mm (solid trace) samples

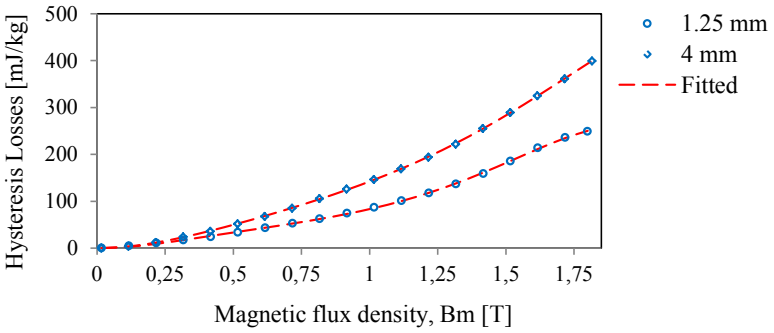

Figure 4.7 Energy losses corresponding to static hysteresis loops, measured values and fitted curves

4.1.2 Dynamic losses

In order to investigate the dynamic losses, three frequencies of 50 Hz, 100 Hz and 150 Hz are chosen and the losses are measured for the 1.25 mm and 4 mm samples. The AC measurements of the sample of 6 mm thickness were only performed at 50 Hz, because the heat generated would become very high, thus exceeding the equipment limits at higher frequencies. Major hysteresis loops for the 4 mm sample at different frequencies are shown in Figure 4.8. The total magnetic losses (comprising hysteresis, classical eddy current and excess losses) versus maximum flux density for the 1.25 mm and 4 mm samples are shown in Figure 4.9. As can be seen, the losses in the 1.25 mm sample are much lower than that of the 4 mm thick sample, which is primarily due to higher eddy currents in thicker materials.

It must be noted that the *x*-axis in Figure 4.9 includes the peak values of the space average flux density across the thickness of the samples, which is corresponding to the voltage induced in the secondary coil of the SST.

Using the hysteresis energies from static measurements (see Figure 4.7) and multiplying by frequency, hysteresis losses are calculated. The accuracy of this approach is confirmed in [99], where a magneto-dynamic hysteresis model was used to simulate magnetic losses. Subtracting the hysteresis losses from the total losses, the dynamic losses can be separated as $P_{dyn} = P_{tot} - P_{hys}$.

Figure 4.10 shows the ratio of the dynamic losses to the total losses, as explained below.

1. As expected, the ratio is higher for the thicker samples due to higher eddy currents. It reduces from 95% and 90% at higher inductions to about 80% and 70% at induction 0.22 T for the samples of, respectively, 6 mm and 4 mm thickness. Through these results, it is possible to assume that the hysteresis losses can be neglected without making significant errors.
2. The ratio is relatively lower for the 1.25 mm thick sample. It reduces from 70% at higher inductions to about 15% at 0.1 T. This means that the hysteresis phenomenon has the same degree of significance as the dynamic losses in the thinner tank walls at lower inductions. It must be noted that the flux is assumed axial along the long side of the samples neglecting the flux bending at the ends. In the actual tank walls, the flux enters through multiple points into the wall, then flows axially. The eddy current losses at the entrance area are not seen in the measurements due to the structure of the SST as well as in the presented calculations in which the axial flux flow is the main assumption. Therefore, the dynamic losses part of the total losses is expected to be higher than those shown in Figure 4.10. In addition, the total losses are not even considerable at low inductions (where the hysteresis phenomenon is more significant) let alone the dynamic losses. Hence, it does not problematical to disregard the hysteresis losses.
3. At lower inductions below 0.22 T for the 4 mm and 6 mm samples and below 0.1 T for the 1.25 mm sample, the ratio starts increasing again despite of the decreasing trend. This behavior can be explained with the initial lower permeability resulting in deeper flux penetration at lower inductions. This leads to an increase in the eddy currents and consequently in the losses.
4. The loss ratio curve is flattened at higher inductions. This means that the rate of rise of the losses (mainly eddy current losses) is adversely affected by another factor, which appears at higher losses. This factor is in fact the temperature in the samples that increases with the losses. The temperature rise has a negative feedback on the conductivity (it reduces with temperature). The lower the conductivity, the lower the resulting losses. That is because the rate of rise of the losses continually decreases with induction increase.

In order to investigate the thermal influence of the losses, the temperature of the specimens is also recorded during the measurements. The temperature reaches beyond 100 °C at 150 Hz for the 4 mm sample due to the considerable losses at such a frequency. Figure 4.11 shows the temperature graph versus the maximum flux density for each sample. This temperature data will be used for correction of the conductivity in the calculation of the eddy current losses.

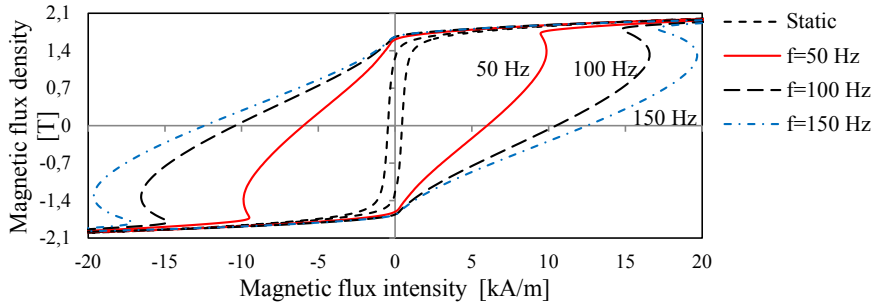

Figure 4.8 Dynamic hysteresis loops for the 4 mm thick sample

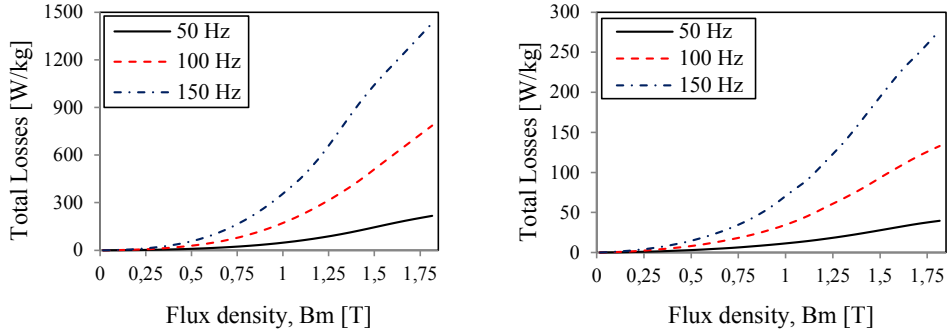

Figure 4.9 Total losses, Left: for the 4 mm thick sample, Right: for the 1.25 mm thick sample

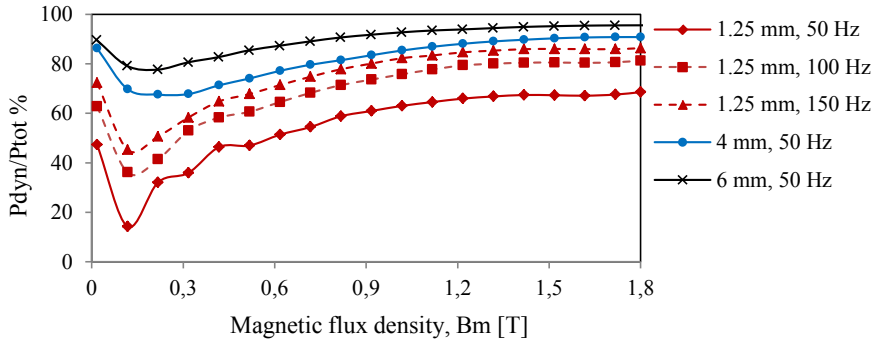

Figure 4.10 The ratio between the dynamic losses and the total losses

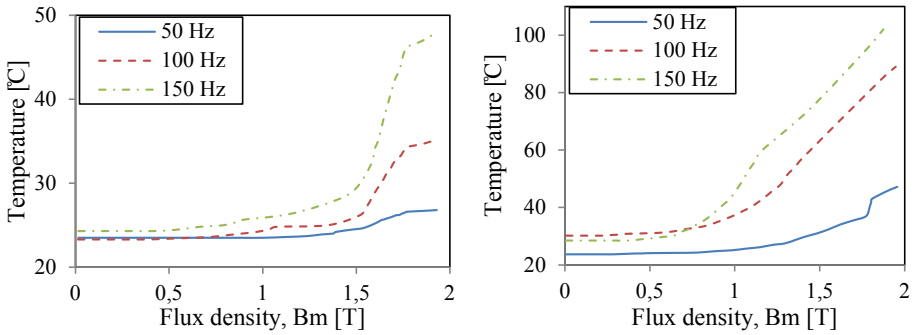

Figure 4.11 Temperature of the specimens during magnetic measurements, Left: for the 1.25 mm sample Right: for the 4 mm sample

4.1.3 Electrical conductivity measurements

To measure the conductivity, DC currents of 20 A, 30 A, 40 A and 50 A are injected into the samples at an ambient temperature of 20 °C. In order to prevent the end effects and to ensure that the current is distributed evenly across the thicknesses of the samples, the voltage drop is measured at the middle between two points with 6 mm distance. The measurement setup is illustrated in Figure 4.12 (Left). Plotting the voltage versus current, the Volt-Amp (V-I) characteristic of each steel sample is obtained. Fitting this characteristic to the linear relation of $V = aI + b$, the resistance (*a*) and the voltage offset (*b*) are identified. As an example, Figure 4.12 (Right) shows the V-I characteristic for the 4 mm sample. The fitting parameters are: a = 4.56e-5 Ω and b = −7.67e-5 V. Once the resistance is obtained, the conductivity can be calculated using the formula $length/(\sigma \cdot Area)$ resulting in 6410 kS/m for the 4 mm and 5820 kS/m for the 1.25 mm samples. Using the same approach at different ambient temperatures (the measurement setup is put in the oven, which provides uniform ambient temperature), the conductivity temperature coefficient (at 20 °C (α_{20})) is obtained as 0.0084 °C^{-1} and 0.0065 °C^{-1} for the 1.25 mm and 4 mm samples, respectively.

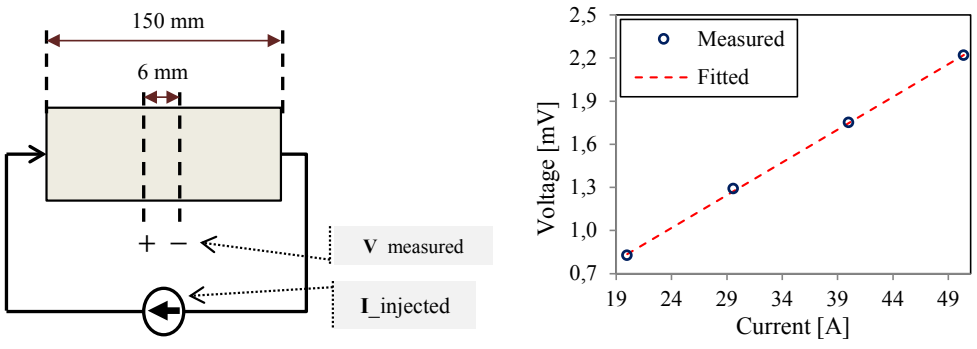

Figure 4.12 Conductivity measurement, Right: test setup, Left: V-I characteristics measured for the 4 mm thick sample

4.1.4 Analytical formula for excess losses

This section presents a formula for calculation of the excess losses at the steady state for the 1.25 mm and 4 mm samples. The formulas are obtained by fitting into the simulation results presented in the previous section. Figure 4.13 shows the excess losses calculated for the 1.25 mm and 4 mm samples at the three frequencies of 50 Hz, 100 Hz and 150 Hz.

Since the temperature and the skin effect play important roles in the losses, the conventional expression of kB_m^n (in which k and n are constant parameters) is not sufficient to represent the losses as a function of induction, as illustrated by the green dashed lines in Figure 4.13.

The best fitting is obtained with a modified equation expressed in (4.1).

$$P_{exc} = kB_m^n/(1 + aB_m + bB_m^2) \tag{4.1}$$

where k, n, a and b are fitting parameters and P_{exc} is the excess loss.

Good fitting capability of (4.1) can be seen in Figure 4.13 where the fitted curve is plotted as solid-blue lines. The fitting parameters are presented in Table 4.2. As can be seen, the parameter b is not frequency dependent, but the rest parameters change with frequency. Performing the measurements at higher frequencies was not practically possible due to high temperature generated by the losses, and hence, there would not be enough data to investigate frequency dependency of the parameters.

Table 4.2 Coefficients of the Excess Loss found by fitting

Frequency	Sample thickness	*k*	*n*	*a*	*b*
150Hz	4 mm	2,0	4,9	-1,24	0,45
	1,25 mm	7.6	2,3	-0,9	0,3
100 Hz	4 mm	0,19	7,67	-1,28	0,45
	1,25 mm	3,5	2,7	-0,9	0,3
50 Hz	4 mm	0,01	8,75	-1,32	0,45
	1,25 mm	1,1	2,8	-0,9	0,3

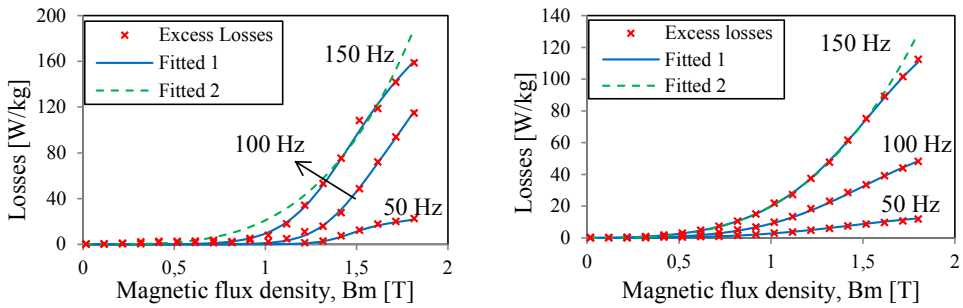

Figure 4.13 Excess losses for the 4 mm samples (Left) and the 1.25 mm sample (Right) - 'Fitted 1' is based on $P_{exc} = kB_m^n/(1 + aB_m + bB_m^2)$, 'Fitted 2' is based on $P_{exc} = kB_m^n$

4.1.5 Characterization of the dynamic losses

To reproduce the losses, a simple model of the SST unit is considered to comprise an exciting winding wrapped around the steel sample assuming that no leakage flux exits [100]. The model is implemented in MATLAB-SIMULINK using the numerical approach presented in Chapter 3, Section 3.1. Assuming the functions of *B* and *H* symmetric about the plane passing the half thickness, the one-dimensional magnetic diffusion equation is solved in the segment of $[0, \frac{Specimen\ thickness}{2}]$. The boundary conditions set to the first and last layers of this model are as expressed in (4.2) and (4.3), respectively [101].

$$\frac{dB_1}{dt} = \frac{8H_2\text{-}7H_1\text{-}H_3}{2\sigma\Delta x^2} + \frac{3(n\text{-}1)}{N\cdot A} v_t(t) \tag{4.2}$$

$$\frac{dB_n}{dt} = \frac{2(H_{n-1}\text{-}H_n)}{\sigma\Delta x^2} \tag{4.3}$$

where $v_t(t)$ is the voltage applied to the excitation winding, N(=150) is the number of turns, A(=50×150×10^{-6}m^2) is the cross section of the steel sample normal to the flux flow direction. Figure 4.13 shows the block diagrams of the model. As can be seen, maximum values of the average flux density (B_m) are used as a breakpoint to the look-up table $Temp - B_m$, which includes temperature as a function of maximum flux density from the measurements, see Figure 4.11. The temperature obtained from the look-up table is fed back to correct the conductivity at each time step of the simulations. The average losses are calculated using equation $\frac{1}{T}\int_t^{t+T} v_t(t) \cdot i_x(t)dt$ where T is the period and i_x is the current that can be i_{cl}, i_{texc} and i_t for classical eddy current loss, excess loss and total losses, respectively.

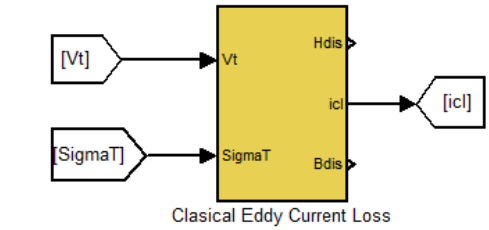	• Model of the classical eddy losses based on the approach presented in Section 3.1.1 with boundary conditions described in (4.2) and (4.3) • 'SigmaT' is the conductivity corrected by the temperature • v_t is the voltage applied to the excited • i_{cl} is the classical eddy current
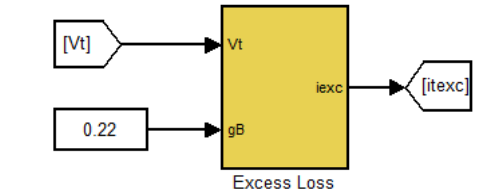	• Model of excess losses based on the approach presented in Section 3.1.3 • 'g_B' is the excess losses coefficient that is tuned during simulations • v_t is the voltage applied to the winding excited • i_{exc} is the excess current
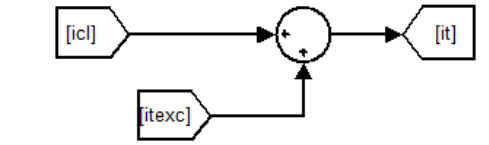	• The classical eddy current adds to the excess current resulting in the total magnetization current
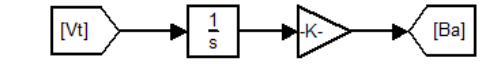	• Space average flux density based on (3.14) • The gain block is $\frac{1}{N\times 50\times 150\times 10^{-6}}$ where N =150 (turn number of the excitation winding)
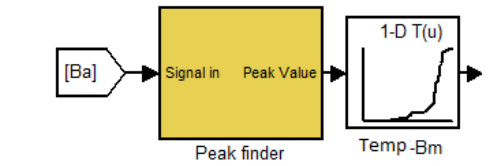	• The block 'Peak finder' finds the peaks of the Space average flux density • The look-up table describes the temperature versus the maximum induction given in Figure 4.11
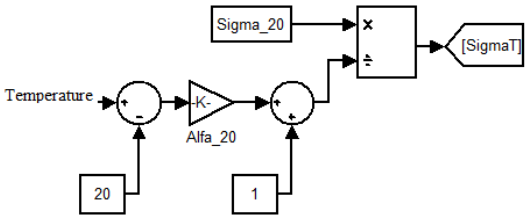	• 'Sigma20' is the conductivity of the samples at 20 °C • 'SigmaT' is the conductivity corrected by temperature • 'Alfa20' is the conductivity temperature coefficient α_{20} given in Section 4.1.3

Figure 4.14 Simple model of the SST for reproducing the measured dynamic losses

Figure 4.15 shows the distribution of magnetic flux density across the half thickness of the 4 mm sample illustrating how the flux is penetrating into the steel. The red solid trace is the average flux density across the sample thickness.

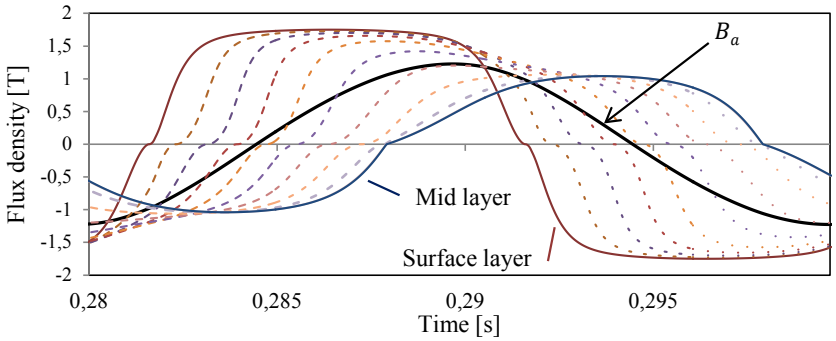

Figure 4.15 Distribution of the flux density across the half thickness of the 4 mm sample at frequency 50 Hz, black solid trace is the average flux density (B_a) across the sample thickness

Figure 4.16 and Figure 4.17 show the classical eddy current losses versus the B_m as calculated for the 4 mm and 1.25 mm samples at 50 Hz, 100 Hz and 150 Hz. In order to see the impact of temperature, the classical eddy current losses are calculated with and without temperature correction at 150 Hz. As can be seen in Figure 4.16, if the conductivity correction was not considered, the eddy current losses would become even greater than the total dynamic losses, which cannot be correct. The temperature is of high significance at higher inductions and frequencies demonstrating the importance of the temperature correction, and thus, the thermal modeling of the tank walls.

It is worth mentioning that the temperature has negligible impact on the hysteresis energy losses when the maximum induction (B_m) is maintained constant [102].

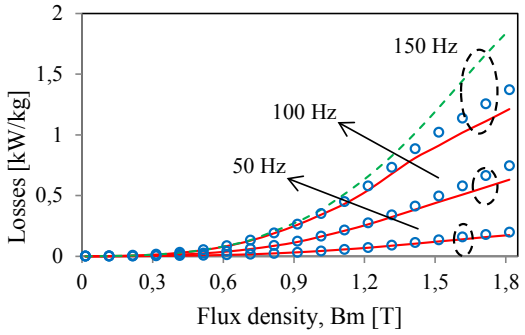

Figure 4.16 Classical eddy current losses calculated for the 4 mm sample, markings are the total dynamic losses from the measurement, dashed trace is the losses with no conductivity temperature correction, solid trace is the eddy current losses with the conductivity corrected by temperature

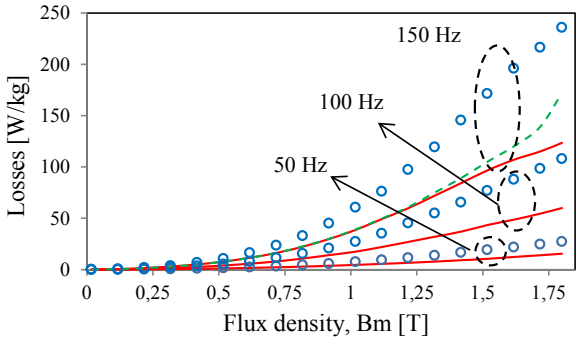

Figure 4.17 Classical eddy current losses calculated for the 1.25 mm sample, blue-markings are the total dynamic losses measured; green-dashed trace is the losses with no conductivity temperature correction; red-solid trace is the eddy current losses with the conductivity corrected by temperature

As explained in chapter 3, the excess losses coefficient gB is a function of flux density. In the simulations, this coefficient is considered to be as a tuning parameter to fit the calculated total losses to the measured values. Figure 4.18 shows the total losses calculated for the 1.25 mm sample with different gB at the frequency 50 Hz. As can be seen, it varies from 0.05 at lower inductions to 0.22 at higher inductions to fit the calculations to the measurement. The gB versus B_m can be fitted by a second-degree polynomial expression of $aB_m^2 + bB_m + c$ using the method of least squares. The fitting result is shown in Figure 4.19 and the fitting parameters identified are given in Table 4.3.

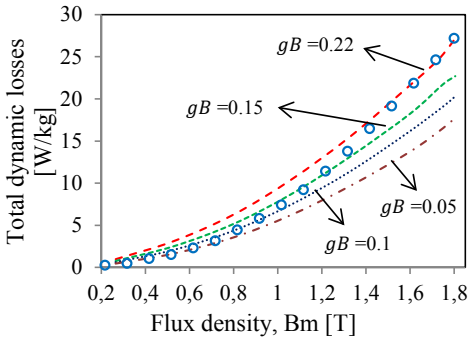

Figure 4.18 Total dynamic losses of the 1.25 mm sample at 50 Hz, blue-markings are the measured losses

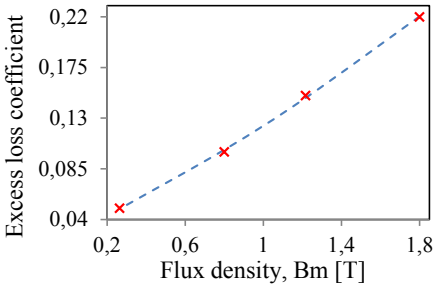

Figure 4.19 Excess losses coefficient as a function flux density for the 1.25 mm sample at 50 Hz, red-markings are from simulation results, blue-dashed line is the fitted by $aB_m^2 + bB_m + c$

Repeating the calculations with the induction dependent gB, see Figure 4.19, the losses are calculated as shown in Figure 4.19 for the 1.25 mm sample. The classical eddy current losses together with the excess losses are also shown in Figure 4.19.

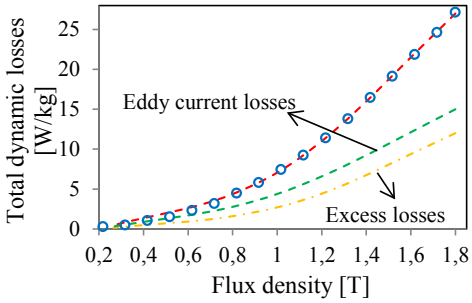

Figure 4.20 The total dynamic losses, measured against the simulated losses components of the 1.25 mm sample at 50 Hz, blue-markings are the measured and the red-dashed trace is the simulated

In the same fashion, the excess losses coefficient is obtained for the 4 mm sample, as shown in Figure 4.21 (Left). It can be fitted by expression aB_m^b with the fitting parameters given in Table 4.3. Using this induction dependent coefficient, the losses are calculated as shown in Figure 4.21 (Right).

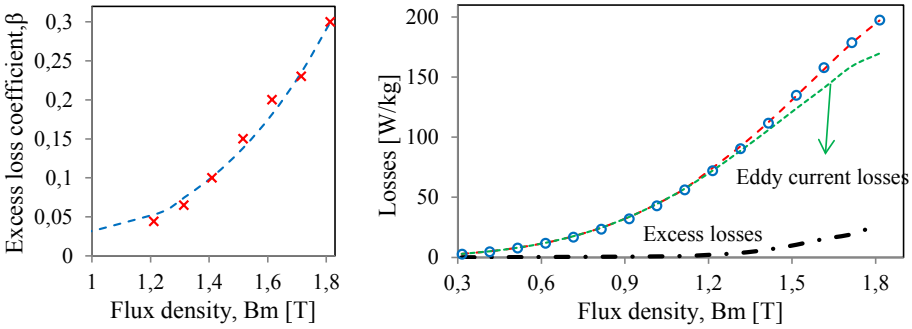

Figure 4.21 Left: The excess losses coefficient gB as a function of induction where red-markings are simulated and blue-dashed is the fitted, Right: Total dynamic losses, blue-markings are the measured and the red-dashed trace is the simulated for the 4 mm sample at 50 Hz

Table 4.3 Fitting parameters for excess losses coefficients

Sample / Coefficients		*a*	*b*	*c*
1.25 mm	$aB_m^2 + bB_m + c$	0.014	0.084	0.026
4 mm	aB_m^b	0.023	4.31	-

As can be seen in Figure 4.20 and Figure 4.21 Right, the excess losses have a relatively larger part of the total dynamic losses for the 1.25 mm sample. It means that the excess losses must be considered in the modeling of the tank walls as thick as 1.25 mm. However, the excess losses are negligible for the 4 mm sample at inductions less than 1.4 T. It starts to appear at inductions over 1.4 T and increases up to 13.9% of the total dynamic losses at

induction 1.8 T. It means that it is possible to ignore the excess losses for the tank walls with thicknesses of 4 mm and above, which is normally the case for large power transformers.

4.1.6 Temperature impact on the conductivity

The electric conductivity of the wall steel is temperature dependent, which can be expressed as (4.4):

$$\sigma = \frac{1}{1 + \alpha_{20}(\theta_t - 20)}\sigma_0 \tag{4.4}$$

where α_{20} is the temperature coefficient at 20 °C, σ is the conductivity at temperature θ_t and σ_0 is the conductivity at 20 °C.

Figure 4.22 shows the conductivity versus temperature for both 1.25 mm and 4 mm samples. As can be seen, the conductivity can reduce to 4044 kS/m and 3314 kS/m for the 4 mm thick and 1.25 mm thick steels, respectively, when temperature reaches 110 °C.

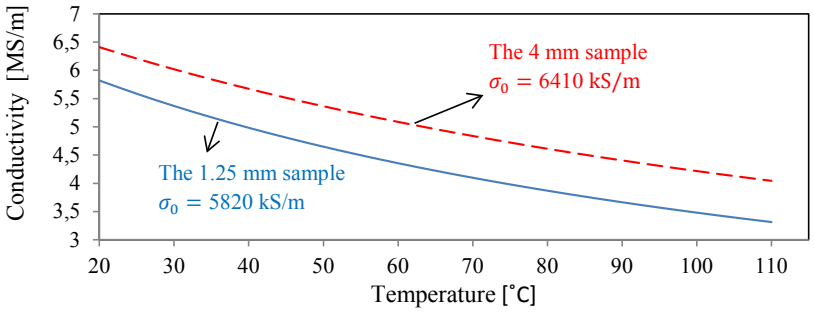

Figure 4.22 Wall steel conductivity as a function of temperature

4.1.7 The wall corrugation impact on the conductivity

The path of the current induced in the corrugated walls can become much longer than that of a plain wall, as shown in Figure 4.23. In this case, the length of the current path can still be kept equal to the tank circumference, but the surplus length due to the fins can be considered in the electric conductivity of the wall steel, as expressed in (4.5).

$$\sigma^* = \frac{l_C}{l_{eff}}\sigma \tag{4.5}$$

where σ^* is the conductivity of the equivalent plain wall, σ is the conductivity of the wall steel, l_{eff} is the effective length of the wall calculated with $l_f + l_C$ where l_C is the circumference of the tank and l_f is the total length of the fins.

The l_f can be calculated with (4.6):

$$l_f = 2n_f H_f \tag{4.6}$$

where n_f is the number of fins and H_f is the fin height.

As an example, for l_C =2880 mm, n_f = 44 and H_f =120 mm, the l_f is calculated as 10560 mm. The corrugation factor of conductivity becomes $\frac{l_C}{l_{eff}} = \frac{2880}{2880+10560} \approx 0.2143$. For conductivity σ = 5820 kS/m, σ^* is calculated as 0.2143×5820 ≈ 1247 kS/m. This can be as low as 710 kS/m when the wall temperature increases up to 110 °C. Such a low conductivity can considerably reduce the current induced in the wall and consequently the losses.

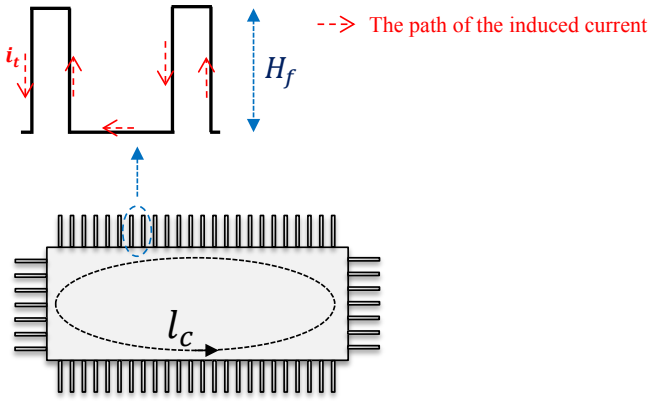

Figure 4.23 The corrugated tank wall, the path of current induced in the wall

4.2 Zero sequence impedance tests on Unit 1 and Unit 2

In order to verify the off-core path model developed in Chapter 3, two 3-phase transformers of 300 kVA (termed Unit 1 from now onwards) and 5 MVA (termed Unit 2 from now onwards) with 3-legged core construction are considered. Table 4.4 summarizes the main characteristics of these units. In order to perform the ZS impedance test, the terminals of the windings to be excited connect together and single-phase test voltage is applied between the common point of terminals and the ground terminal, as shown in Figure 4.24 [23]. Measuring the current at the common point (I_0), the impedance per phase can be calculated with $Z_0 = 3 \times \frac{V_0}{I_0}$. In addition to the impedance, the total losses are also measured at the common point of connection. Using both the impedance and the losses, the parameters of the off-core model are identified, as illustrated in Chapter 6.

Unit 1 is the main test object for verifying the model developed in this thesis. Zero-sequence impedance test results of Unit 1 including OC-ZS and SC-ZS impedances are available for both LV and HV sides. The OC-ZS tests at the LV side (among other tests) were performed as a Master's thesis work and presented in [103]. The HV side measurements are performed as a part of this PhD work. The impedance and the losses measured on Unit 1 versus the voltage applied are plotted in Figure 4.25. It is worth mentioning that the wall thermal time constant plays an important role when considering the impact of the temperature rise in the test results. The thermal time constant is principally determined by the heat transfer capability of the wall. For the corrugated walls, the heat can be easily transferred to the ambient because of the extended outer surface of the wall (the fins). As will be shown in Section 6.1.2, the wall time constant of Unit 1 is in the range of

few minutes (about 2.5 minutes), which is sufficiently short to be seen in the test results of Unit 1.

The ZS impedance of Unit 2 is measured from the LV side as 0.55 Ω where the delta connected HV windings provides a short-circuited path for the induced zero sequence currents [33]. Temperature dependency of the off-core impedance does not influence the test results noticeably since the off-core flux path is bypassed by a D-connected, HV winding. This Unit will only be used in Section 5.1 where the properties of the model linear inductances are discussed.

Table 4.4 Characteristics of the sample transformers

	Unit 1	Unit 2
Power	300 kVA	5000 kVA
Vector group	Y_N-y_n 0, D-y_n 11	D-y_n 11
Voltage ratings	HV (Y): 11.43 kV, HV(D): 6.6 kV LV: 0.235 kV	HV (D): 33 kV LV (Y): 6.3 kV
Current rating	HV (Y): 15.2 A LV: 737 A	HV (D): 87.5 A LV (Y): 458.2 A
Cooling	ONAN	ONAN
Wall type/thickness	Corrugated/1.25 mm	Plain/6 mm
HV winding resistance	2.5 Ω/phase	1.5 Ω/phase
LV winding resistance	0.0009 Ω/phase	0.013 Ω/phase

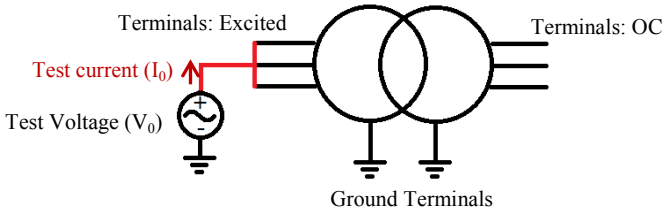

a) Test circuit for OC-ZS impedance

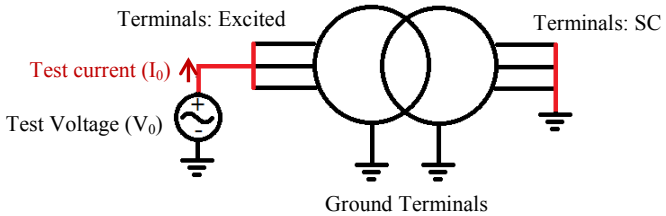

b) Test circuit for SC-ZS impedance

Figure 4.24 Test circuits for zero-sequence impedance measurements [23]

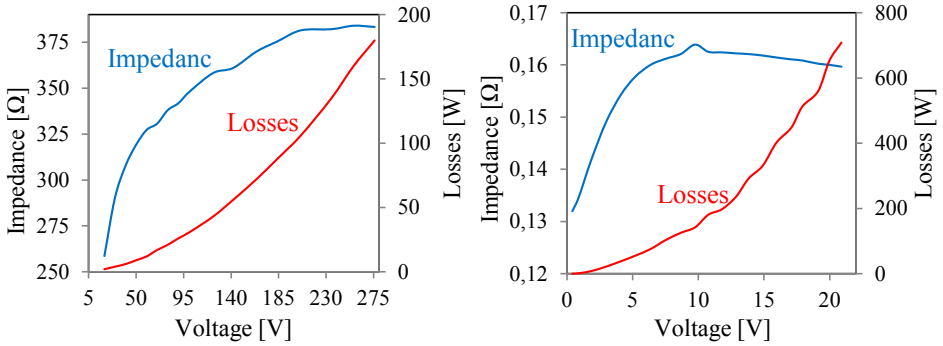

Figure 4.25 OC-ZS impedance and losses of Unit 1 measured at the LV side (Right) and HV side (Left)

To easily compare OC-ZS inductances seen from each side, HV side measurements are referred to the LV side (using the turns ratio) and plotted in the same figure as the LV side measurements, as shown in Figure 4.26.

In addition, SC-ZS impedance is also measured from the HV side of Unit 1 at different voltages, as shown in Figure 4.27.

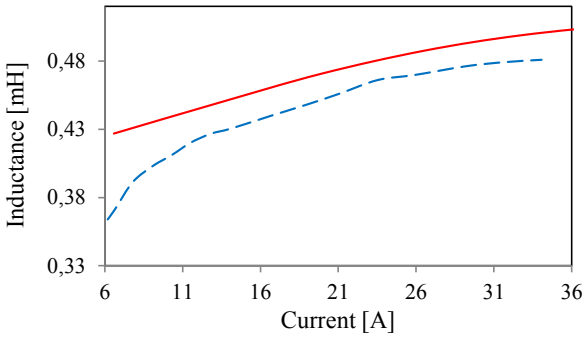

Figure 4.26 OC-ZS inductance seen from the LV side (solid trace) and HV side (referred to LV and shown as dashed trace) of Unit 1

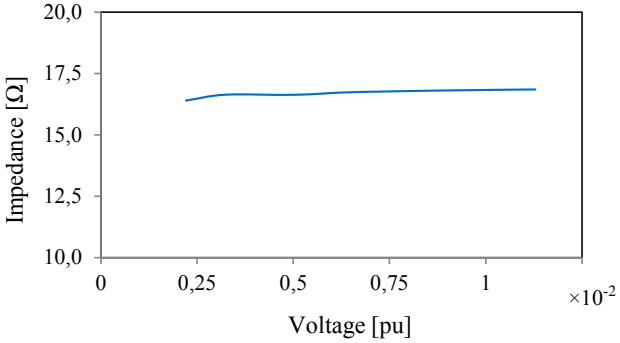

Figure 4.27 SC-ZS impedance seen from the HV side (LV short-circuited) - Unit 1

Chapter 5

Evaluations and discussion on the parameters

5.1 Parameters of the oil gaps (Linear inductances)

As discussed in Chapter 3, there are two sets of branches in the equivalent circuit of the off-core flux path (see Figure 5.1). The first set includes linear inductances corresponding to the oil gap between the active part and the tank walls. A calculation approach of these linear inductances is presented in this section based on the 3D-FEM method. This 3D model consists of the windings and the core; the inner surfaces of the tank walls are considered as the model boundary. As explained in the following sections, through the use of a set of flux-tangential and flux-normal boundary conditions, the linear inductances are calculated.

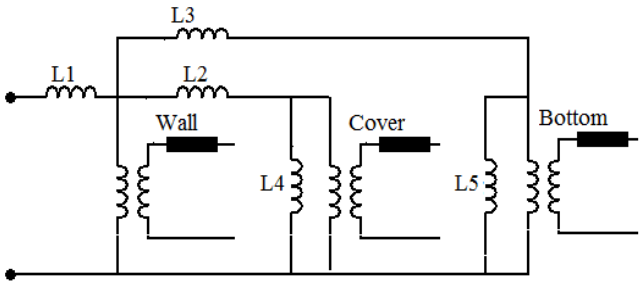

Figure 5.1 The off-core equivalent circuit

5.1.1 Calculation of L_1

L_1 represents the parallel flux path between the winding excited and the wall's inner surfaces. In order to calculate this parameter, flux-tangential boundary conditions are set to the tank's inner surfaces, meaning that the flux cannot penetrate in the tank. This is equivalent to a non-magnetic material with infinite electric conductivity (and thus, infinitely large eddy currents induced) and zero magnetic permeability (infinitely high reluctance path). As a result, all the tank branches in the circuit of Figure 5.1 can be considered short-circuit and the inductance seen from the terminal becomes L_1.

5.1.2 Calculation of L_2, L_3, L_4 and L_5

Table 5.1 introduces different simulation cases where each corresponds to a set of flux-normal and flux-tangential boundary conditions applied to the tank's inner surfaces. Table 5.1 also includes the case for calculating L_1 as explained in Section 5.1.1. The flux-normal boundary condition implies full flux penetration with no magnetic reluctance and no eddy currents induced. This is equivalent to a material with zero electric conductivity and infinite magnetic permeability resulting in an open-circuit tank branch in the equivalent circuit of Figure 5.1.

Table 5.1 Calculation formulas of linear inductances

	Boundary condition			Terminal inductance from the equivalent circuit, Figure 5.1
	Wall	Cover	Bottom	
Case 1	Normal	Normal	Normal	$L_{T,1} = L_1 + (L_3 + L_5)\|\|(L_2 + L_4)$
Case 2	Tangential	Tangential	Tangential	$L_{T,2} = L_1$
Case 3	Normal	Tangential	Tangential	$L_{T,3} = L_1 + L_2\|\|L_3$
Case 4	Normal	Tangential	Normal	$L_{T,4} = L_1 + (L_3 + L_5)\|\|L_2$
Case 5	Normal	Normal	Tangential	$L_{T,5} = L_1 + (L_2 + L_4)\|\|L_3$

Solving the circuit of Figure 5.1 for each simulation case given in Table 5.1, a set of equations relating the unknowns $L_2 \dots L_5$ to the terminal inductances ($L_{T,i}$ where i is the case number) are obtained. The linear inductances are obtained by solving the set of equations, once the terminal inductances are calculated (by means of 3D-FEM for each simulation case, as stated in Section 5.1.3).

5.1.3 Calculation of the terminal inductances ($L_{T,i}$) using 3D-FEM

In 3-legged core transformers, the reluctance of the core (legs and yokes) is negligible compared to the reluctance of the off-core flux path. Thus, the OC-ZS inductances seen from the windings are in fact equal to the terminal off-core inductances ($L_{T,i}$).

In order to calculate the $L_{T,i}$, a 3D-FEM model of the transformer with five variations are made corresponding to the five cases introduced in Table 5.1. The core is considered as a linear anisotropic material with relative permeability of 50000 in the flux flow direction whereas it is 100 in the other directions (this value is not significant as long as the off-core

flux path is of concern). Since the tank is excluded from the FEM model and the eddy currents' effect on the core is not considered, static formulation of magnetic potential is sufficient for inductance calculations. The inductance matrix of the windings is calculated using the energy method and is expressed by $\bar{L}=\begin{bmatrix} [\bar{L}_{\text{HV}}]_{3\times3} & [\bar{L}_{\text{HV-LV}}]_{3\times3} \\ [\bar{L}_{\text{LV-HV}}]_{3\times3} & [\bar{L}_{\text{LV}}]_{3\times3} \end{bmatrix}_{6\times6}$, where $[\bar{L}_{HV}]_{3\times3}$ is the sub-matrix of three HV windings, $[\bar{L}_{HV-LV}]_{3\times3}$ and $[\bar{L}_{LV-HV}]_{3\times3}$ are the sub-matrices of the mutual inductances between HV and LV windings and $[\bar{L}_{LV}]_{3\times3}$ is the sub-matrix of the LV windings.

The OC-ZS inductance seen from HV is calculated using only the sub-matrix $[\bar{L}_{HV}]_{3\times3}$ since the LV side is open. The HV voltages ($\bar{V}_{HV}$) and currents ($\bar{I}_{HV}$) can be expressed by (5.1).

$$\bar{V}_{HV} = \bar{L}_{HV} \cdot D\bar{I}_{HV} \rightarrow D\bar{I}_{HV} = \bar{\Gamma}_{HV} \cdot \bar{V}_{HV} \tag{5.1}$$

where D is the time derivation operator, and $\bar{\Gamma}_{HV}$ is the reverse inductance matrix ($= \bar{L}_{HV}{}^{-1}$).

When the HV windings are connected together at the terminals and excited with a single-phase voltage of V_0, the current of the i^{th} HV winding ($I_{HV,i}$) can be written as:

$$DI_{HV,i} = \Gamma_{i1}^{HV} \cdot V_0 + \Gamma_{i2}^{HV} \cdot V_0 + \Gamma_{i3}^{HV} \cdot V_0 \rightarrow \frac{DI_{HV,i}}{V_0} = \Gamma_{i1}^{HV} + \Gamma_{i2}^{HV} + \Gamma_{i3}^{HV} \tag{5.2}$$

where Γ_{ij}^{HV} is the $(i,j)^{th}$ element of $[\bar{\Gamma}_{HV}]_{3\times3}$. As be seen in (5.2), the OC-ZS inverse inductance of the i^{th} HV winding is equal to $\sum_{k=1}^{3} \Gamma_{ik}^{HV}$ and thus:

$$L^{HV}{}_{T,i} = (\sum_{k=1}^{3} \Gamma_{ik}^{HV})^{-1} \text{ , } i\text{=1..3} \tag{5.3}$$

where $L^{HV}{}_{T,i}$ is the terminal inductance of the off-core path seen from the i^{th} HV winding.

Using the same approach for the sub-matrix $[\bar{L}_{LV}]_{3\times3}$, the terminal off-core inductance seen from i^{th} LV winding ($L^{LV}{}_{T,i}$) is expressed by:

$$L^{LV}{}_{T,i} = (\sum_{k=1}^{3} \Gamma_{ik}^{LV})^{-1} \text{ , } i\text{=1..3} \tag{5.4}$$

where Γ_{ij}^{LV} is the (i,j)$^{\text{th}}$ element of $[\bar{\Gamma}_{LV}]_{3\times3}$.

5.1.4 Considerations on the off-core terminal inductances

Using the approach stated in Section 5.1.3, the terminal off-core inductances are calculated for the transformers Unit 1 and Unit 2 introduced in Chapter 4, Section 4.2.

All the FEM simulations are performed by means of ANSYS Maxwell [104]. In the simulations, automatic adaptive meshing is used to refine the elements' size in each pass of running until the energy error becomes less than 0.05%. Table 5.2 shows the energy errors obtained for each of the simulation cases. Figure 5.2 shows the model geometry and the meshing quality as performed for Unit 2.

Table 5.2 Energy error obtained in 3D-FEM simulations

	Energy error %		Delta Energy error %	
	Unit 1	Unit 2	Unit 1	Unit 2
Case 1	9.1e-3	23e-3	4e-3	11e-3
Case 2	32.6e-3	1.7e-3	13e-3	1.0e-3
Case 3	9.8e-3	11.5e-3	3.4e-3	9.4e-3
Case 4	20.0e-3	16.8e-3	6.7e-3	14.8e-3
Case 5	21.6e-3	12.1e-3	10.0e-3	1.6e-3

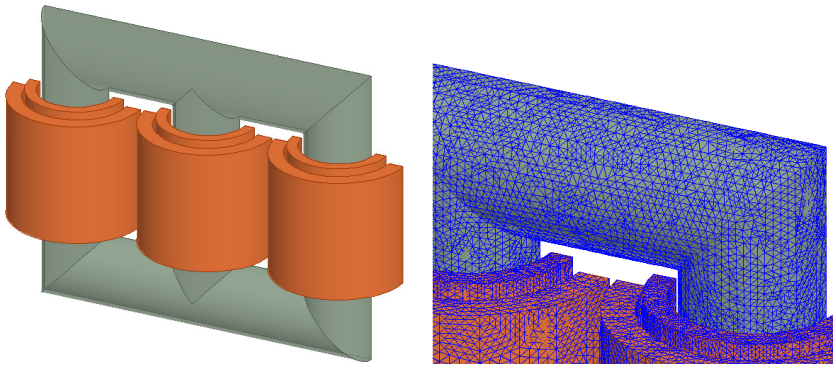

Figure 5.2 Left: 3D model of Unit 2, Right: the meshing of the model

Table 5.3 shows the calculation results seen from HV and LV sides. For ease of comparison of the differences, LV side values are referred to the HV side, as shown in the parentheses. As can be seen, there is a little difference between the inductances of Case 1 and Case 4 as well as Case 3 and Case 5 for both units. For each pair, only the cover has opposite boundary conditions (see Table 5.1). Having almost the same inductance for the abovementioned pairs of the cases implies that the cover is not of significance in the terminal off-core inductances whether the tank is highly magnetically permeable (flux-normal boundary condition) or reluctant (flux-tangential boundary condition). This is because of the large oil-gap between the core top and the cover. As a result, the cover can be excluded from consideration without making any significant errors. However, comparing the values of Case 1 and Case 5 as well as Case 3 and Case 4, large discrepancies are seen in the off-core terminal inductances. In each pair of these cases, only the bottom has opposite boundary conditions, thus implying that the tank bottom cannot be ignored.

Another interesting observation is the relative differences between the off-core terminal inductances seen from LV and HV sides for each simulation case, as calculated with (5.5).

$$E_i\% = \frac{L^{LV}{}_{T,i}(\text{referred to HV}) - L^{HV}{}_{T,i}}{L^{HV}{}_{T,i}} \times 100 \tag{5.5}$$

Figure 5.3 shows the relative differences in percentage for each simulation case. As can be seen, the only meaningful difference between HV and LV values is that of Case 2 where the entire tank is set to a flux-tangential boundary condition. In the remaining cases, the off-core inductances are almost identical with an error less than 3.7% for Unit 1 and 1.26% for Unit 2.

Table 5.3 The off-core terminal inductances

$L_{T,i}$ [mH]		Unit 1	Unit 2
Case 1	HV	1395.0	2524.4
	LV	0.61 (1427.7)	31.0 (2555.8)
Case 2	HV	172.7	420.75
	LV	0.094 (221.5)	6.7 (554.8)
Case 3	HV	1020.8	1536.0
	LV	0.447 (1058.6)	19.0 (1566.5)
Case 4	HV	1392.7	2362.2
	LV	0.6 (1434.5)	29.0 (2391.0)
Case 5	HV	1030.0	1612.1
	LV	0.450 (1066.0)	19.8 (1632.4)

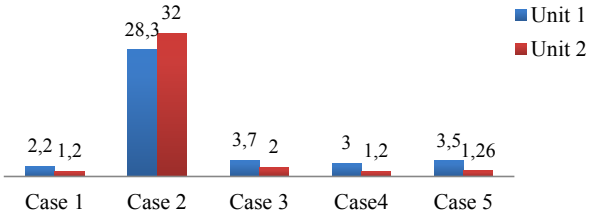

Figure 5.3 The relative difference (%) between the off-core inductances seen from HV and LV sides

To understand the relative differences, the flux distribution in each simulation case can be informative, as shown in Figure 5.4 for Unit 1. As can be seen, the flux return path in Case 2 mainly includes the channel beyond the winding excited parallel to the wall. This gap for LV (the inner) winding is wider than that for the HV (the outer) winding, and thus, the respective inductance is larger. For the remaining cases, the off-core inductance is mainly determined by the horizontal path from the core to the wall, less influenced by the path parallel to the wall. This flux path is not particularly dependent to the radial location and thickness of the excited winding. However, the winding height may have an impact on these flux paths. The HV and LV windings have approximately similar heights in both Unit 1 and Unit 2. Hence, it is expected that HV and LV side off-core inductances (adjusted by turns ratio) will be similar for the all cases except for Case 2. It is worth mentioning that the transformer windings are normally designed to have approximately identical magnetic heights in order to control the electromagnetic forces, particularly in large power transformers. Therefore, neglecting the height difference of the windings, the flux paths for Cases 1, 3, 4 and 5, and thus, the inductances, are roughly similar.

In order to further explore the sensitivity of the off-core inductances to radial location and thickness of the windings, simple 2D-FEM models of Unit 1 are simulated. The first model includes only LV winding, and the inductance is calculated for different variations where the winding is displaced radially by 100% towards the wall, as shown in Figure 5.5. The results for each simulation case are shown in Figure 5.6. As can be seen, all the cases except for Case 2 are almost independent of the winding radial displacement. Moreover, the inductance of Case 2 decreases with distance because the flux return path parallel to the wall becomes narrower.

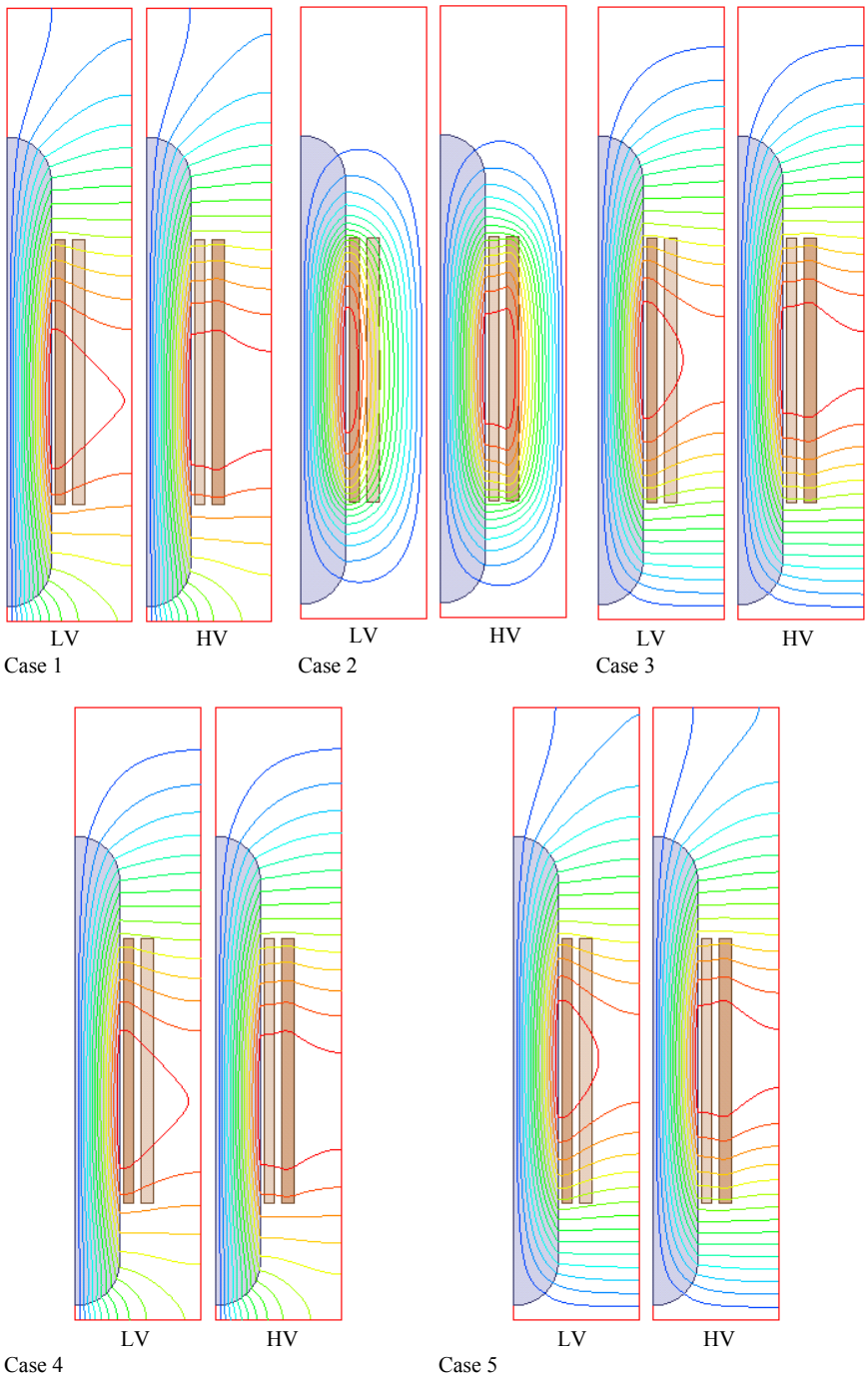

Figure 5.4 Flux lines for each simulation case and excitation side

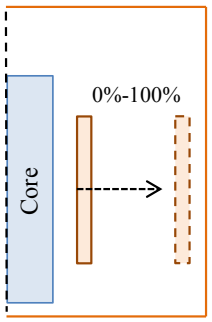

Figure 5.5 The FEM model for investigating radial displacement of the winding

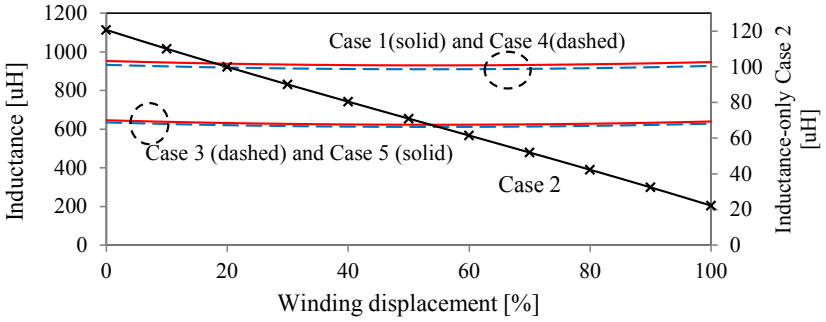

Figure 5.6 The results for radially displaced winding simulations (Figure 5.5)

The second model considers the influence of the winding thickness on the off-core inductance. Figure 5.7 shows the model where the thickness is increased by 200% from its original value. As can be seen in the results shown in Figure 5.8, the inductance except for Case 2 remains approximately constant in comparison to the thickness of the winding. The inductance for Case 2 has larger change versus the thickness. In fact, the flux return path parallel to the wall (and consequently, the off-core inductance) decreases with increasing thickness.

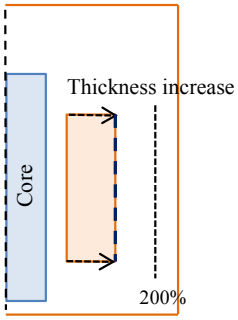

Figure 5.7 The model used for studying the winding thickness

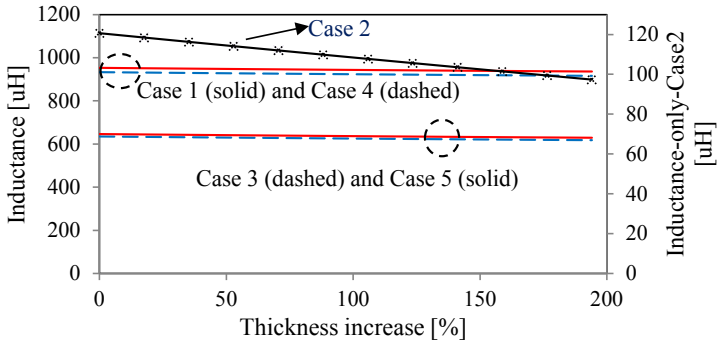

Figure 5.8 The off-core inductance versus winding thickness for each simulation case

5.1.5 Considerations on the off-core inductances - Case 2

As discussed, the off-core inductance for Case 2 seen from LV side is relatively larger than that seen from HV due to the wider off-core flux gap as seen in Figure 5.9. Here, the difference between these two off-core inductances is not equal to the leakage inductance as defined based on PS flux (denoted with L_{LH} in the overall equivalent circuit shown in Figure 3.2). This is basically because the leakage PS flux path is different from that of the off-core leakage paths in terms of path width and length.

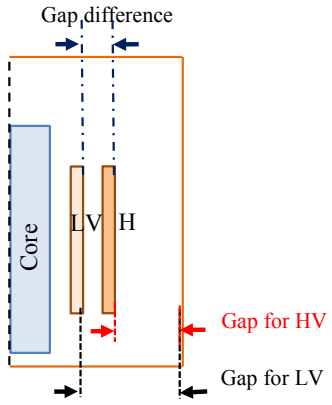

Figure 5.9 The flux paths for LV and HV sides in Case 2 and their geometrical difference

Considering the numerical results from Table 5.3, the inductance difference of Case 2 is 48.8 mH and 134.05 mH for Unit 1 and Unit 2, respectively. As explained above, it is smaller than the PS leakage inductances of 50 mH and 150 mH for Unit 1 and Unit 2, respectively. In the overall equivalent circuit shown in Figure 3.2, the off-core circuit is connected to the HV winding. This means that the $L^{LV}{}_{T,2}$ should be equal to $L^{HV}{}_{T,2} + L_{LH}$ but this is not the case according to the explanations given above. To correct this deviation, L_{LH} and $L^{HV}{}_{T,2}$ are magnetically coupled through a mutual inductance of M, as illustrated in Figure 5.10. This mutual inductance is calculated with (5.6) [105].

$$M=\frac{1}{2}(L_{LH}+L^{HV}{}_{T,2}-L^{LV}{}_{T,2}) \tag{5.6}$$

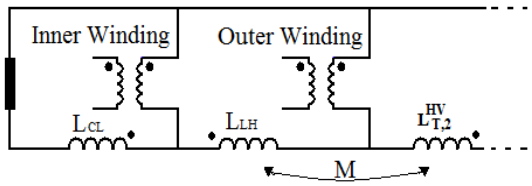

Figure 5.10 The off-core circuit improved for Case 2

5.1.6 Impact of the tank presence

5.1.6.1 Impact of the wall

The boundary conditions of flux-tangential and flux-normal as used for calculation of the off-core terminal inductances are two extreme states of the actual tank steel. As a matter of fact, the tank neither behaves as flux-tangential nor flux-normal boundary conditions. Using the model shown in Figure 5.5 with the cover and the bottom set to flux-tangential and the wall to impedance boundary conditions (in which the magnetic relative permeability and electric conductivity can be set), sensitivity of the inductance to the magnetic relative permeability and electric conductivity is studied. The winding location and the wall distance to the winding are considered to be the same as to LV winding of Unit 1. The results are shown in Figure 5.11, where the *x*-axis is the relative permeability in logarithmic scale varying from 1 to 50000. As can be seen, the wall with low electric conductivity and high magnetic permeability behaves as a flux-normal boundary condition. In contrast to this, the wall with high electric conductivity and low magnetic permeability behaves as a flux-tangential boundary condition. Examples of these two extreme states are the walls equipped with magnetic shunts and magnetic shields that are used to keep the flux away from the tank walls.

The magnetic shunts are constructed from laminated electric steel similar to the core material having high permeability and very low conductivity. Since these shunts are formed from laminated sheets in the flow direction of magnetic flux, the induced current is confined to each lamination and thus, it does not encompass the active part. It means that the tank walls equipped with shunts can be considered as flux-normal boundary condition. This can be seen in Figure 5.11, where the off-core inductance for the wall conductivity σ_7 (=0.1 kS/m that is as low as semi-conductive materials) reaches to that for the wall set to flux-normal boundary condition at magnetic relative permeability higher than ~100.

The magnetic shields are of good electric conductors with relative permeability of 1, which is normally copper. Despite of the magnetic shunts, the shield provides a closed path for the induced current and acts like a one-turn winding encompassing the active part. The opposite amp-turn induced in this one-turn conductor forces the flux confined between the shield and the winding excited. This is similar to the wall set to a flux-tangential boundary condition. This can be seen in Figure 5.11 where the off-core inductance for the wall conductivity σ_1 (=56 MS/m the same as of copper) reaches to that for the wall set to a flux-tangential boundary condition at magnetic relative permeability lower than ~1000 (which is applicable to the tank steels made of mild steels).

For electric conductivity ranged between σ_1 (as of copper) and σ_7 (as of semi-conductors), the wall behaves between two limits of flux-tangential and flux-normal boundary conditions. It should be noted that the tank steel is magnetically non-linear with magnetic permeability varying from low values at the initial and saturation regions to high values at the linear region of B-H characteristics. Therefore, the wall behavior oscillates between flux-normal and flux-tangential boundary conditions as ZS flux varies in a wide range.

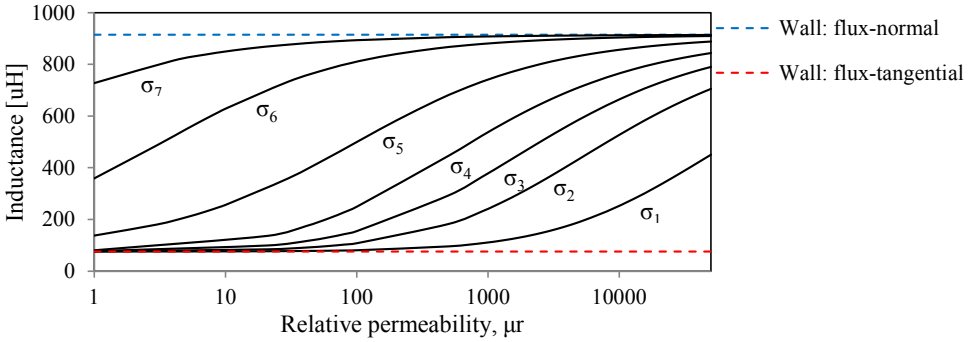

Figure 5.11 The off-core inductance (reference to model Figure 5.5 with the wall set to impedance boundary condition as well as the bottom and cover to flux-tangential boundary condition) versus the wall relative permeability at different wall electric conductivity ($\sigma_1>\sigma_2 \ldots>\sigma_7$)

Two important aspects must be pointed out with respect to the tank conductivity. The First concerns with the tank temperature rise caused by the heat generated in the windings and the core at normal operation of transformers as well as joule losses in the tank resulting from the current induced by the off-core flux. This current can be high in the case of large zero sequence flux leading to high temperature in the tank, and consequently to low electric conductivity.

Second note concerns with corrugations of the tank wall. As discussed in Section 4.1.7, the corrugation has an increasing effect on the wall resistance that can be considered in an equivalent conductivity denoted with σ^* (using equation (4.5)).

Table 5.4 and Table 5.5 provide a summary of the electric conductivity of the two steels of 4 mm and 1.25 mm thickness (introduced in Chapter 4) at three different temperatures; 20 ℃, 50℃ and 110 ℃. For the 1.25 mm thick sample, equivalent values are provided for the wall construction of Unit 1 designed with 44 fins of 120 mm height and circumference length of 2880 mm.

Using the values provided in Table 5.4 and Table 5.5, the off-core inductance is plotted versus the wall magnetic permeability, as shown in Figure 5.12. As can be seen, the inductance curve shifts slightly up (this applies for both plain and corrugated wall types) due to the temperature impact on the conductivity.

Table 5.4 Summary of electric conductivity for the 4 mm thick steel sample

Thickness	σ at 20℃ kS/m	σ at 50℃ kS/m	σ at 110℃ kS/m
4 mm	6410	5222	4044

Table 5.5 Summary of electric conductivity for the 1.25 mm thick steel sample

Thickness	σ at 20℃ kS/m	σ^* at 20℃ kS/m	σ^* at 50℃ kS/m	σ^* at 110℃ kS/m
1.25 mm	5820	1247	996	710

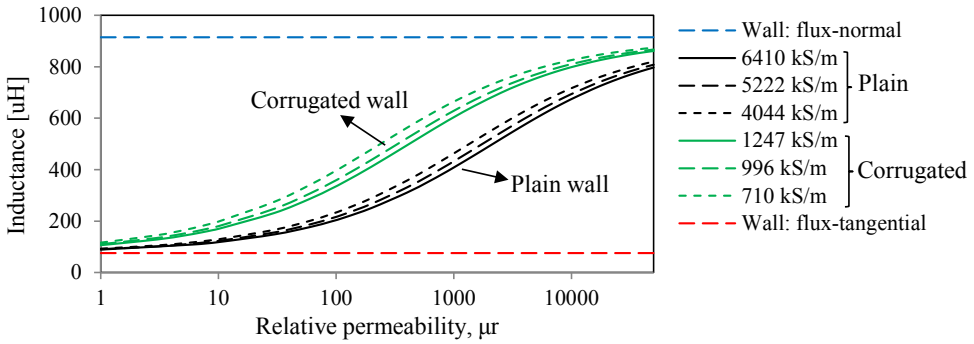

Figure 5.12 The off-core inductance (reference to model Figure 5.5 with the wall set to impedance boundary condition as well as the bottom and cover to flux-tangential boundary condition) versus relative permeability for the tank steel conductivity at different temperatures (reference to Table 5.4 and Table 5.5)

In order to investigate the effect of the Core-Wall distance, variations of the simulations are performed with different relative Core-Wall distance ($ratio_{cw}$) defined as *ds*/(*Core height-Winding height*); see Figure 5.13 Left. As can be seen in the results shown in Figure 5.13 Right (obtained for the conductivity 6410 kS/m as an example, similarly shaped curves are obtained for other conductivity), the off-core inductance curve is less dependent of permeability when the $ratio_{cw}$ increases. There are two distinguished sides in the curves, the high permeability side where the inductance is increasing with the $ratio_{cw}$ and the low permeability side where the inductance is decreasing with an increase in the $ratio_{cw}$. To understand this behavior, the off-core inductances of upper limit (the wall set to flux-normal boundary condition) and lower limit (the wall set to flux-tangential boundary condition) are plotted versus $ratio_{cw}$ as shown in Figure 5.14. As can be seen:

1. The wall boundary condition at larger $ratio_{cw}$ is less significant, since both curves converge at an ultimate inductance of 288.6 mH.
2. For the wall set to flux-normal boundary condition, the off-core inductance is higher than the convergent value and decreases with $ratio_{cw}$.
3. For the wall set to flux-tangential boundary condition, the off-core inductance is lower than the convergent value and increases with $ratio_{cw}$.

Based on the above results, the wall at higher permeability behaves similar to flux-normal boundary condition as the off-core inductance is decreasing with the $ratio_{cw}$ for both cases. There is a similar resemblance between the wall at lower permeability and flux-tangential boundary condition. As a result, the permeability of the wall corresponding to the convergent inductance can be assumed as a transition point from tangential-like (low permeability side) to normal-like (high permeability side) behavior.

Table 5.6 provides the transition permeability for the wall conductivity of both plain and corrugated types at temperatures 20℃ and 110℃, and at different $ratio_{cw}$. As can be seen, the transition permeability is smaller for the wall of low conductivity than that of high conductivity. In other words, the plain tank walls having higher conductivity can be assumed as flux-tangential boundary condition even at rather high magnetic permeability. In contrast to this, the walls of corrugated type with lower effective conductivity behave like a flux-normal boundary condition at low magnetic permeability (this occurs at much lower permeability when the wall temperature rises up to its typical values during the operations). In addition to the conductivity, the transition permeability decreases with $ratio_{cw}$. This can be explained by the fact that the circulating current induced in the wall is lower at farther walls, resulting in easier flux penetration. This means that the wall is more similar in nature to the flux-normal condition.

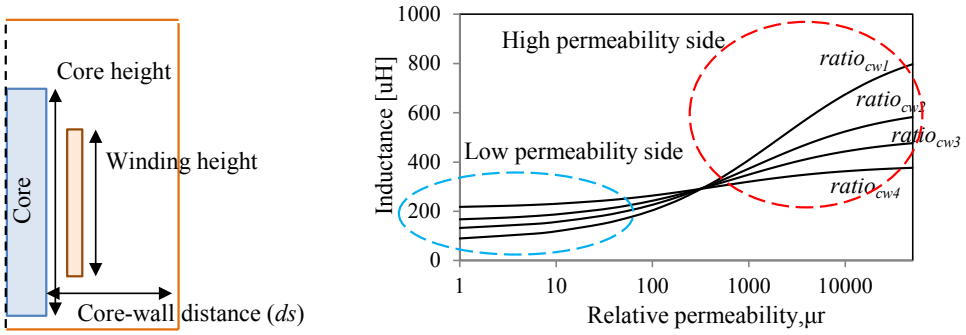

Figure 5.13 Left: definition of $ratio_{cw}$ defined as *ds/(Core height-Winding height)*, Right: the off-core inductance versus the wall permeability at different tank wideness ratios, $ratio_{cw1}<ratio_{cw2}<ratio_{cw3}<ratio_{cw4}$ (at a sample conductivity of 6410 kS/m)

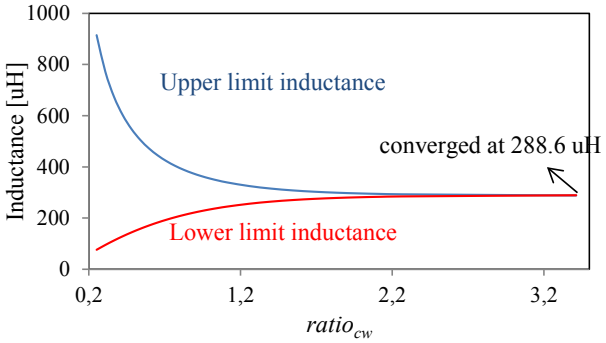

Figure 5.14 Upper (wall is set to flux-normal boundary condition) and lower (wall is set to flux-tangential boundary condition) limit inductances versus of $ratio_{tw}$ defined as *ds/(Core height-Winding height)*

Table 5.6 Transition relative permeability from tangential-like to normal-like wall

$\mu_{r\_transition}$	$ratio_{cw}$			
	0.3	0.4	0.5	0.8
σ = 6410 kS/m	325,4	316,6	311,2	305,2
σ = 4044 kS/m	198,5	192,8	189,3	185,5
σ* = 1247 kS/m	61,3	59,3	58,3	57,2
σ* = 710 kS/m	24,0	34,7	33,8	32,8

5.1.6.2 Impact of the tank cover

As discussed in Section 5.1.4, the cover does not affect the terminal off-core inductances of Unit 1, since the cover is far above the core top. However, in some designs the winding leads are taken out through the wall, thus resulting in a small distance between the core top and the cover.

In order to investigate the sensitivity of the off-core inductance to Core-Cover distance, variations of the pairs [Case 1, Case 4] and [Case 3, Case 5] with different distance ratios between Core-Core and Core-Wall are simulated. In each pair, only the cover has different boundary conditions (see Table 5.1). Figure 5.15 shows the model and results (as the off-core inductance) where the *x*-axis is the ratio as defined above. As can be seen, the inductances of pairs [Case 1, Case 4] and [Case 3, Case 5] are convergent at the ratio of 2.5 meaning that the cover becomes insignificant at ratios beyond this point. Repeating the simulations for Unit 2, the same ratio of 2.5 is obtained at the convergent point.

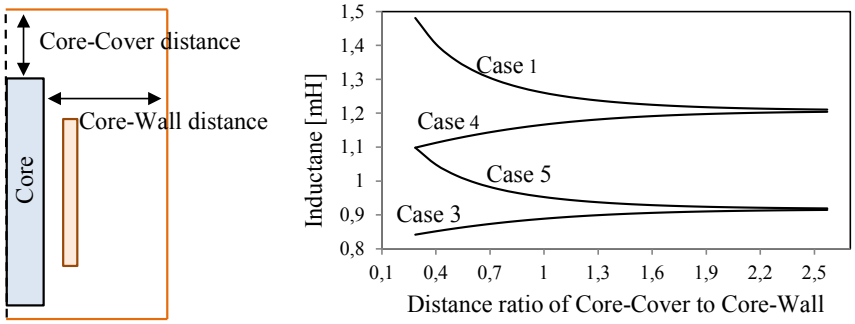

Figure 5.15 The off-core inductance at various Core-Cover relative gap

5.1.6.3 Impact of the tank bottom

To investigate the impact of the tank bottom, the wall is first set to the flux-normal and the bottom to the impedance boundary conditions. As can be seen in Figure 5.16, the bottom behaves between two extremes of flux-tangential and flux-normal conditions for relative magnetic permeability varying from 100 to 3000, which are more practical for structural steels. The wall is then considered to be more realistic by setting it to the impedance boundary condition. Variations of the model are simulated with different magnetic permeability and electric conductivity of the wall at two relative Core-Wall distances of

$ratio_{cw}$=0.3 and $ratio_{cw}$=0.8 (as defined in 5.1.6.1). As can be seen in the results shown in Figure 5.17, the bottom is less significant at lower wall magnetic permeability, higher wall conductivity, and smaller ratio, as defined above. In other words, when the wall behaves in a similar manner to a flux-tangential boundary condition, the bottom is not significant. This is the case for the corrugated walls and the walls with magnetic shunts. Conversely, the bottom is of higher impact when the wall conductivity is lower, the wall magnetic permeability is higher, and the ratio is larger. It can be realized that the walls behaving like a flux-normal boundary condition, which is the case for the plain walls and the walls with magnetic shields, mean that the bottom has a high impact.

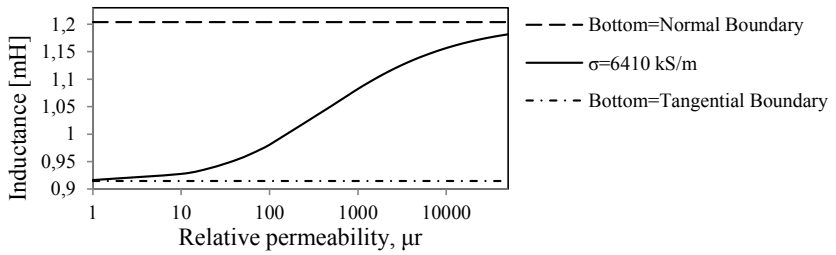

Figure 5.16 The off-core inductance as a function of relative permeability of the bottom at a sample conductivity of 6410 kS/m; the wall is set to normal boundary condition

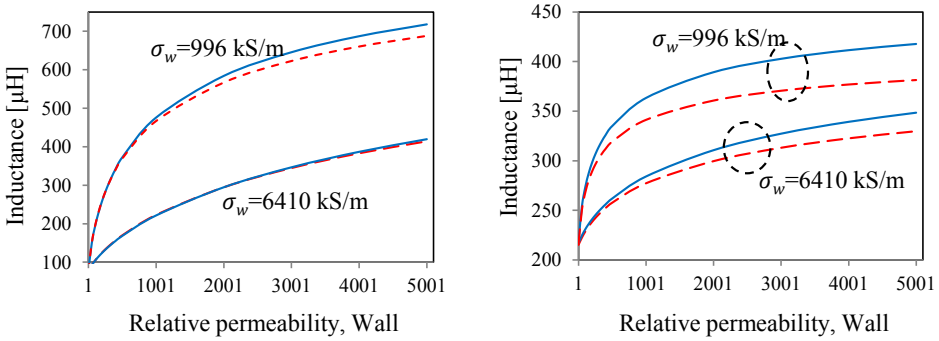

Figure 5.17 The off-core inductance as a function of the wall's relative permeability, σ_w is the wall conductivity, the bottom relative permeability is 200 (red-dashed trace) and 1000 (blue-solid trace), $ratio_{cw}$=0.3 (Left) and $ratio_{cw}$=0.8 (Right).

5.2 Parameters of the tank model

Considering the equivalent circuit for each tank element, a number of new parameters including wall heights (h_t), wall lengths (l_t), wall thickness (t_d) and electric conductivity (σ) of the tank steel are added to the existing parameter lists, the linear inductances.

It should be noted that the linear inductances calculated in Section 5.1 using flux-tangential and flux-normal boundary conditions instead of the actual tank walls need to be tuned when non-linear tank walls are involved. This is primarily due to the fact that the flux does not enter the wall through a single point. In Figure 5.18 illustrating a simplified flux

flow into the wall (in reality, the flux entrance points are continuously distributed), reluctance of each flux path towards the wall is denoted with R_i and the wall section between two flux-entering points by Z_i. When the wall has zero reluctance, the equivalent reluctance of the path towards the wall becomes parallel. However, when Z_i is not zero, the wall sections are also involved and an equivalent linear reluctance representing the paths towards the wall is no longer in parallel connection. In an equivalent circuit of such a complex structure, all the parameters including the wall height, thickness and conductivity as well as the linear inductances as calculated with extreme boundary conditions must be tuned by fitting the circuit to a given impedance and losses (resulting from FEA or tests) seen from the exited winding. The distribution of flux entering points depends on Core-Wall distance and electromagnetic properties of the wall steel. Core-Wall distance is a structural parameter dependent on the voltage level. However, the wall conductivity may vary during different operational conditions due to its temperature dependency. Therefore, once the tuning factors are obtained using the wall conductivity at a specific temperature, it must be checked to determine if it is still a valid tuning factor within a practical variation of temperature in the wall. A practical variation of the tank temperature can be assumed from 20℃ to 110℃ [84].

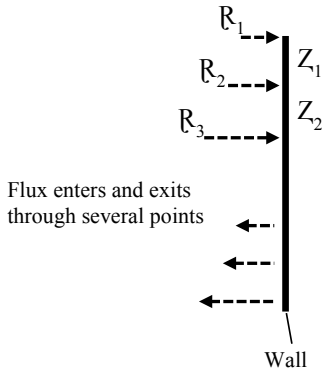

Figure 5.18 Flux enters and exits through several points

5.2.1 Considerations on the wall parameters

To investigate the capability of the off-core equivalent circuit as presented in Chapter 3 in reproducing the impedance and the losses, a simple 2D model as shown in Figure 5.19 is considered. The wall steel is modeled with the non-linear B-H curve as measured (the normal curve) for the 4 mm sample and electric conductivity of 6410 kS/m. The dimensions of the core and windings are the same as of Unit 1. The model is simulated by using 2D-FEM in transient formulation and the impedance and losses are calculated for verifying the equivalent circuit.

The equivalent circuit of this model is shown in Figure 5.20. Since the cover and bottom are set to a tangential boundary condition, the linear network can be reduced to only two linear inductances denoted with L_1 and L_2. Using the approach presented in Section 5.1.2, two linear inductances (seen from LV winding) are calculated for two variations with $ratio_{cw}$=0.3 (based on original dimension of Unit 1) and $ratio_{cw}$=0.4 (~60% wider than Unit 1) as shown in Table 5.7.

Table 5.7 Linear inductances for different variations of the model shown in Figure 5.19

Variations	$ratio_{cw}$	L_1	L_2
Based on Unit 1	0.3	75.9 µH	838.8 µH
~60% wider than Unit 1	0.4	188.0 µH	245.3 µH

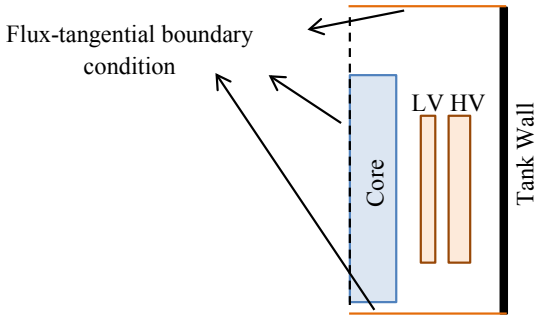

Figure 5.19 Simple 2D model including the wall as non-linear steel

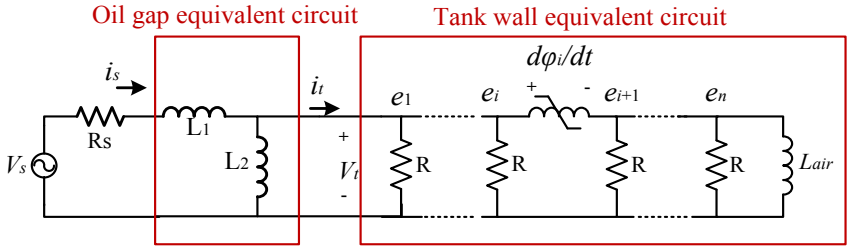

Figure 5.20 The off-core equivalent circuit of the model shown in Figure 5.19

The governing equations of this circuit are stated in (5.7) and (5.8).

$$V_t = V_s - R_s i_s - L_1 \frac{di_s}{dt} \tag{5.7}$$

where V_s, i_s and R_s are the voltage, current and resistance of the winding excited. V_s is the circuit input and the rest are outputs.

$$i_s = i_t + \frac{1}{L_2}\lambda_2 \rightarrow i_s = i_t + \frac{1}{L_2}\int V_t\, dt \tag{5.8}$$

where λ_2 is the flux linkage of L_2 and thus $\lambda_2 = \int V_t\, dt$ (see Figure 5.20).

Using the time derivative of (5.8), it follows:

$$\frac{di_s}{dt} = \frac{di_t}{dt} + \frac{1}{L_2}\frac{d\lambda_2}{dt} \rightarrow \frac{di_s}{dt} = \frac{di_t}{dt} + \frac{1}{L_2}V_t \tag{5.9}$$

The relation of V_t and i_t is described with the model presented in Chapter 3, Section 3.1.1.

An implementation of these equations together with the tank model in MATLAB-SIMULINK is shown in Figure 5.21.

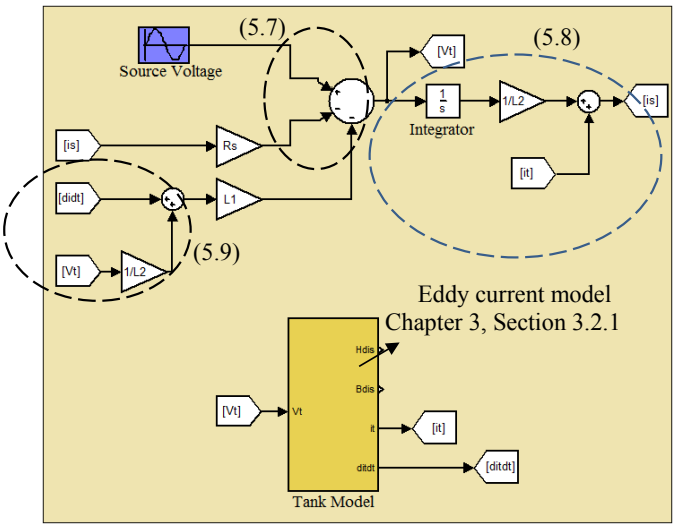

Figure 5.21 Implementing of the circuital equations of Figure 5.20 in MATLAB-SIMULINK

The results for Variation 1 are shown in Figure 5.22 and Figure 5.23 together with the results from the equivalent circuit. As can be seen, a specific wall height such as 0.57 m can be found at which both impedance and the losses calculated are fitted to the FEM results.

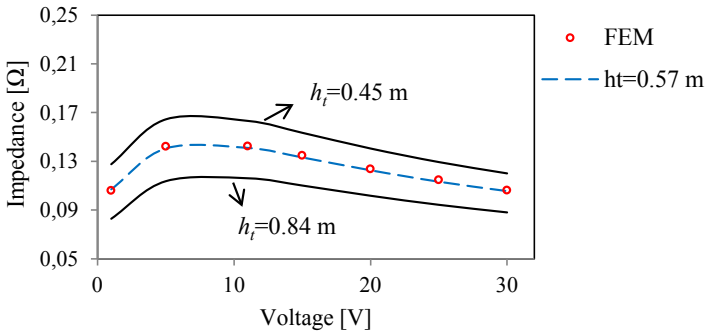

Figure 5.22 Impedance seen from LV side, $ratio_{cw}$=0.3, the wall conductivity: 6410 kS/m

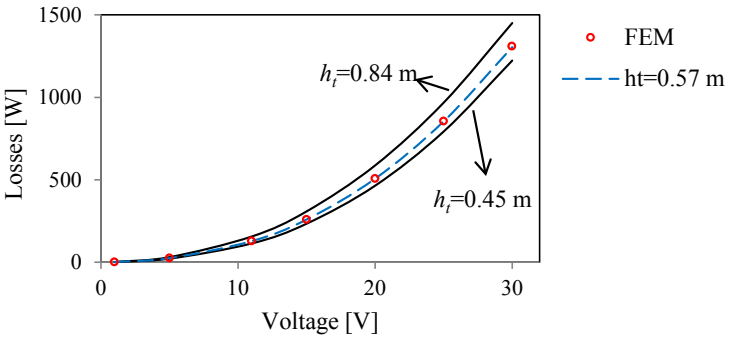

Figure 5.23 Losses seen from LV side, $ratio_{cw}$=0.3, the wall conductivity: 6410 kS/m

Using the same wall parameters, the FEM results can be reproduced for the wall conductivity reduced due to temperature rise up to 110℃ (see Table 5.4), as shown in Figure 5.24 and Figure 5.25.

Upon further reduction in the conductivity (that can be due to the corrugation), the circuit parameters will need to be tuned again. As examples, the conductivities of 996 kS/m and 710 kS/m (see Table 5.5) are chosen in the further simulations and the results are shown in Figure 5.26 and Figure 5.27. As can be seen, the wall height must change to 0.7 m and the inductance L_2 must increase by a factor of 1.15 in order to fit to the FEM results. Once the circuit is tuned for the wall conductivity of 996 kS/m, it will be valid for the conductivity of 710 kS/m.

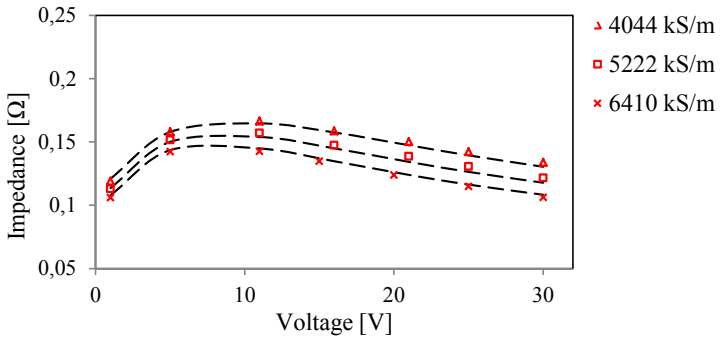

Figure 5.24 Impedance seen from LV side, $ratio_{cw}$=0.3, red markings: from FEM, dashed traces: from equivalent circuit results with h_t= 0.57 m at different wall conductivity

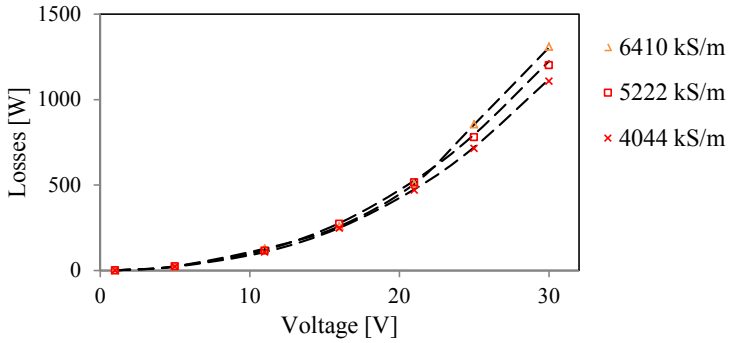

Figure 5.25 Losses seen from LV side, $ratio_{cw}$=0.3, red markings: from FEM, dashed traces: from equivalent circuit results with h_t= 0.57 m at different wall conductivity

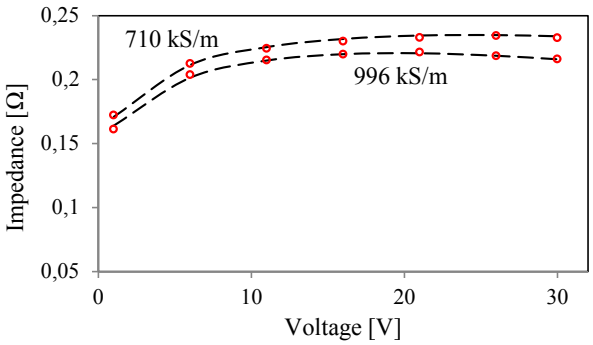

Figure 5.26 Impedance seen from LV side, $ratio_{cw}$=0.3, red markings: from FEM, dashed trace: from equivalent circuit results with h_t= 0.7 m and L_2 is increased by a factor of 1.15

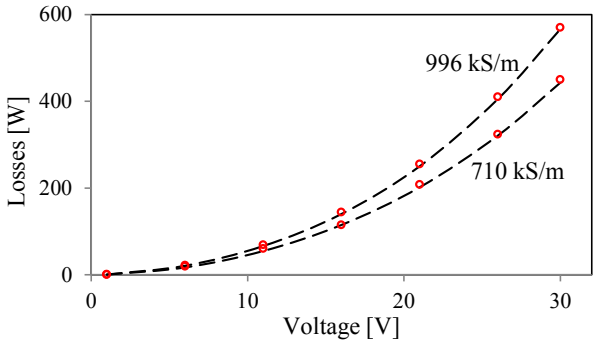

Figure 5.27 Losses seen from LV side, $ratio_{cw}$=0.3, red markings: from FEM, dashed trace: from equivalent circuit results with h_t= 0.7 m and L_2 is increased by a factor of 1.15

Figure 5.28 shows the impedance and the losses versus input voltage for the second variation (see Table 5.7) considering a wall conductivity of 6410 kS/m that illustrates a good fitting capability to the FEM results with $h_t = 0.65$ m and a factor of 1.15 for L_2.

Figure 5.29 shows a sensitivity analysis of the impedance and losses on the wall conductivity at voltage 30 V using the circuit with the parameters $h_t = 0.65$ m and the factor of 1.15 for L_2 as identified for the wall conductivity 6410 kS/m. As can be seen, both impedance and losses start slowly, deviating from the FEM results at a conductivity of around 4000 kS/m, which is below the conductivity variation range due to operational temperature rise of the tank (ranged from 6410 kS/m at 20℃ to 4044 kS/m at 110℃).

As a conclusion to this section, an off-core circuit tuned for conductivity at a given temperature will still be valid for higher temperatures (in a practical range for the transformer tank) and there is no need for re-tuning.

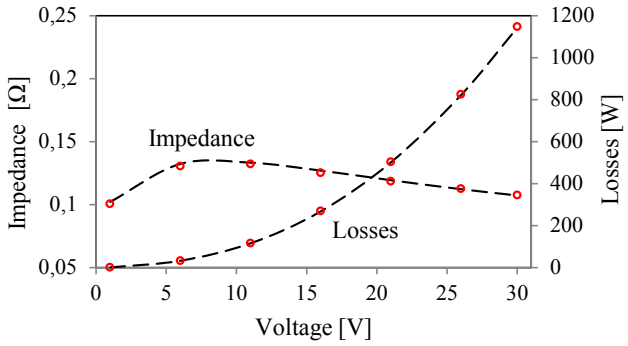

Figure 5.28 The impedance and losses (LV side) at wall conductivity of 6410 kS/m, wider variation, red markings: from FEM, dashed trace: from equivalent circuit results with h_t=0.65 m and L_2 increased by a factor of 1.15

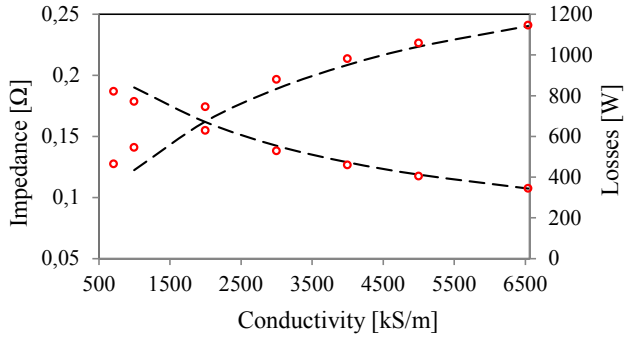

Figure 5.29 The impedance and losses (LV side) as function of wall conductivity, wider variation at voltage 30 V, red markings: from FEM, black-dashed trace: from equivalent circuit results with h_t = 0.65 m and L_2 increased by a factor of 1.15

Tuning factors of the wall height (h_t) and the inductance (L_2) are denoted with K_H and K_L, respectively. The K_H and K_L are defined as factors of, respectively, mechanical height of the wall (which is 1085 mm for the simulated model) and the inductance L_2 (calculated with the approach stated in Section 5.1.2). Table 5.8 summarizes these factors identified for different variations of the model shown in Figure 5.18.

Table 5.8 Tuning factors of the circuit parameters of the model shown in Figure 5.19

Model	Conductivity	K_H	K_L
$ratio_{cw}$=0.3	6410 kS/m	0.53	1.00
	996 kS/m	0.65	1.15
	710 kS/m	0.65	1.15
$ratio_{cw}$=0.4	6410 kS/m	0.60	1.15

5.2.2 Considerations on the bottom parameters

As illustrated in Section 5.1.6.3, the bottom behaves between two extreme states of flux-tangential and flux-normal boundary conditions. This influence is further studied with a simple 2D model, which includes the bottom with 4 mm thickness, as shown in Figure 5.30. The B-H curve of the bottom is that of the 4 mm sample presented in Chapter 4. The

impedance and losses seen from LV winding are calculated for two variations with different $ratio_{cw}$. The conductivity of the bottom and the wall are considered 6410 kS/m (as a plain plate at 20℃) and 996 kS/m (as a corrugated wall at 50℃), respectively.

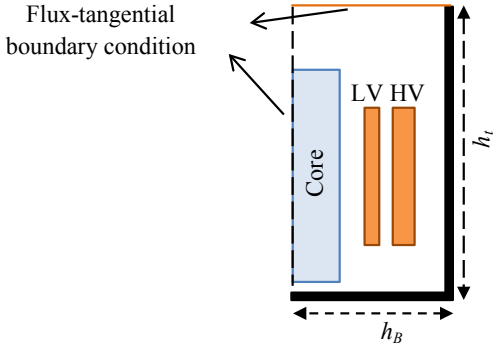

Figure 5.30 The simple 2D model including the bottom

Once the terminal off-core inductances for the model variations of Figure 5.30 (seen from LV winding) are calculated (see Table 5.9) the linear inductances of the off-core equivalent circuit are obtained (using the approach presented in Section 5.1.2) as listed in Table 5.10.

Since the cover is set to flux-tangential boundary condition, L_4 is bypassed in the overall equivalent circuit and only L_2 remains, which connects in parallel to the wall, as illustrated in Figure 5.31 (an implementation of this circuit in MATLAB-SIMULINK is presented in Appendix 2).

Table 5.9 Off-core inductances seen from LV side of the model in Figure 5.32

$L_{T,i}$ [μH]	Variation 1 $ratio_{cw}$=0.3	Variation 2 $ratio_{cw}$ =0.8
Case 1	1213.7	740.4
Case 2	75.9	211.9
Case 3	914.7	404.7
Case 4	1204.0	659.3
Case 5	919.5	418.3

Table 5.10 Linear inductances of the off-core equivalent circuit

Linear inductances [μH]	Variation 1 $ratio_{cw}$=0.3	Variation 2 $ratio_{cw}$ =0.8
L1	75.9	211.9
L2	2238.1	882.9
L3	1342.6	246.6
L4	34.5	383.5
L5	933.01	660.4

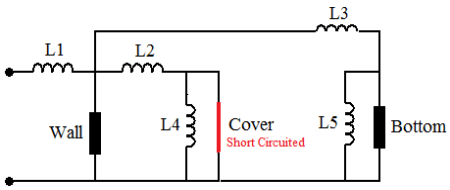

Figure 5.31 Equivalent circuit of the model shown in Figure 5.30, the cover is short-circuited due to the tangential boundary condition

Figure 5.32 and Figure 5.33 show the impedance and the losses calculated where the red markings show the results of FEM simulations and the blue dashed traces are from the equivalent circuit (Figure 5.31). In order to consider the multiple flux entrance points to the wall and bottom and fit the equivalent circuit to the results from FEM simulations, the tuning factors of the height (K_H), the linear inductance (K_L) and the conductivity (K_S) are found, as given in Table 5.11. The K_S is defined as a proportional factor of the actual conductivity of the wall/bottom. Both the wall and the bottom have the same factors of K_S and K_H, while all the linear inductances have the same factor of K_L.

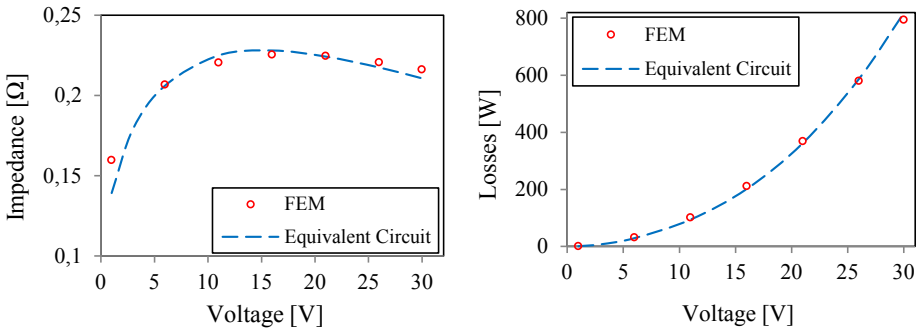

Figure 5.32 The off-core impedance (Left) and losses (Right) as a function of voltage, the model of Figure 5.30 - Variation 1 (see Table 5.9)

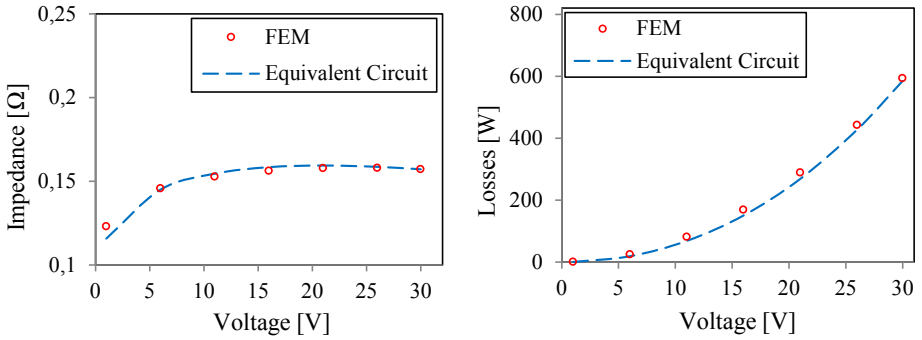

Figure 5.33 The off-core impedance (Left) and losses (Right) as a function of voltage, the model of Figure 5.30 - Variation 2 (see Table 5.9)

Table 5.11 The tuning factors of the equivalent circuit parameters

Model	K_S	K_H	K_L
Variation 1 ($ratio_{cw}$=0.3)	1	0.78	1.6
Variation 2 ($ratio_{cw}$=0.8)	0.55	1.3	2.3

To compare the results, the impedance and the losses of the models shown in Figure 5.19 (only the wall considered) and Figure 5.30 (the bottom also included) are plotted in Figure 5.34 through Figure 5.37. As can be seen, the bottom's presence leads to an increase in the losses in both variations. The off-core impedance is less sensitive to the bottom's presence at smaller $ratio_{cw}$ where the wall is dominant. However, the bottom has a stronger influence when $ratio_{cw}$ increases and the wall behaves more as flux-normal than flux-tangential boundary condition. These observations are expected as discussed in Section 5.1.6.3.

The tank bottom is a base plate of transformers and is normally much thicker than the walls. The impact of the bottom thickness is also seen in the simulation results where the bottom is considered with a thickness of 10 mm. The bottom thickness generally has an increasing impact on the losses and a decreasing impact on the off-core impedance. The impact on the losses is not considerable at high wall conductivity (which is similar to the flux-tangential condition) and small $ratio_{cw}$. On the contrary, the impact on the off-core impedance is observable at low wall conductivity (which is similar to the flux-normal condition) and large $ratio_{cw}$.

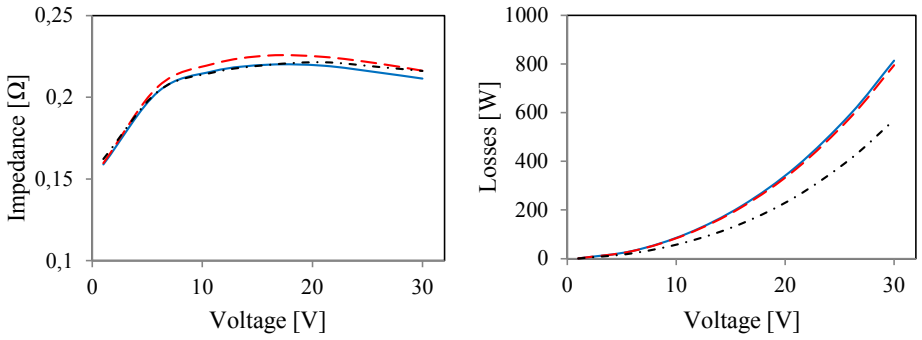

Figure 5.34 The tank bottom's influence on the off-core impedance and the losses for Variation 1, electric conductivity of 996 kS/m for Wall and 6410 kS/m for Bottom, dashed trace: Bottom thickness is 4 mm, solid trace: Bottom thickness is 10 mm, dotted-dashed trace: no Bottom

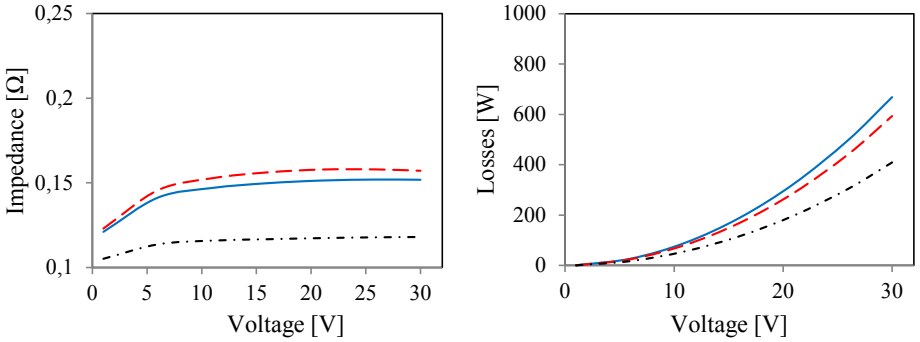

Figure 5.35 The tank bottom's influence on the off-core impedance and losses for Variation 2, electric conductivity of 996 kS/m for Wall and 6410 kS/m for Bottom, dashed trace: Bottom thickness 4 mm, solid trace: Bottom thickness 10 mm, dotted-dashed trace: no Bottom

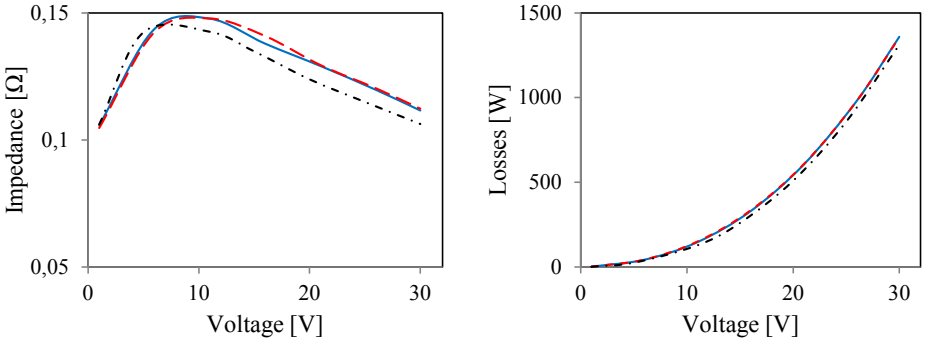

Figure 5.36 The tank bottom's influence on the off-core impedance and losses for Variation 1, electric conductivity of 6410 kS/m for both Wall and Bottom, dashed trace: Bottom thickness 4 mm, solid trace: Bottom thickness 10 mm, dotted-dashed trace: no Bottom

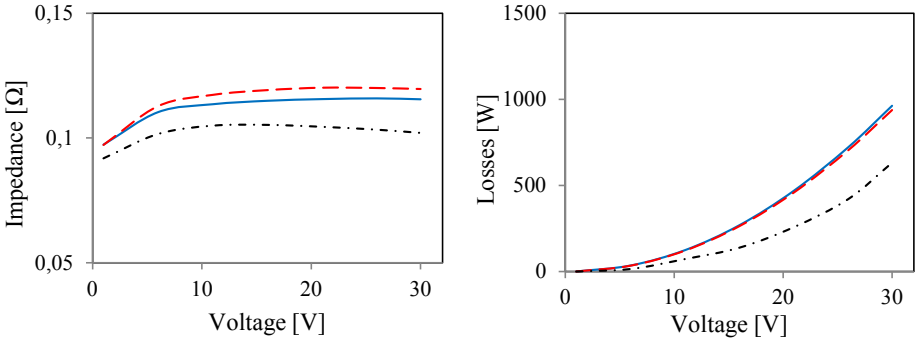

Figure 5.37 The tank bottom influence on the off-core impedance and losses for Variation 2, electric conductivity of 6410 kS/m for both Wall and Bottom, dashed trace: Bottom thickness 4 mm, solid trace: Bottom thickness 10 mm, dotted-dashed trace: no Bottom

5.2.3 Temperature impact

As discussed, the parameters identified for the off-core path model can be considered temperature independent. Hence, the thermal model of the tank wall (presented in Chapter 3, Section 3.2) can be coupled to the circuit of Figure 5.31 (implemented in MATLAB-SIMULINK as presented in Appendix 2, using tuning factors given in Table 5.11 for variation 1, $ratio_{cw}$=0.3) in order to investigate the impact of the tank temperature rise on the impedances and losses. It is assumed that the wall is of plain type (not corrugated) and the electric conductivity at 20 °C is 6410 km/S. Both heat transfer mechanisms of convection and radiation (with emissivity=0.95) from the wall are taken into account where temperature dependency of the thermal parameters is considered as well. The convection coefficients of the air and the transformer oil as well as equivalent radiation coefficient from the outer surface of the wall are shown in Figure 5.38. These coefficients are calculated at ambient temperature of 20 °C and oil average temperature of 55 °C with the equations stated in Appendix 1.

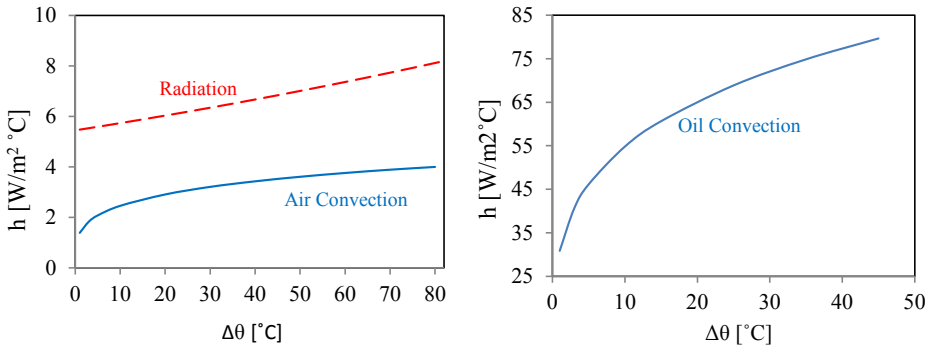

Figure 5.38 Hear transfer coefficient of Left: Ambient air convection coefficient (solid curve), Radiation from Wall outer surface (dashed curve) Right: Transformer oil convection coefficient

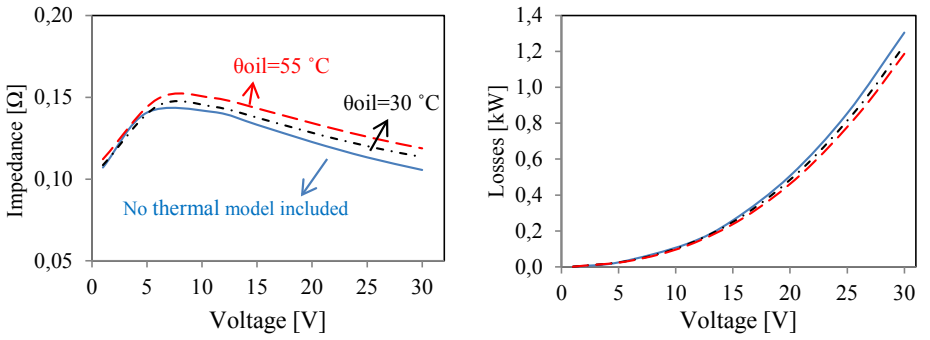

Figure 5.39 The off-core impedance and losses of the model Figure 5.19, $ratio_{cw}$=0.3 taking the thermal model into calculation, solid trace: no thermal model included, dashed trace: Oil temperature is 55 °C, dotted-dashed: Oil temperature is 30 °C

Figure 5.39 shows the simulation results in terms of impedance and losses seen from the LV winding at steady state condition and at two different oil temperatures of 30 °C and 55 °C. As can be seen, the impedance is increasing with the oil temperature. The rate of increase is higher at higher voltages, since the temperature rise in the wall is higher due to the relatively higher losses. However, the increase in resistance due to temperature rise causes a decrease in the wall losses compared to the case where no-thermal model is used.

Figure 5.40 shows dynamic response of the wall temperature at the input voltage of 30 V. It takes about 11.4 and 10.5 minutes to reach the wall steady state temperature (99%) at input oil temperatures of 30 °C and 55 °C, respectively. Since the thermal resistances are non-linear, the thermal time constant is thus temperature dependent.

Considering the wall with the conductivity of 996 kS/m (resembling the corrugated walls), the impedance and losses are those shown in Figure 5.41. The length of the wall considered for calculation of heat transfer from the outer surface is corrected with a factor of 6410(kS/m)/996(kS/m) in order to take the surplus surface due to the corrugation into account. As can be seen, the impedance becomes flatter at higher voltages and the losses decrease faster than of the plain wall due to the temperature rise.

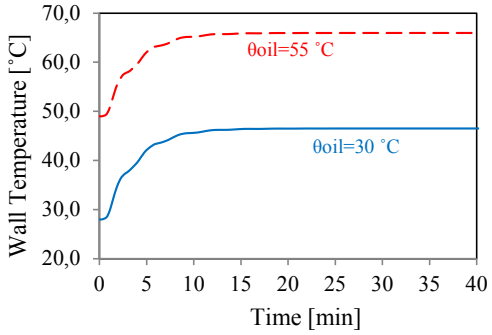

Figure 5.40 Dynamic response of Wall temperature at Voltage of 30 V and Oil temperature of 55 °C (dashed trace) and 30 °C (solid trace)

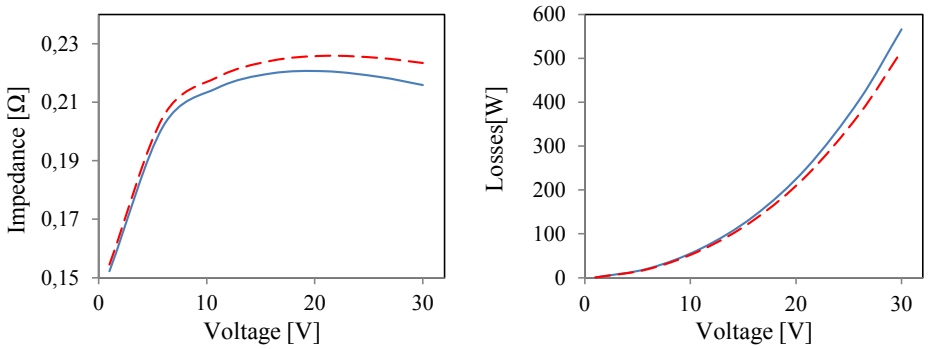

Figure 5.41 The off-core impedance and losses for the model Figure 5.19, $ratio_{cw}$=0.3 with Wall conductivity of 996 kS/m, solid trace: no thermal model included, dashed trace: thermal model included with Oil and Air temperature of 55 °C and 20 °C, respectively

5.3 Winding radial position: impact on the off-core inductance

As shown in Figure 5.6, the off-core inductance for the cases where the wall is set to a flux-normal boundary condition does not change to any great extent with radial displacement of the winding. On the contrary, the inductance is sensitive to the radial displacement when the wall is set to a flux-tangential boundary condition. To investigate this sensitivity for realistic tank walls, the model of Figure 5.5 is simulated again wherein the wall is set to the impedance boundary condition. The simulations are performed with the wall relative permeability of 20 and 1000 and the conductivity of 996 kS/m and 6410 kS/m.

The inductance of the displaced winding normalized to the inductance at the original position (0%) as a function of radial relative displacement is shown in Figure 5.42. As can be seen, it is more sensitive to the radial displacement at lower permeability and higher conductivity. It could be expected since the wall with low permeability and high conductivity resembles the flux-tangential boundary condition.

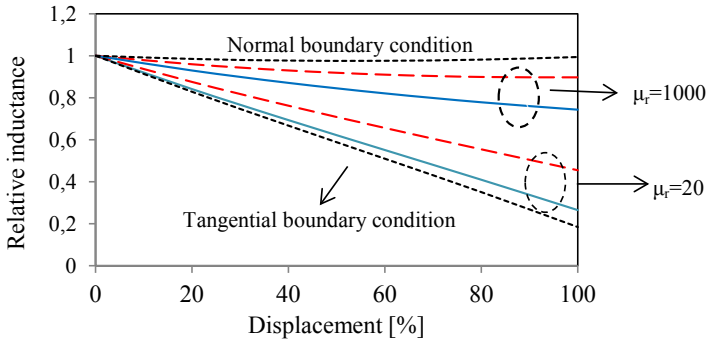

Figure 5.42 Relative inductance of the displaced winding based on inductance at $dx = 0$, for the wall conductivity of 996 kS/m (dashed trace) and 6410 kS/m (solid trace)

It can be interpreted that the rate of change of the off-core inductance versus radial displacement is larger for the plain walls (and the walls equipped with magnetic shield) than for the corrugated walls (and the walls equipped with magnetic shunts).

Based on the above explanation, it can be expected that the difference between HV and LV side off-core inductances (assuming that both have equal magnetic heights) is larger at lower excitations where the magnetic permeability is lower. This difference becomes smaller when the excitation increases because the magnetic working point moves towards the linear part of the B-H characteristics leading to higher permeability. It is worth mentioning that, the resistivity increase, due to the temperature rise at higher excitations, will also affect the off-core inductance difference.

Radial displacement can also influence the transition permeability, which is a turning point where the tank behavior changes from being as flux-tangential to flux-normal boundary conditions (see Section 5.1.6.1). As can be seen in Figure 5.43, the converged inductance for the same model as used in Section 5.1.6.1 where the excited winding is radially displaced by

50% towards the wall becomes 254.0 uH, which is ~12% smaller than the case of no-displaced winding (288.6 uH). In fact, shifting the winding towards the wall will not influence the upper limit inductance, as shown in Figure 5.6 (Case 3), but has a decreasing impact on the lower limit inductance due to narrower gap between the excited winding and the wall. Hence, two graphs will meet at lower inductance and larger $ratio_{cw}$.

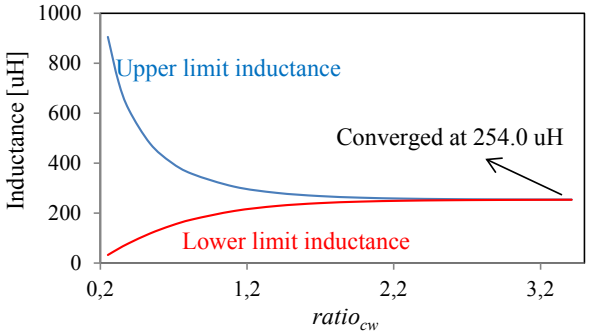

Figure 5.43 Upper (wall is set to flux-normal boundary condition) and lower (wall is set to flux-tangential boundary condition) limit inductances versus of $ratio_{cw}$ defined as *ds*/(*Core height-Winding height*) for the case where the excited winding is radially shifted by 50% towards the wall

Chapter 6

Benchmarking of the off-core model of Unit 1

6.1 OC-ZS characteristics

In order to verify the off-core model in representing actual transformers, the open circuit zero sequence impedance measured from HV and LV side of Unit 1 is used. First, lossless variations of the off-core model are considered where the tank branches are excluded and replaced with flux-normal and flux-tangential boundary conditions. These variations are introduced as simulations cases 1 through 5 in Table 5.1.

With the lossless variations, the following questions are answered:

1. Which of the simulation cases introduced in Table 5.1 is the most proper approximation for representing the actual off-core path of transformers?
2. Which tank elements are significant and must be considered in the complete model?

6.1.1 Lossless variations

Considering simulation cases of Table 5.1 as varieties of lossless models, the off-core inductances calculated for each are compared with the measurements from LV as well as HV sides of Unit 1. Figure 6.1 shows OC-ZS inductance measured from LV side versus phase voltage compared to the inductances obtained for each simulation case. As can be seen:

1. the inductance is much larger than that of Case 2 meaning that the tank does not behave as flux-tangential boundary condition at all.

2. the inductance is slightly lower than those of Case 3 and Case 5 at voltages lower than 1.8 V (that is ~1.4%); however, it becomes larger at voltages beyond that.
3. at higher voltages, the inductance tends to be almost constant with a small decreasing rate.

Since the tank wall of Unit 1 is of the corrugated type, the effective resistivity of the wall is much higher, as explained in Section 5.1.6.1. Accordingly, the transition permeability is expected to be low as it is less than 60 (see Table 5.6) for the corrugated wall at temperature 20℃. It is even lower for higher temperatures. This means that the wall resemblance to the flux-normal boundary condition takes place at a lower voltage (as low as 1.3%). However, at very low voltages, the flux density in the wall is too small, shifting the wall magnetic working point to the initial region of the B-H characteristics. Hence, the tank steel shifts to the low permeability region (see Figure 5.13) where the wall is similar to the flux-tangential boundary condition, and the inductance becomes closer to that of Case 2. At higher voltages, additional influence of the temperature rise on the conductivity can reduce the induced current leading to easier penetration of the flux. Hence, the wall influence approaches the flux-normal condition. This may also explain almost constant inductance where the wall is magnetically saturated but the off-core inductance is not decreasing as expected.

Similar observations can be made for the measurements from HV side as compared to the inductances of the lossless models shown in Figure 6.2. As can be seen, the measured inductance crosses the lines of Case 3 and Case 5 at the voltage 1.5% (about 100 V) that is approximately similar to that measured from LV side.

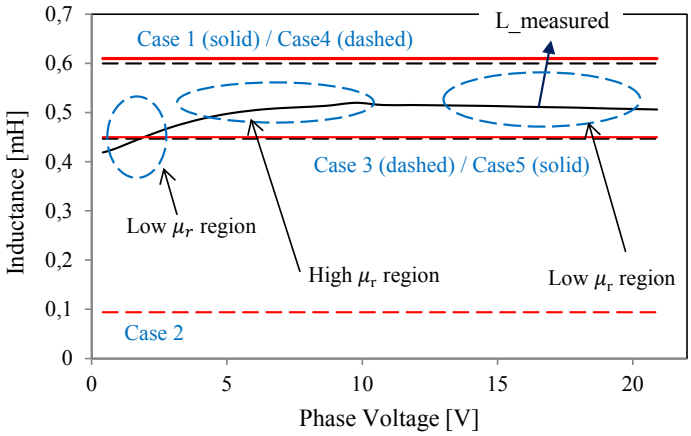

Figure 6.1 Off-core inductances of the lossless models in comparison to the OC-ZS inductance measured at the LV-side of Unit 1

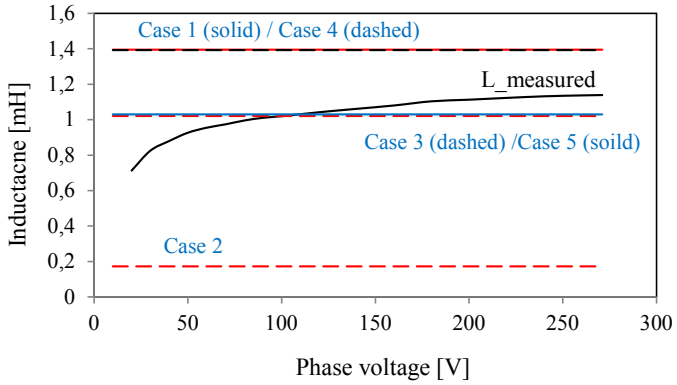

Figure 6.2 Off-core inductances of the lossless models in comparison to the OC-ZS inductance measured at the HV-side of Unit 1

6.1.2 The complete model

The complete model also includes the tank branches. As concluded in Section 6.1.1 the wall and the bottom of Unit 1 must be taken into account.

Linear inductances are calculated with the approach presented in Sections 5.1.1 and 5.1.2 as shown in Table 6.1. Since Core-Cover distance is sufficiently large to not influence the off-core impedance and losses (resulted in a small L_4), it is excluded from the modeling.

Table 6.1 Linear inductances of the off-core path for Unit 1

Inductance	Seen from LV [mH]	Seen from HV [mH]
L_1	0.0935	172.7
L_2	1.53	2016.3
L_3	0.4625	1463.3
L_4	1.00E-05	49.8
L_5	0.0303	1594.2

Table 6.2 summarizes physical and structural data to be used in the model identification. The thickness (t_d), number (n_f), fin spacing (S) and height of fins (H_f), the wall height (h_t) and circumference (l_C) are simply obtained from the tank dimensions. The effective length of the wall (l_{eff}) is calculated with $2n_f h_f + l_C$ (as clarified in 4.1.7).

The flux path in the bottom is denoted with h_B (see Figure 5.30) and is calculated with (6.1) as the dimensions are illustrated in Figure 6.3. This figure also shows the average path for the current induced (l_B) in the bottom. The length of the current path is calculated with (6.2) where the path at both short ends is approximated by half circles with a radius of $\frac{1}{2}\left(\frac{B_W+B_S}{2}\right)$.

$$h_B = \frac{6B_W+2B_S}{8} \tag{6.1}$$

$$l_B = 4B_{L-L} + \frac{\pi(B_W+B_S)}{4} \tag{6.2}$$

where B_{L-L} is the leg-leg distance, B_S and B_W are the distance of the outer leg to the tank short side and long side, respectively.

The OC-ZS impedance and the losses measured from LV and HV side will be used for verifying of the model.

Table 6.2 Physical and structural data of Unit 1 to be used in the modeling of off-core flux path

	Thickness	Fins	Height	Length	Conductivity
Wall	t_d=1.25 mm	n_f=44 H_f=120 mm S=60 mm	h_t=1085 mm	l_c=2880 mm l_{eff}=13440 mm	σ_{20}= 5820 kS/m α_{20}=0.0084 °C^{-1}
Bottom	t_B=4 mm	NA	h_B=190.6 mm	l_B =1484.7 mm	σ_{20}= 6410 kS/m α_{20}=0.0065 °C^{-1}

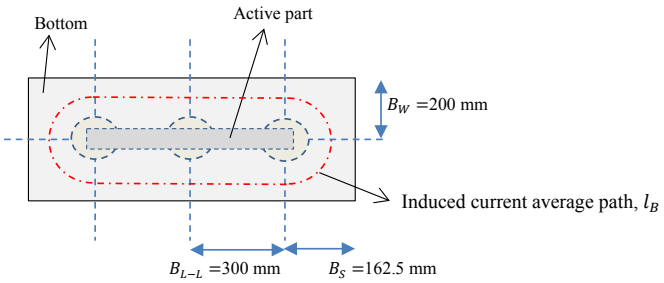

Figure 6.3 An illustration of bottom dimension and average path of the induced current

The following considerations are made in the simulations:

1. Since the wall of Unit 1 is of corrugated type, the equivalent conductivity σ^* taking account the corrugation length is 1247 kS/m at 20 °C using (4.5).
2. The ambient air temperature is set to 20 °C.
3. The top and bottom oil temperature is assumed to be 20 °C (the same as the ambient) because the transformer had not been loaded before the tests. Since the oil heat capacity is large, any temperature rise in the oil due to the heat generated in the wall is neglected.
4. Separate thermal models are used for the wall (corrugated vertical wall) and the bottom (Horizontal plate). As stated in Section 3.2.2, the characteristic length of the wall and the bottom are 1085 mm (the wall height) and 139.6 mm (Area/Perimeter), respectively. Figure 6.4 shows an illustration of the wall and the bottom stating which heat transfer mechanism is used for the surfaces.
5. The wall area at the corners is considered as plain plate and both convection and radiation of plain vertical wall are used for them. The total length of this area is

calculated with $(l_c - (n_f - 4)S)$ where $(n_f - 4)S$ is the total length of the wall under the fins. Using the dimensions in Table 6.2, the length of areas under the fins and the corners become 2400 mm and 250 mm, respectively.

6. Figure 6.5 and Figure 6.6 show the heat transfer coefficients of the tank surfaces using the equations stated in Table 6.3.
7. The physical parameters of the air and the oil are described in Appendix 1.
8. The equivalent circuit of Figure 5.33 is used for the simulations. As concluded in Chapter 4, Section 4.1.4, the excess losses of the 1.25 mm sample are considerable, and this is thus taken into account in the simulations. However, the bottom is of 4 mm steel and the excess losses are neglected. The excess losses coefficient for the 1.25 mm steel, denoted with g_B, is field dependent as described in Table 4.2.
9. Implementation of the circuit in MATLAB-Simulink is presented in Appendix 2.
10. Thermal capacitances are calculated with $\rho_{st} c_{p,st} V_{st}$ where ρ_{st}, $c_{p,st}$ and V_{st} are, respectively, the steel density, the specific heat capacitance and the volume. For the tank of Unit 1, ρ_{st}=7111 kg/m^3, $c_{p,st}$=490 Ws/kg°C and Vol_{st}=0.0172 m^3 for the wall and 0.0015 m^3 for the bottom. The volumes are calculated using the dimensions given in Table 6.2.

Using the tuning factors stated in Table 6.4, which are obtained by trial and error, the model fits to the measurements at the steady state, as shown in Figure 6.7. Figure 6.8 shows the wall and the bottom temperatures. As can be seen, thermal time constant of the wall is much lower than that of the bottom because of easier heat transfer from the wall rather than the bottom. This is important, because the duration of the geomagnetic disturbances with high magnitudes of GIC is in the range of minutes (some references mention to 5 minutes [16]), which is comparable with the thermal time constant calculated for the tank wall of Unit 1. This means that the wall will respond to such events quickly, despite of the discussions in the literature [15] [17]. With the average oil temperature of 55℃ (to be used for the wall inner ambient) and bottom oil temperature of 40℃ (to be used for the bottom inner ambient) resembling the full load condition, the OC-ZS impedance and the losses will become those as shown in Figure 6.9. As can be seen, the difference is not considerable for this transformer. The reason is the good heat transfer capability of the wall (see Figure 6.5 and Figure 6.6) that prevents the temperature rise to a high extent. For large power transformers where the radiators are located outside, the walls have poorer heat transfer capability rather than corrugated walls that results in a relatively higher temperature rise in the wall.

Using the linear inductances for the HV side given in Table 6.1, a new set of tuning factors is obtained (see Table 6.4) to fit the simulations results to the measurements from HV side, as shown in Figure 6.10. As a matter of fact, the winding distance to the wall influences the flux entering/exiting points to/from the wall and concentration of the flux lines at the wall inner surface, resulting in different tuning factors.

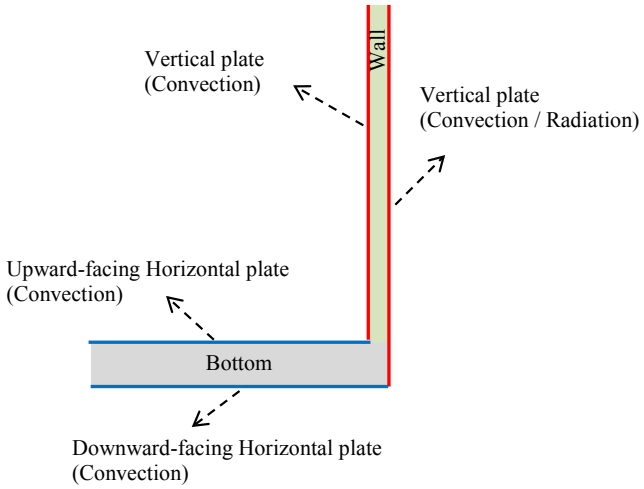

Figure 6.4 Heat transfer of each surface of the wall and the bottom

Table 6.3 Heat transfer equations used for different surfaces of the tank

Tank Surface	Heat transfer mechanism	Equation	Parameters
Wall (inner surface)	Convection-Vertical	(3.21)	L_c = 1085 mm
Wall (outer surface)	Convection Plain vertical (at the edges) Corrugated vertical (under the fins)	(3.21) (3.22)	L_c =1085 mm $\bar{L}_s = \frac{L_c}{S}$ =18.1 $\bar{H}_s = \frac{H_f}{S}$ =2
	Radiation Plain vertical (at the edges) Corrugated vertical (under the fins)	(3.27) (3.30)	$\bar{L}_s = \frac{L_c}{S}$ =18.1 $\bar{H}_s = \frac{H_f}{S}$ =2
Bottom (inner surface)	Convection Upward-facing	(3.23)	(Area/Perimeter) L_c =139.6 mm
Bottom (outer surface)	Convection Downward-facing	(3.24)	(Area/Perimeter) L_c =139.6 mm

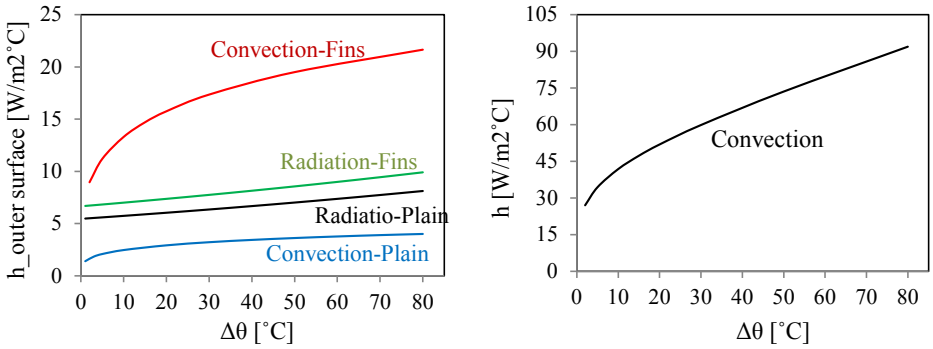

Figure 6.5 Heat transfer coefficients of the wall, Left: Outer surface, Right: Inner surface

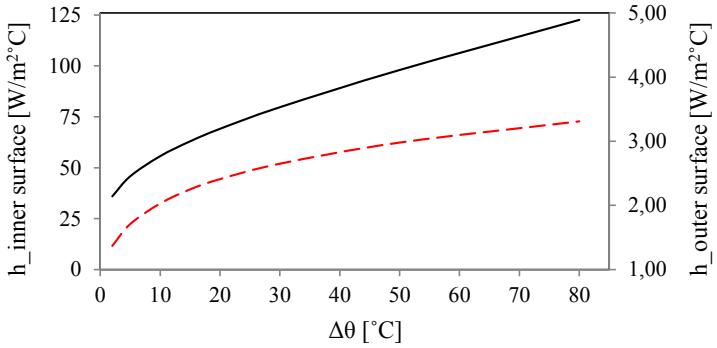

Figure 6.6 Heat transfer coefficients of the bottom, solid trace: Inner surface, dashed trace: Outer surface

Table 6.4 Tuning factors resulting from fitting to measurements of LV and HV sides (Reference to Figure 6.7 and Figure 6.10)

Tuning factor	K_S (Conductivity)	K_H (Tank height)	K_L (Linear inductances)	K_{th} (Tank thickness)
LV side	0.5	0.4	0.88	2.5
HV side	1.5	0.9	1.5	2.5

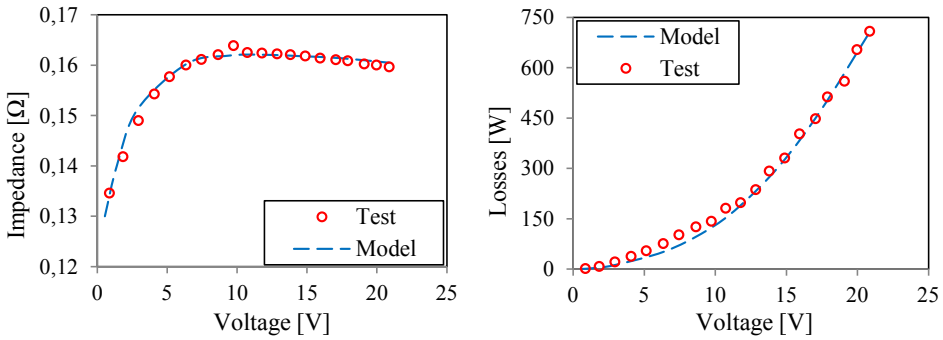

Figure 6.7 The model results in terms of the off-core impedance (Left) and losses (Right), LV side

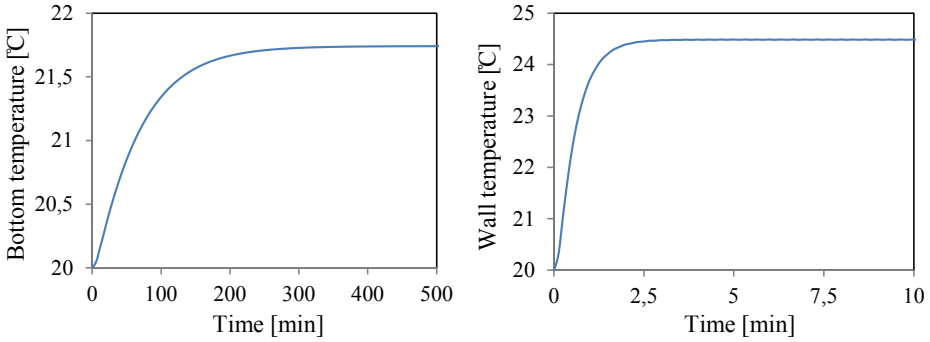

Figure 6.8 Temperature of the wall (Right) and the bottom (Left), LV side

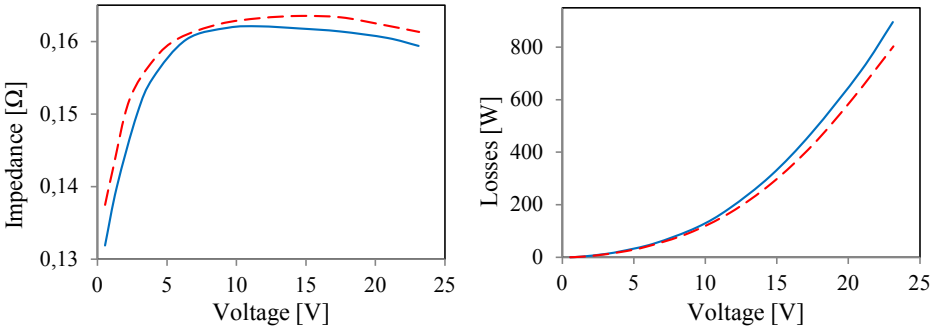

Figure 6.9 Influence of the oil temperature on calculated impedance and losses - LV side, the oil average temperature equals to 20 °C for both wall and bottom thermal models (solid traces), the oil average temperature is 55 °C for the wall thermal model and the bottom oil temperature is 40 °C for the bottom thermal model (dashed curve)

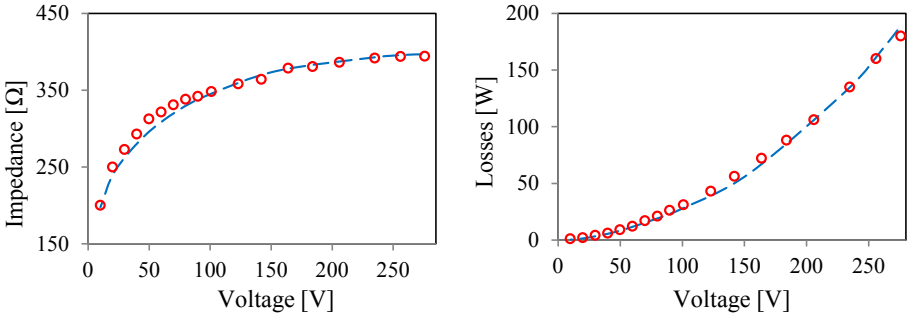

Figure 6.10 The model results in terms of the off-core impedance (Left) and losses (Right), HV side

6.2 SC-ZS characteristics

In order to verify the SC-ZS characteristics for the overall equivalent circuit (as presented in Chapter 3), SC-ZS inductances calculated from the overall equivalent circuit (see Appendix 3) is verified with the values obtained with 3D-FEM (see Appendix 3).

SC-ZS inductance seen from the outer winding differs from the inductance seen from the inner winding. This can be explained through the circuit as shown in Figure 6.11 (only phase A is included for readability). For example, if ZS voltage is applied to the inner winding (LV side) with outer winding short-circuited, the outer winding resistance connects parallel to the off-core circuit neglecting the yoke's effects. Since the winding resistance is much smaller than the off-core impedance, it could be claimed that the off-core path impedance is by-passed with the resistance of the winding. As a result, the SC-ZS impedance seen from the inner winding equals (slightly higher) the SC-PS impedance. In contrast to this, when the outer winding is exciting and the inner winding is short-circuited, the off-core circuit connects parallel to the series impedance of the leakage inductance and the inner winding resistance, as shown in Figure 6.12. The off-core impedance is much larger than the series impedance, meaning that the SC-ZS impedance seen from outer winding is slightly smaller than SC-PS impedance. This explains why SC-ZS impedance is smaller than SC-PS impedance in transformers with Y_N-d vector group [40] (An approach for calculation of SC-PS inductance using the inductance matrix obtained from 3D-FEM is presented in Appendix 3).

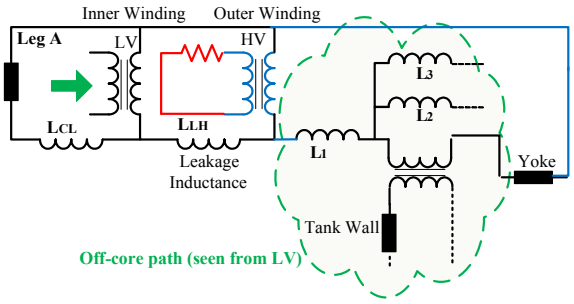

Figure 6.11 Illustration of SC-ZS impedance seen from LV, the off-core path connects parallel to the HV winding resistance (colored red)

Table 6.5 includes SC-ZS impedances seen from the LV and HV sides for Unit 1 obtained from the equivalent circuit for the five simulation cases, as introduced in Table 5.1. SC-PS impedance seen from LV and HV sides are, respectively, 7.4 mΩ and 17.4 Ω for Unit 1. As can be seen, SC-ZS impedance seen from LV side (HV short-circuited) equals SC-PS impedance for all the cases. However, HV side values (LV short-circuited) are slightly smaller than SC-PS impedances due to the influence of the off-core inductances, as explained earlier in this section. This influence is more visible for Case 2 because the off-core inductance is much smaller than the other cases (see Table 5.3). As a matter of fact, the walls with flux-tangential boundary condition is similar to a short-circuited turn and the

inductance seen from HV equals the parallel connection of leakage inductances between HV-LV and HV-Wall. The results from the equivalent circuit have good agreement with the results obtained directly from 3D-FEM as presented in Table 6.6 demonstrating the adequacy of the circuit model in representing SC-ZS characteristics.

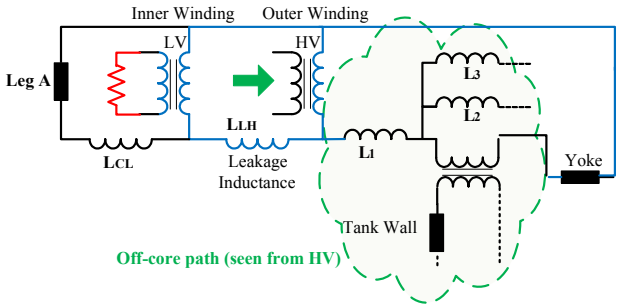

Figure 6.12 Illustration of SC-ZS impedance seen from HV, the off-core path connects parallel to series impedance of the leakage inductance and the LV winding resistance (colored red).

As stated in Chapter 5, the tank walls act between two extreme states (due to non-linear behavior of the wall steel) of flux-tangential and flux-normal boundary conditions and hence SC-ZS impedance will be non-linear to some extent. Using the detailed wall model presented in Chapter 5, SC-ZS impedances seen from the HV side (LV short-circuited) - both calculated and measured - are shown in Figure 6.13. As can be seen, the impedance is slightly voltage dependent at lower voltages, but tends towards the impedance of Case 1 (in which the tank walls are set to the flux-normal boundary condition). When the LV side is short-circuited, the wall is magnetized at relatively low and medium flux densities where the magnetic working point remains in the linear region of the B-H curve. This, together with relatively high resistance of the corrugated walls, leads to a behavior resembling flux-normal boundary condition. At very low voltages, the working point moves to the initial region of the B-H curve leading to the inductance (permeability) reduction. However, this may be different in transformers with plain walls where the wall resistance is much lower and, thus, the wall magnetic behavior may approach to the flux-tangential boundary condition.

Table 6.5 SC-ZS impedance calculated with the equivalent circuit for Unit 1

Unit 1	LV short-circuited			HV short-circuited		
	Z [Ω]	L [mH]	R [Ω]	Z [Ω]	L [uH]	R [Ω]
Case 1	16.8	51.6	4.5	7.4E-03	22.6	1.96E-03
Case 2	13.4	41.0	3.7	7.4E-03	22.8	1.95E-03
Case 3	16.6	50.9	4.4	7.4E-03	22.6	1.96E-03
Case 4	16.8	51.6	4.5	7.4E-03	22.6	1.96E-03
Case 5	16.6	50.9	4.4	7.4E-03	22.6	1.96E-03

Table 6.6 Comparison of SC-ZS inductances calculated with 3D-FEM and equivalent circuit

Simulation Cases		Unit 1	
		LV Short-circuited [mH]	HV Short-circuited [μH]
1	Equivalent Circuit	51.6	22.6
	3D-FEM	51.1	22.5
2	Equivalent Circuit	41.0	22.8
	3D-FEM	41.1	22.7
3	Equivalent Circuit	50.9	22.6
	3D-FEM	51.1	22.5
4	Equivalent Circuit	51.6	22.6
	3D-FEM	51.2	22.5
5	Equivalent Circuit	50.9	22.6
	3D-FEM	51.1	22.5

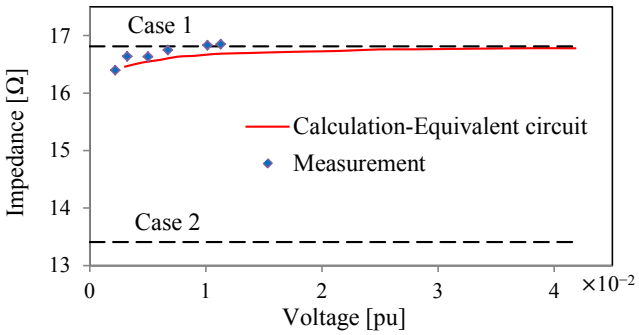

Figure 6.13 SC-ZS impedance seen from HV side (LV short-circuited) - Unit 1

Chapter 7

Applications

7.1 DC biased operation of transformers

As stated in Chapter 1, Section 1.2.1, to analyze DC biased transformers, it is necessary to include a sufficiently detailed model for the off-core flux path. This is of great importance for 3-legged cores where the off-core path is the only way that the flux closes its loop. However, the cores of the 5-legged type also need a proper representation of the off-core path when the outer legs saturate and the flux flowing off the core increases [14].

7.1.1 The wall magnetization - AC excitation with DC offset

In order to analyze the wall magnetization under DC biasing, the wall model presented in Chapter 3, Section 3.3, is used in a simple test circuit, as illustrated in Figure 7.1. The AC is a voltage source representing the power network with a frequency of 50 Hz and the DC represents any source driving DC current into the transformer winding such as GIC. The GIC has a very slow nature with a frequency range of 0.0001 Hz to 1 Hz (to be the period in the range of seconds to hours) [106]. Most researchers have considered GIC to be as a step function, which drives the DC current through the neutral point of windings.

In the following simulations, a step voltage is used to represent the driving source of the GIC. The wall is considered with a height of 1.0 m, thickness of 4.0 mm and with the same length as the wall circumference of Unit 1, which is 2.88 m.

Figure 7.2 through Figure 7.4 show the simulation results including the magnetization current, eddy current induced in the wall inner surface and the losses for the wall conductivity of 6410 kS/m. The AC excitation has been tuned in such a way that the maximum flux density at the inner surface of the wall (denoted with B_m in the figures) becomes 0.1 T (Figure 7.3) and 1 T (Figure 7.2). As can be seen in the results:

1. Only the magnetizing current contains a DC component, whereas the eddy currents induced are free from this at steady state, as seen in the Figure 7.2 and Figure 7.3.
2. The losses increase with GIC in general; however, it is less effective at lower flux densities, as seen in Figure 7.4 (Left).
3. The flux generated by GIC does not induce any voltage, and thus, any current, due to its stationary nature (at steady state). Accordingly, no losses in the wall are generated by GIC itself. However, DC (at steady state) combined with AC flux shifts the AC flux on the B-H curve that causes an increase in the losses.

In order to investigate the impact of time varying nature of GIC, the simulations at B_m=1 T and GIC=20 A are repeated. In this simulation, a sinusoidal voltage source (with an amplitude of 20 A) is used to represent the GIC source (instead of the step voltage source in Figure 7.1) that is positively shifted to give a DC component of 20 A at frequencies of 1 Hz, 0.5 Hz and 0.1 Hz. As can be seen in Figure 7.4 (Right), frequency sweep from 0 Hz to 1 HZ has almost no significant influence (less than 2%) in the losses.

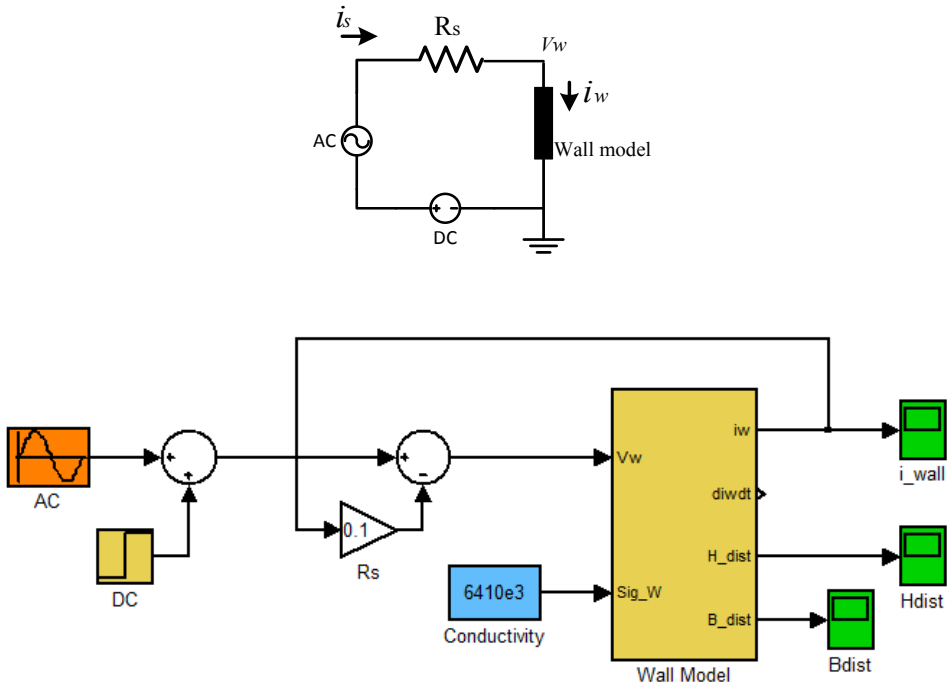

Figure 7.1 The circuit (top) considered for DC magnetization of the wall and its implementation (bottom) in MATLAB-SIMULINK

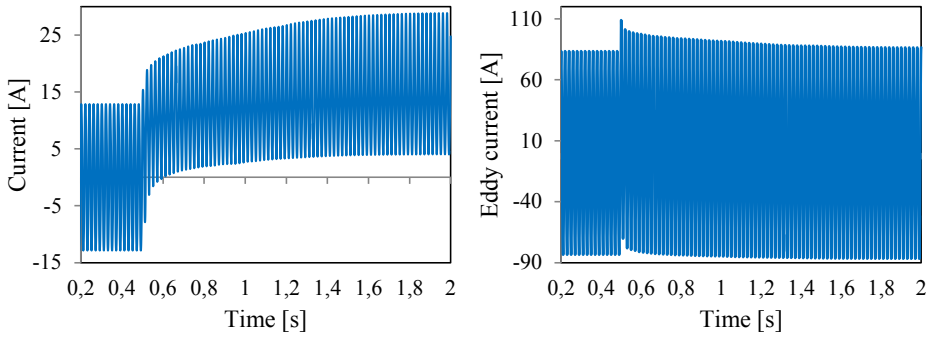

Figure 7.2 Wall magnetization current (Left), Wall eddy current induced - Inner surface (Right) at B_m=1 T, GIC=15 A, Conductivity=6410 kS/m

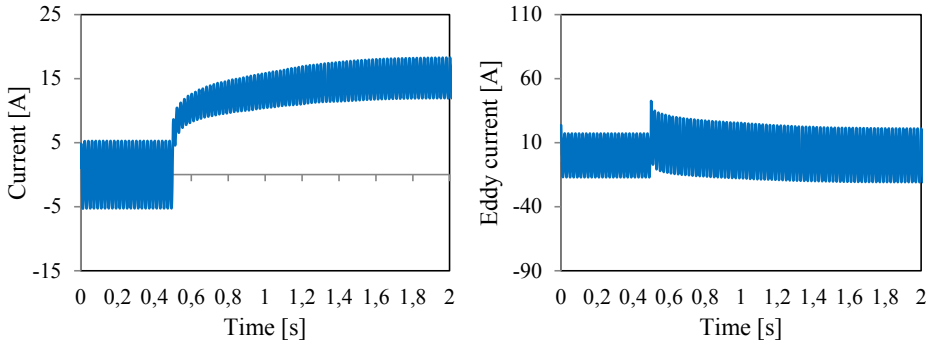

Figure 7.3 Wall magnetization current (Left), Wall eddy current induced - Inner surface (Right) at B_m= 0.1 T and GIC = 15 A, Conductivity = 6410 kS/m

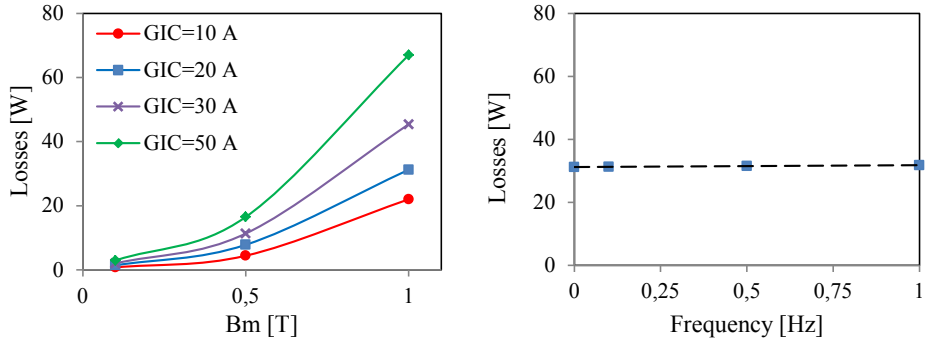

Figure 7.4 Wall losses at different GIC and B_m amplitudes (Left). Variation of the losses at different GIC frequencies when GIC is considered as a sinusoidal voltage source with an amplitude of 20 A positively shifted to give a DC component of 20 A, and B_m = 1 T (Right)

As a conclusion to this section:

1. The AC off-core flux in the wall is the key when GIC occurs. The DC flux that is not generating any losses in the wall by itself, however, influences the AC losses by shifting the magnetic working point on the B-H curve of the wall steel.
2. The time varying nature of GIC (with frequency as low as 1 Hz and below) does not influence the losses significantly.
3. When the wall losses can be neglected, it is possible to eliminate the tank branches from the model (except for the tank equipped with magnetic shields) and replace them with open-circuits (that means the tank behaves like a flux-normal boundary condition). This is mainly because the magnetic penetration depth is significantly larger than the wall thickness at such low frequency of GIC, and the wall reluctance against the oil-gap reluctance is negligible. The off-core inductance to be used in the overall model is therefore the inductance as calculated for Case 1 (see Table 5.1).

7.1.2 Simulation of Unit 1 subjected to GIC

Operation of Unit 1 under GIC event is studied using the model tuned in Chapter 6. Figure 7.6 shows the simulation circuit where the load Z_L is supplied through the transformer Unit 1 at the HV side. The LV side is connected to the network with stiff voltage source. The transformer is loaded at 70% with Z_L=10+jω1.97. The R_S is a negligible resistive series source impedance of 20 mΩ. To represent the GIC, a DC voltage source is applied between the ground and the neutral point of the HV winding.

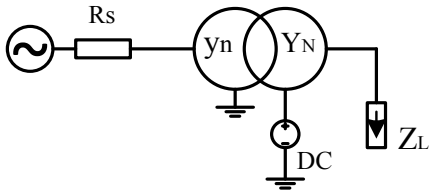

Figure 7.5 System topology used in the simulations

The transformer is represented by the overall model shown in Figure 7.8 with the following considerations.

- Since the magnetizing current gets high orders of harmonics with high magnitudes when the transformer is subjected to GIC, an accurate estimation of winding losses at higher frequencies is necessary. The primary side (that is LV winding) consists of one layer of 21 turns. The DC resistance (R_{LV_DC}) of the winding is equal to 0.00082 Ω that is modified with (7.1) to include the AC effects [107].

$$R_{LV\_ac} = R_{LV\_DC} \cdot \text{Real}\left(u \cdot \left(\coth(u) - \frac{2}{3}\tanh(u) + \frac{2}{3}n_l{}^2 \tanh\left(\frac{u}{2}\right)\right)\right) \tag{7.1}$$

where R_{LV_ac} is the ac resistance of the LV winding and $u = (1+j)\frac{a}{\delta}$, a is the diameter of the winding conductor, $\delta = \sqrt{2/\sigma_{cu}\mu_0\omega}$ (whereas σ_{cu}: the copper electric

conductivity = 58 MS/m, μ_0: free space magnetic permeability, ω: angular frequency) is the magnetic penetration depth in copper, and n_l is the number of layers = 1.

The equation (7.1) is realized through a Foster series circuit consisting of one R-L cell, as shown in Figure 7.6 (Left). The parameters are identified as 0.00082 Ω, 0.00356 Ω and 2.0×10^7 H for R_{LV_DC}, R_{s1} and L_{s1}, respectively. Figure 7.6 (Left) shows fitting quality of the identified Foster circuit in representing (7.1).

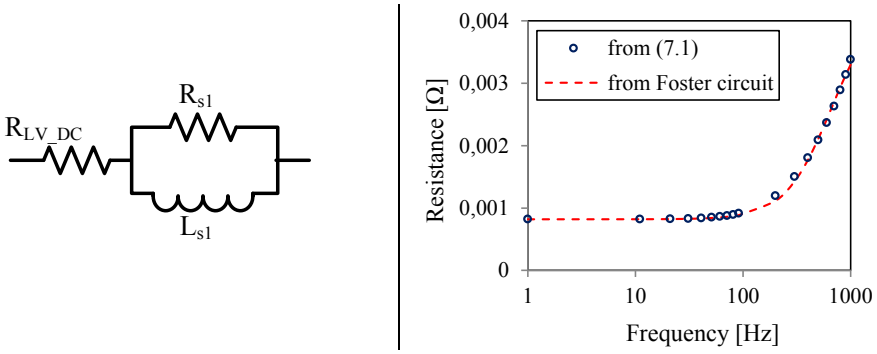

Figure 7.6 Left: Foster equivalent circuit, Right: AC resistance of the LV winding vs. frequency

- Non-linear branch of the main legs and yokes is modeled by means of a parallel R-L circuit with constant resistance and non-linear inductance representing the core losses and the magnetization characteristics of the core, respectively. Parameters of the core are estimated by fitting to the no-load test results, as discussed in [61] [64] [108]. Figure 7.7 shows the magnetization characteristics of the leg and the yoke. The losses equivalent resistances are 101.3 Ω and 103.5 Ω for the leg and the yoke, respectively.

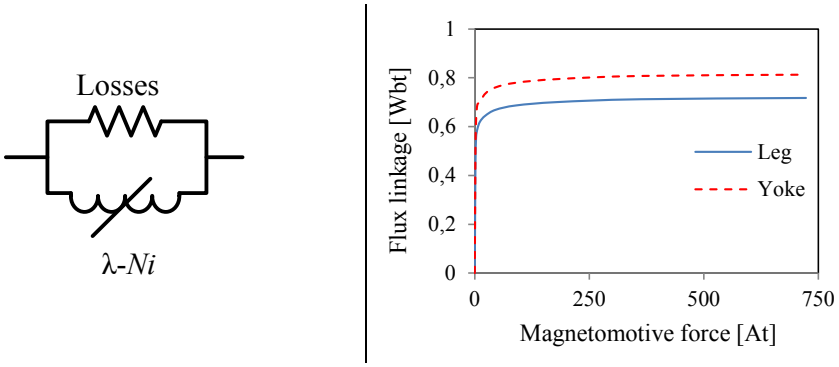

Figure 7.7 Left: Core equivalent circuit, Right: Magnetization characteristics of the core (Unit 1)

- Leakage inductance (L_{LH}) between the windings is obtained from short circuit test as 23.3 uH [61]. The inductance L_{LC} between the innermost winding and the core leg is estimated as one third of leakage inductance (=7.8 uH) [61].
- The off-core equivalent circuit presented in Chapter 6, Section 6.1.2, which is tuned for the HV side, is used to represent the DC flux path outside the core.

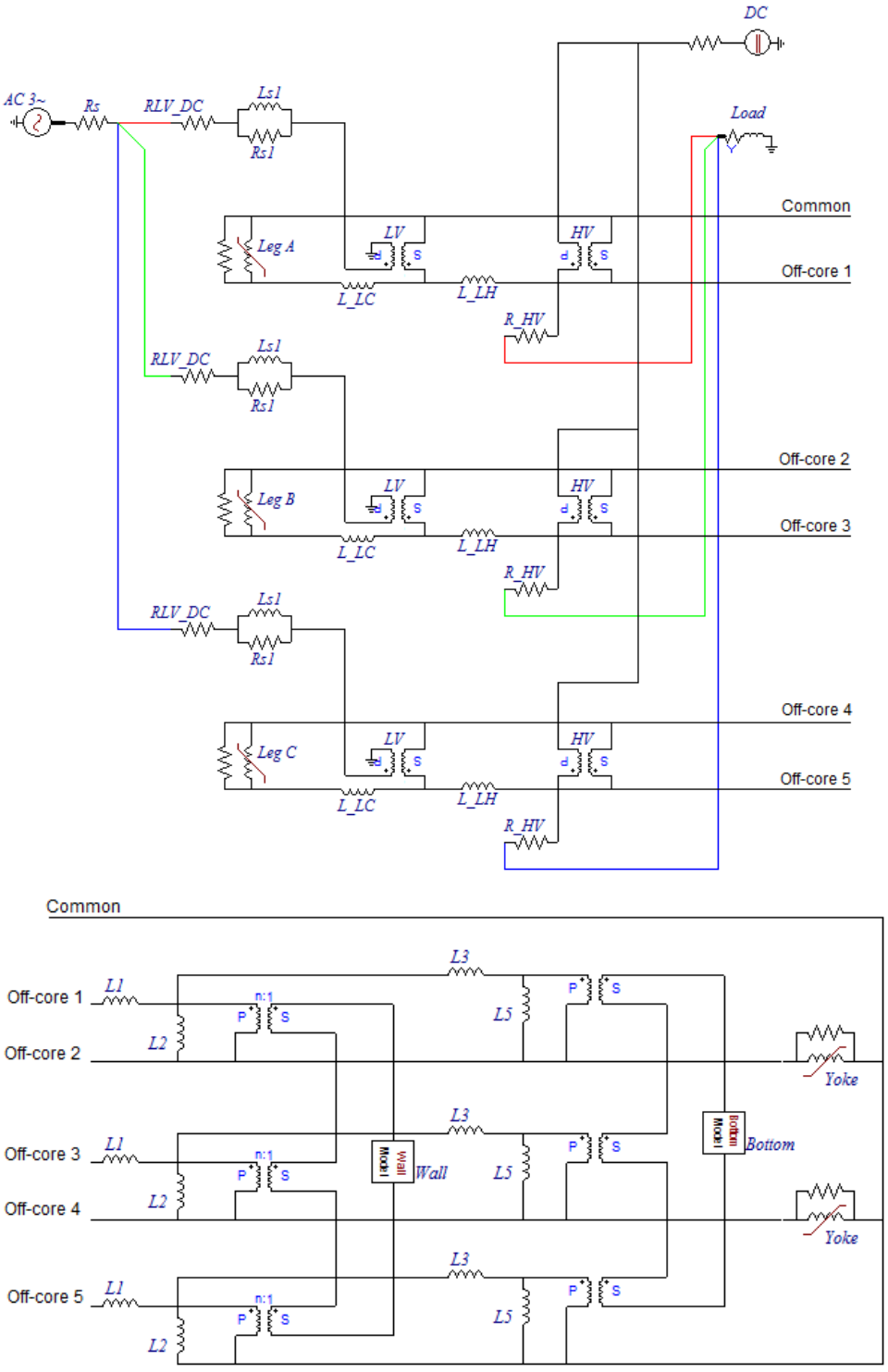

Figure 7.8 The dual circuit model implemented in ATPDraw for GIC simulations

As concluded in Section 7.1.1, the walls resemble the flux-normal boundary condition for the DC flux. Hence, the DC current should not see the tuning factors of the linear inductances or the calculated flux will be underestimated. Since all the linear inductances are tuned by the same factor, dividing the DC source by this factor will compensate its effect. In the following simulations, the GIC/K_L is thus applied to the intended transformer. In addition, it is applied as a step function with a slow rise time of 3 s preventing high frequency transients.

Figure 7.9 shows the magnetizing currents at different GIC levels. As can be seen, the half cycle saturation of the core results in a considerable increase in the half cycle of the magnetizing current. Figure 7.10 shows the effective values of the magnetizing currents versus the GIC levels.

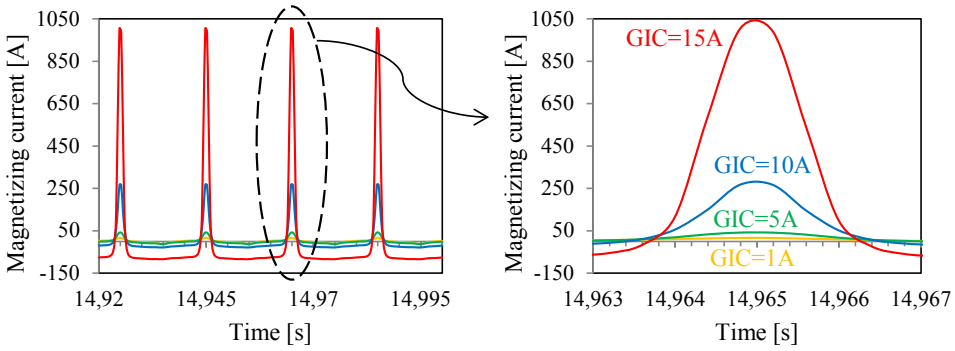

Figure 7.9 Magnetizing current at different levels of GIC

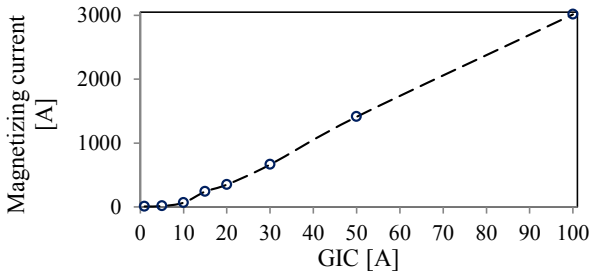

Figure 7.10 The effective (rms) values of magnetizing current as a function of GIC levels

Highly distorted magnetizing current (see Figure 7.9) results in a large amount of harmonics injected to the network. Figure 7.11 shows the harmonic content of the magnetizing current normalized by the main component (50 Hz) for the GIC=10 A and GIC=100 A at the neutral point. As can be seen, both even and odd harmonics exit in the frequency spectrum of the magnetizing current that should be taken into account in protection relays setting.

The voltage and current induced in the wall are shown in Figure 7.12. As can be seen, with fully symmetrical network voltages, there is no zero sequence voltage and thus no

considerable voltage (and then current) induced in the walls. The losses due to such inductions in the walls are negligible even at a GIC of 100 A.

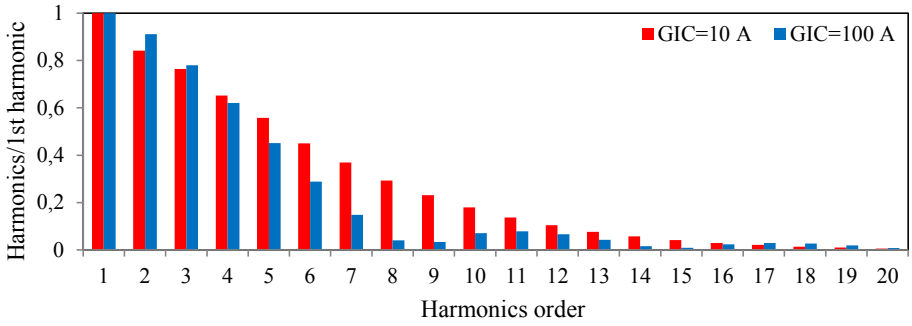

Figure 7.11 Harmonic content of the transformer magnetizing current

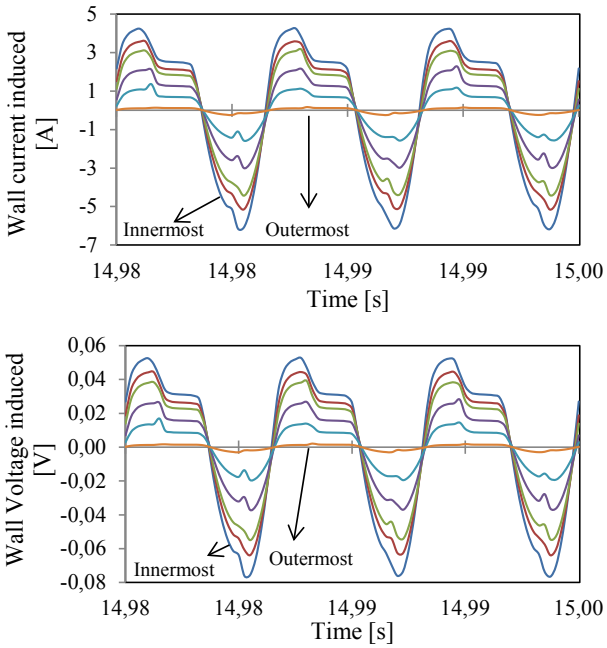

Figure 7.12 Distribution of voltage (Bottom) and current (Top) induced in the walls at GIC=100 A

Figure 7.13 compares the currents induced in the innermost layer of the wall and the bottom at GIC=100 A. As can be seen, the bottom has a considerable contribution that cannot be neglected in the modeling of the tank.

The magnetizing currents of the wall and the bottom are also shown in Figure 7.14. As can be seen, the DC magnetizing current is the major component as expected. Moreover, it can be observed that both have the DC values superimposed on the AC currents.

In addition to the time domain waveforms, the frequency content of the wall currents is also informative. Figure 7.15 shows the frequency spectrum of the wall magnetizing

(flowing through the first non-linear inductor in the equivalent circuit) and eddy currents in the first (innermost) layer of the wall discretized up to 20th harmonic. As can be seen, the eddy currents flowing through the walls only include the zero sequence harmonics consisting of 3rd, 6th, 9th, etc. However, the wall magnetizing current includes a dominant DC component, which is far larger than the AC components. These results are expected, since:

- the wall is encompassing all three phases meaning that the voltages induced by each phase summed up and due to 3-phase symmetry are cancelled out leaving only zero sequence harmonics. It must be noted that the geometrical symmetry of the transformer from the off-core flux path point of view can influence this result. In other words, if the tank distance to the outer phases is different, the off-core linear inductances will be different for each phase, thus resulting in asymmetric voltages induced in the walls. Hence, the positive sequence frequencies will also exist in the induced wall current.
- the DC flux does not induce any voltage in the wall and thus, the current, which generates the losses in the walls, has no DC component.
- the DC magnetizing currents flowing through the non-linear inductors are responsible for the DC flux in the tank. The magnitude of the DC current is far larger than the AC components due to the GIC in the secondary winding.

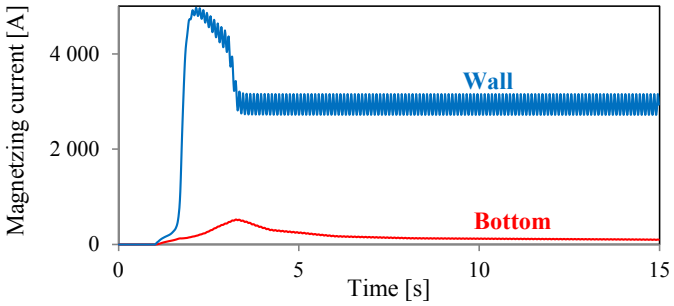

Figure 7.13 The wall and the bottom magnetizing current - Innermost layer at GIC=100 A

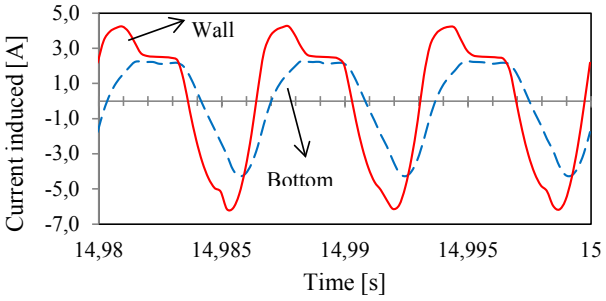

Figure 7.14 The current induced in the wall and bottom - Innermost layer at GIC=100 A

In contrast to the wall and the bottom currents, the currents in the linear inductors linked to each phase include the fundamental frequency (50 Hz) in addition to the higher frequencies as can be seen in Figure 7.16. As explained, the harmonics other than third multiples are of

positive sequence quantities that are cancelled out in the tank (walls and bottoms). The DC component is not shown in the bar diagrams of Figure 7.16, emphasizing the AC components.

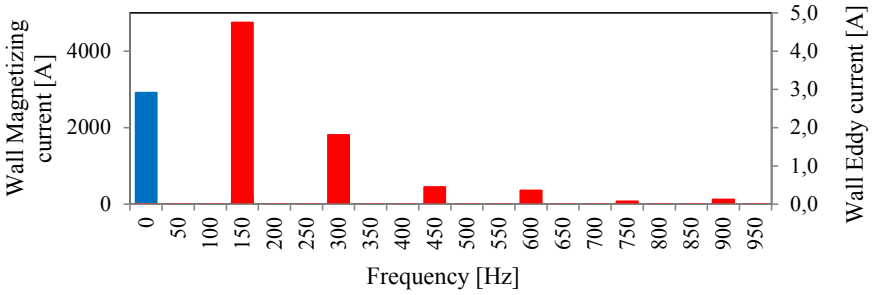

Figure 7.15 Frequency spectrum of the wall magnetizing (Blue bars) and eddy currents (Red bars) in the innermost layer, GIC=100 A

It is worth noting that the core clamping and the tie bars can be considered in parallel to the linear inductors of the L_1, L_2 and L_3. In fact, these metallic parts are magnetically in series with the oil gaps. It can be concluded that the heating effect during GIC events due to the flux in the tie bars and the core clamp may be potentially more significant than in the tank walls. Investigation of the losses in these parts and considering them in the circuital modeling is, however, out of scope of this PhD work.

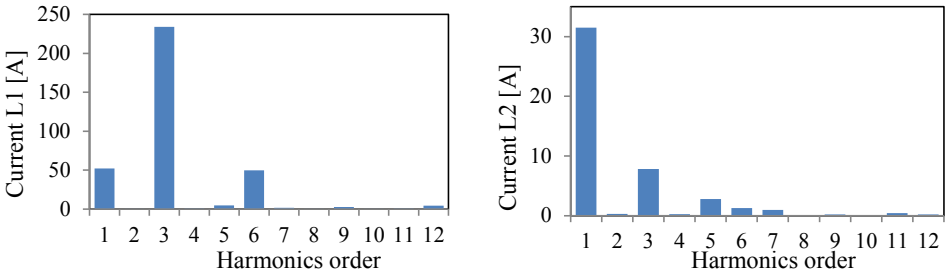

Figure 7.16 Currents of the inductors L_1 (Left) and L_2 (Right)

The reactive power consumption of Unit 1 during GIC events is shown in Figure 7.17 as a function of GIC level. A linearly relationship between the reactive power consumption and GIC is repeatedly reported in the literature. In order to see the effect of the tank in the overall reactive power seen from LV side, the lossless model of Case 3, which is the closest to the test results as shown in Section 6.1.1, is also simulated and the results are shown in Figure 7.17 with the dashed trace. As can be seen, the reactive power is overestimated when the lossless model is used compared to the results from the complete model.

There is similar behavior for the magnetizing current, active and apparent power seen from LV side as shown in Figure 7.18, Figure 7.19 and Figure 7.20. As shown in Figure 7.20, the apparent power is exceeding the rated power at approximately GIC=65 A using the complete model, while it is estimated to occur at GIC=55 A when using the lossless model.

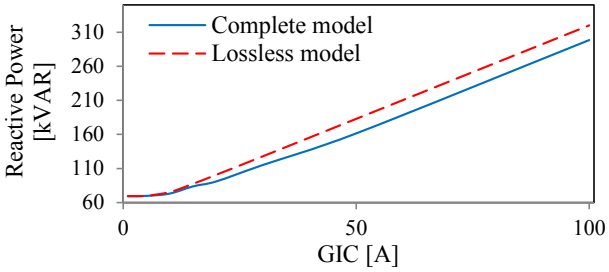

Figure 7.17 Reactive power of Unit 1 versus GIC

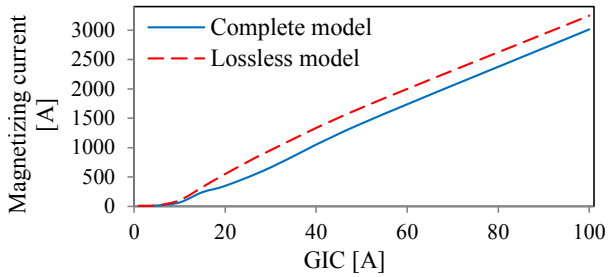

Figure 7.18 Magnetizing current (rms) versus GIC

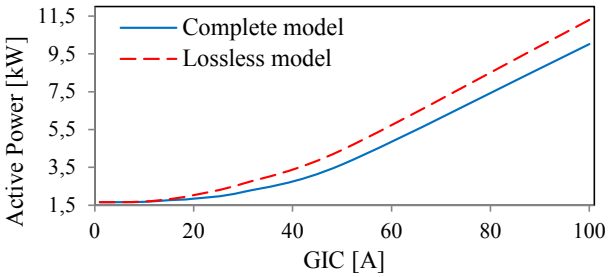

Figure 7.19 Active power seen from LV side versus GIC

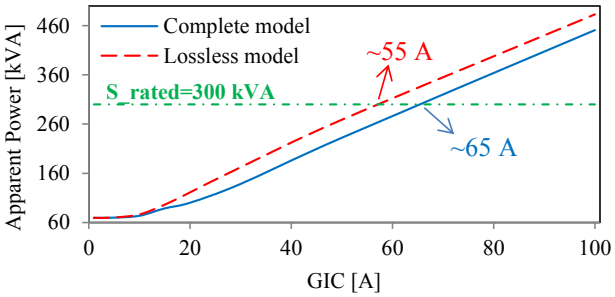

Figure 7.20 Apparent power seen from LV side at different GIC levels

7.2 Unbalanced operation of 3-phase transformers

Asymmetrical operation of transformers occurs in two cases:

1. Primary-side voltage unbalance
   This condition occurs when the 3-phase voltage applied to the primary side is not symmetrical. This means that there is a ZS component of voltage, which drives the ZS current resulting in the ZS flux.

2. Secondary-side load unbalance
   This condition occurs when the load connected to the secondary side of transformer is not symmetrical meaning that the load impedance of the phases differs from one another resulting in ZS loading of the transformer. In this case, a ZS current source can represent the unbalanced load.

Depending on which winding, the inner or the outer, is driving the ZS current, the ZS flux path is different as shown in Figure 7.21. As can be seen, when the inner winding supplies the ZS current, the ZS flux path includes the core in series with the leakage channel parallel to the off-core path. The ZS flux path is different when the outer winding supplies the ZS current. In this case, it includes the off-core path in series to the leakage channel parallel to the core. In both cases, the flux in the leakage channel depends on the electric impedance of the other (than the one excited with the ZS voltage/current) winding. The lower the impedance, the higher the flux in the leakage channel will be. This impedance can be either the load impedance (for the primary-side voltage unbalance) or the network equivalent impedance at the primary side (for the secondary-side load unbalance). These different flux paths depending on the ZS excited side explains different ZS impedances measured from HV and LV sides, as also discussed in Section 6.2.

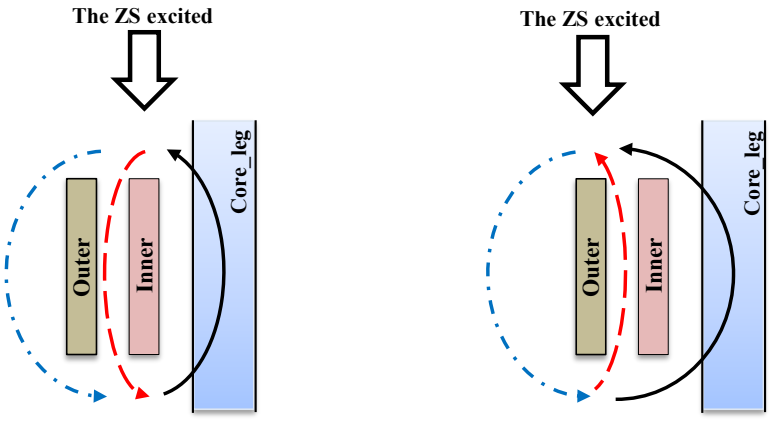

Figure 7.21 The ZS flux path depending on which winding drives the ZS current, Left: Inner winding supplies the ZS current, Right: Outer winding supplies the ZS current

The dual circuit model consisting of a detailed off-core path equivalent circuit, introduced in this thesis, can conveniently represent the different ZS excitation cases. As an example,

Table 7.1 illustrates the cases where the LV (inner winding) is the primary and the HV (outer winding) is the secondary with the steady state equations of the ZS impedances. The same symbols are used for both impedances in order to prevent complications caused by the overuse of symbols; however, they are referred to the side, which is excited.

The first row shows the primary side voltage unbalance (LV side) situation where the load impedance is connected to the off-core impedance in parallel, then in series with the leakage and network common point impedance (Z_S). The impedance $Z_{S+Leakage}$ is equal to $Z_S+Z_{Leakage}$ where $Z_{Leakage}$ includes the winding resistance plus leakage inductance.

The second row shows the secondary side load unbalance (HV side) situation where the zero sequence load current (I_0) sees $Z_S+Z_{Leakage}$ in parallel to $Z_{off\text{-}core}$ as the transformer zero sequence impedance.

Table 7.1 Zero sequence current path for loaded transformer, the HV (outer winding) side is considered secondary connected to the load, and LV side (inner winding) is considered primary connected to the network through Z_S

Circuit diagram	ZS Impedance Steady state
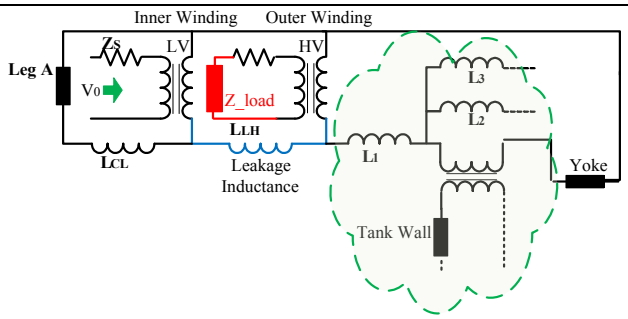	$Z_0=(Z_{load}\|\|Z_{off\text{-}core})+Z_{S+leakage}$ (all impedances are referred to LV side)
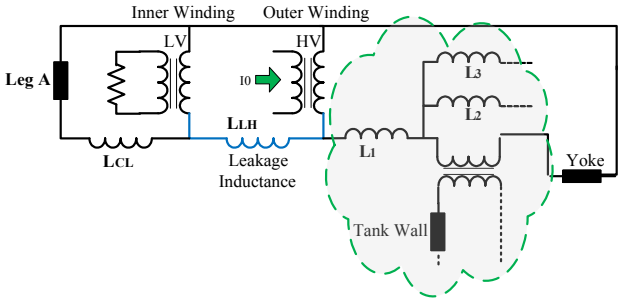	$Z_0=(Z_{S+leakage}\|\|Z_{off\text{-}core})$ (all impedances are referred to HV side)

Considering Unit 1, each term of the equations given in Table 7.1 can be calculated as follows:

1. If the unit is loaded with rated power of 300 kVA at the HV side with rated voltage of 11430 kV, a load impedance of $\frac{11430^2}{300000} = 435.5\ \Omega$ magnitude per phase is needed. Referring to the LV side with turn's ratio squared (48.67), it becomes 0.184 Ω.

2. As presented in Chapter 5, Section 5.4, the $Z_{off\text{-}core}$ of Unit 1 varies from 0.13 Ω to 0.16 Ω from the LV side, and between 200 Ω and 400 Ω from HV side.
3. The impedance $Z_{S+Leakage}$ has a magnitude of 0.0074 Ω (R_{HV}+j$X_{Leakage}$ referred to LV) seen from LV side, and 17.52 Ω (R_{LV}+j$X_{Leakage}$ referred to HV) seen from HV side.

As can be seen, Z_{load} (0.184 Ω) and $Z_{off\text{-}core}$ (0.13-0.16 Ω) are comparable in magnitude meaning that the zero sequence current is equally shared between the load and the off-core inductance.

However, from the load side (the HV), $Z_{S+Leakage}$ and $Z_{off\text{-}core}$ are 17.52 Ω and 200 Ω (varying up to 400 Ω), respectively. Therefore, the off-core is easily bypassed, resulting in lesser current to the off-core branch.

7.2.1 Unbalanced simulation of Unit 1

To investigate the explanations given above with time domain simulations, the model introduced and developed in Chapter 3 and Chapter 5 is run with voltage unbalance as well as load unbalance condition. As illustrated in Figure 7.22, the overall model of the transformer Unit 1 is implemented in ATPdraw. As discussed in Chapter 5, only the wall and the bottom are taken into account since the cover has no impact on the results. The off-core path parameters are those as presented in Chapter 5, Section 5.4. The LV winding is the primary connected to the voltage source and the HV winding is the secondary connected to the load. Non-linear branches of the legs and yokes, leakage inductance (L_{LH}) and core-inner winding inductance (L_{LC}) are identified through using no-load and short circuit test results [103] [108]. The R_n and R_N are neutral resistances of the windings and R_g is the load neutral resistance, which have relatively small values of 1 μΩ. Two unbalanced situations are examined with, first single phase to ground short circuit at the primary side, and, second with single phase to ground short circuit at the secondary side as extreme scenarios of two unbalance situations. The currents flowing through the neutral resistances (LV and HV windings) as well as through the off-core circuit (Current of L_1) are considered as outputs. Figure 7.23 shows the results for the first scenario, with single phase to ground fault at the transformer LV terminal. Zero sequence phase currents are obtained with equations of $I_0\_Primary = \frac{I\_R_n}{3}$, $I_0\_Secondary = \frac{I\_R_N}{3} \times 48.667$ where 48.667, I_R_N and I_R_n are the HV/LV turns ratio, HV side neutral current and LV side neutral current, respectively.

As can be seen, the zero sequence current flowing through the secondary side is much lower than that of the off-core path as could be expected from the previously provided explanations in Section 7.2.

Figure 7.24 shows the results for the load side single phase to ground fault where phase A is short-circuited at time 0.5 s. As can be seen, the situation is like load side zero sequence excitation where the phase zero sequence current of the secondary side is larger than that of the primary side. As expected from Table 7.1, the off-core path current is much lower than the phase zero sequence current of primary winding meaning that the off-core path is bypassed by the leakage channel and primary winding resistance.

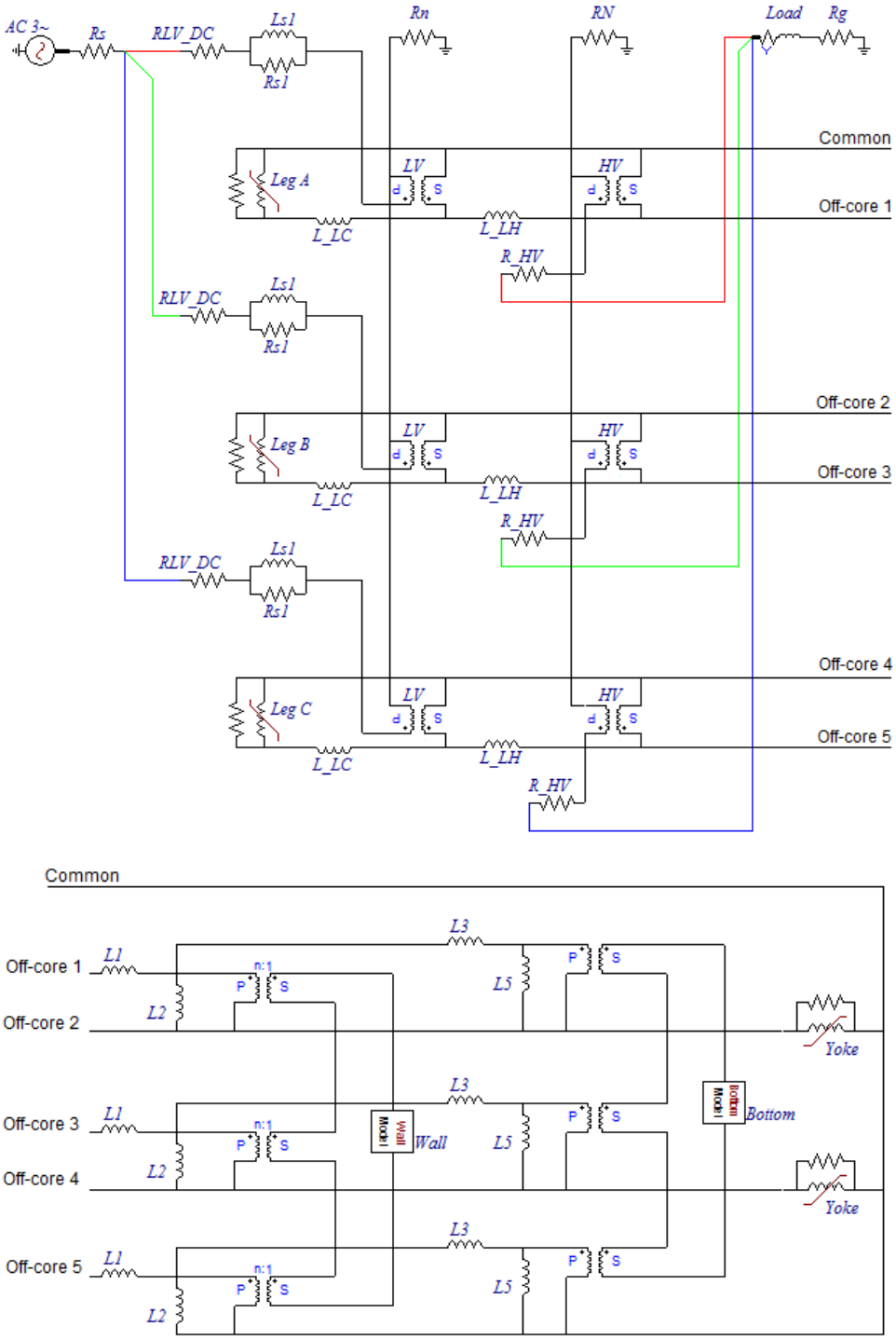

Figure 7.22 The model of Unit 1 implemented in ATPDraw - Only the wall and the bottom are considered since the cover has no impact (as discussed in Chapter 5)

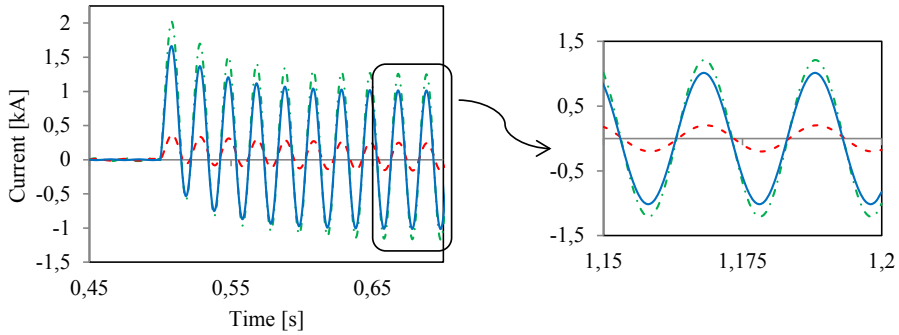

Figure 7.23 Single phase to ground short circuit at the primary side, I_0_Primary (green dotted-dashed) and I_0_Secondary (red-dashed) compared to the off-core path current (blue solid)

In addition to these two extreme scenarios, two more scenarios with single-phase half-load impedance (load impedance of a phase is halved) and half voltage (voltage of a phase is halved) are also considered. Figure 7.25 and Figure 7.26 show the results including zero sequence phase-currents of primary and secondary sides as well as off-core path currents. As can be seen, the half-voltage scenario at the primary side results in higher off-core current than half-load scenario at the secondary side.

As a conclusion of this section, it is again emphasized that the off-core flux can be considerable when the primary side voltage unbalance occurs as well as when asymmetrical high impedance short circuit occurs at the load side. For such situations, the detailed model of the tank is of great importance when the tank flux and its impacts on the ZS impedance and the losses in the walls are of interest.

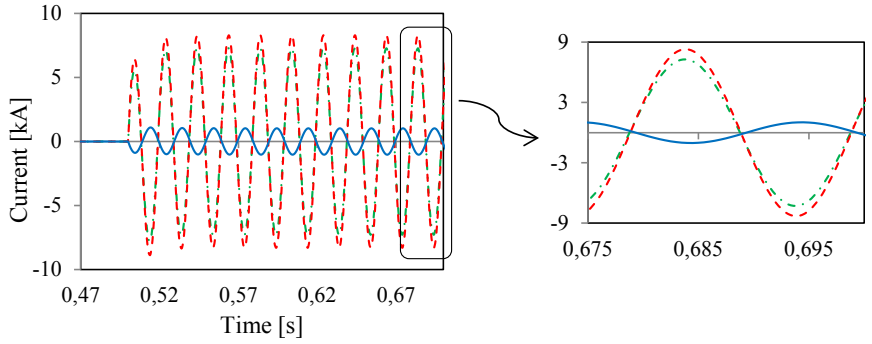

Figure 7.24 Single phase to ground fault at the secondary side, I_0_Primary (green dotted-dashed) and I_0_Secondary (red-dashed) compared to the off-core path current (blue solid)

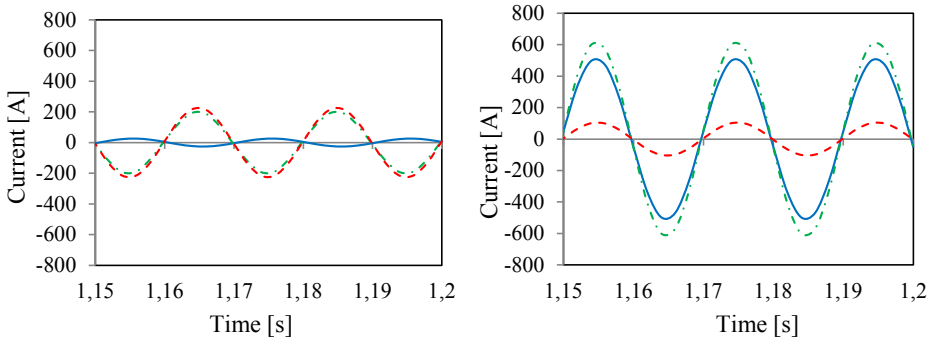

Figure 7.25 Zero sequence currents of the primary (dotted-dashed) and secondary (dashed) sides compared to the off-core path current (solid), Left: single-phase half-load, Right: Single-phase half-voltage

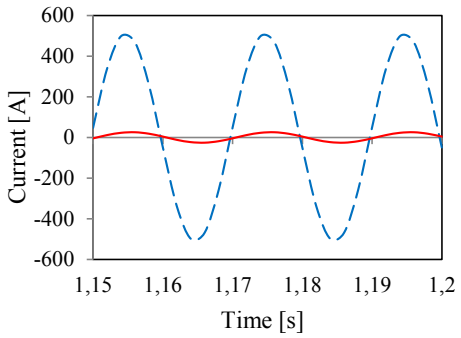

Figure 7.26 The off-core path currents in scenarios half-load (solid red) and half-voltage (dashed blue)

Chapter 8

Conclusions and future works

8.1 Conclusion

A topologically correct equivalent circuit is proposed for the off-core flux path using the duality principle. The tank walls, cover and bottom are realized in the modeling as a non-linear R-L ladder circuit, obtained from the finite difference approximation of the one-dimensional magnetic diffusion equation. The tank sections are connected to the basic equivalent circuit of the transformer (including the core and the windings) with linear inductors representing the oil gaps between the tank and the active part.

Due to the duality feature of the equivalent circuit, the losses of the tank including the wall, the bottom and the cover are modeled in their topologically correct areas. The differences between the ZS impedances seen from different windings are explored at different conditions in terms of magnetic permeability and electric conductivity of the tank. As discussed in the thesis, the impedance difference is negligible when the wall behaves like a flux-normal boundary condition (as it is the case for the walls of corrugated kind or equipped with magnetic shunts). This difference is relatively larger when the wall behaves like a flux-tangential boundary condition (as it is the case for the walls of plain kind or equipped with magnetic shield).

In addition, the thermal effect of the heat generated in the tank is taken into consideration by means of a thermal equivalent circuit. In this thermal model, the tank is considered as a thermal node (no temperature difference between inner and outer sides) connected to the oil and ambient nodes with constant temperatures through non-linear thermal resistances.

There is a set of unknowns to be identified including linear inductances of the oil gaps, dimensional parameters of the tank, electromagnetic/thermal properties of the tank steel and the coolant mediums (the oil and the air) as well as thermal resistances and capacitances. The calculation approaches of the parameters with comprehensive discussions are presented, as detailed in Chapter 5.

In order to identify the electromagnetic properties of the tank steel, extensive magnetic measurements are performed to identify the B-H characteristics (normal curve and hysteresis loops), hysteresis losses, dynamic losses and frequency dependency of each loss mechanisms. The electric conductivity and the temperature coefficients are also measured on the tank steel samples. Further analysis is performed on the measurement results to characterize different loss mechanisms including hysteresis, classical eddy current and excess losses.

The model proposed is implemented in MATLAB-SIMULINK and successfully used to reproduce the OC-ZS and the SC-ZS impedances of the 3-phase, 3-legged transformer under study, termed Unit 1 in this thesis.

As applications of the proposed model, transformers under DC biasing as well as under unbalanced voltage and load conditions are studied.

In the following, a summary of the conclusions for each part the work is provided.

a) Electric equivalent circuit of the off-core flux path

1. The linear inductances of the off-core circuit are calculated using 3D-FEM with extreme boundary conditions on the walls. For this purpose, five simulation cases are defined based on flux-normal and flux-tangential boundary conditions set on the different tank elements (the wall, the cover and the bottom) as detailed in Chapter 3.
2. The tank walls are preliminarily considered with impedance boundary condition to investigate the effect of the walls magnetic permeability and electric conductivity in the terminal off-core inductances. This is compared with the results obtained from the calculations in which the walls are set to extreme boundary condition, as used for computing the linear inductances.
   - As the simulations show, the tank with high magnetic permeability and low electric conductivity behaves like a flux-normal boundary condition. The wall equipped with the magnetic shunts is the design closest to this condition.
   - In contrast, the tank with low magnetic permeability and high electric conductivity behaves like a flux-tangential boundary condition. The wall equipped with the magnetic shields is the design closest to this condition.
3. The walls of corrugated type have larger electric resistance compared to the walls of plain type and this affects the magnetic flux penetration depth.
4. In cases where the tank losses are not of interest, the lossless variations of the proposed model, where the tank is removed and the model is set to the proper boundary conditions (either flux-normal or flux-tangential), can be used instead of the complete model. In such circumstances:

- The walls of corrugated type and the walls equipped with the magnetic shunts can be replaced by a flux-normal boundary condition due to relatively lower effective electric conductivity.
- The walls of plain type and the walls equipped with the magnetic shields can be replaced by a flux-tangential boundary condition due to relatively higher electric conductivity.

5. To fit the off-core model to the measurements, the linear inductances (calculated with extreme boundary conditions on the tank), the tank steel conductivity and the height of the tank must be tuned by proper factors. This is principally a result of the assumption that the flux enters/leaves the tank through single points.
6. The tank's influence on the off-core flux path depends on its relative distance to the active part. The cover is normally far from the core (the winding leads are taken out from the cover) and thus less significant in the off-core flux path. From the simulations of the transformer studied in this thesis, when the ratio between the core-cover distance and the core-wall distance is larger than 2.5, the cover can be neglected. The walls are normally optimized to be relatively close to the active part. The bottom is always right under the core, and thus cannot be neglected.
7. SC-ZS impedance is much lower than the SC-PS impedance when the wall behaves in a similar way to flux-normal boundary condition (as the case for the wall with magnetic shunts and the wall of corrugated type).
8. SC-ZS impedance is slightly lower than the SC-PS impedance when the wall behaves in a similar way to flux-tangential boundary condition (as the case for the wall with magnetic shields and the plain wall).
9. The SC-ZS impedance seen from the inner winding is smaller than that seen from the outer winding due to the off-core impedance. This difference is relatively larger when the wall behaves in a similar way to flux-tangential boundary condition.

b) Thermal equivalent circuit of the tank walls

1. In cases concerning the large off-core flux, the losses in the tank may cause high temperatures such that the electromagnetic behavior changes considerably. The thermal circuit proposed in this thesis can be used to predict the temperature rise and be fed back to correct the electric conductivity of the tank steel and then calculate the losses.
2. The temperature rise causes a decrease in the losses and an increase in the impedance. This can explain why the ZS impedance becomes flatter at higher excitations while it is expected to reduce due to lower permeability at the saturation region of the tank steel.
3. The inner surface of the tank is considered with convection heat transfer coefficients for the vertical walls and the horizontal plates of the cover and the bottom.
4. The outer surface of the tank is considered with both convection and radiation heat transfer coefficients for the vertical walls (plain and corrugated) and horizontal plates of the cover and the bottom.
5. As shown in the simulations, the thermal time constant of the wall and the bottom are different; it is much lower for the wall than the bottom due to easier heat transfer from the wall.

6. Thermal effects on the tank steel may not be significant in the corrugated walls due to the easier heat transfer from the outer surfaces. However, in the plain walls, it may be more effective since the oil cooling radiators are normally installed beyond the walls.

c) Magnetic measurements on the tank steel specimen

1. The ratio between the hysteresis losses and the dynamic losses is notably small in thick steels (while the opposite is the case in the much thinner core laminations) especially at higher excitations. Therefore, the hysteresis can be neglected in electromagnetic modeling of the tank.
2. Since the tank walls are magnetized at wide ranges of flux density, the non-linear behavior of the B-H curve at the initial region as well as the saturation region must be taken into account. For this purpose, the single-value normal B-H curve can be used.
3. The classical eddy current losses are the major part of the dynamic losses in the tank walls thicker than of 4 mm. This means that the excess losses can be easily neglected in large power transformers where the walls are of 6 mm or thicker steel plates. However, the excess losses can be comparable to the classical eddy current losses in the steel plates as thin as 1.25 mm. Such thin walls are common in distribution transformers.
4. Temperature rises have a significant influence on the classical eddy current losses of thick specimens.

d) Simulation of transformers subjected to GIC

1. The walls act like a flux-normal boundary condition for the DC flux. Thus, no voltage is induced in the walls and no losses generated.
2. The off-core AC flux in the wall is the key when GIC occurs. This influences the AC losses by shifting the magnetic working point on its magnetic B-H curve.
3. The time varying nature of GIC does not influence the losses in the wall.
4. The model proposed for the off-core flux path is tuned to reproduce the ZS test results measured at power frequency. The GIC is a near DC current, meaning that the current induced is so small that the wall under such near DC excitation can resemble a wall with a small electric conductivity. In other words, the wall behaves like a flux-normal boundary condition at such low frequency. Hence, the tuning factors of the linear inductances (K_L), which are used for the wall under AC excitation at power frequency, are no longer applicable. To consider this fact, GIC must be divided by the K_L to ensure that the DC flux is shared correctly between the linear inductances.
5. As can be seen in the GIC simulations, the voltage and currents induced in the tank have only third multiplied harmonics, which are of zero sequence kinds. It means that the power frequency flux that leaks from the core during the GIC does not appear in the tank walls. This may reduce the losses in the walls to high extent.
6. The power frequency off-core flux can appear in the off-core linear inductances. The metallic parts of tie-bars and core clamps can be represented with non-linear resistors parallel to the L_1, L_2 and L_3. Hence, the losses in these parts due to the power frequency off-core flux (and thus, the temperature rise) can be increased considerably during the GIC event.

7. Although the losses in the tank walls can be negligible, the tank can influence the reactive power losses and the magnetizing currents during the GIC events.

e) Simulation of transformers under asymmetrical operation

1. Two asymmetrical operations are distinguished as primary-side voltage unbalance and secondary-side load unbalance conditions based on the ZS flux path.
2. In the primary-side voltage unbalance condition, the load impedance affects the flux flowing in the off-core path.
3. If the unbalance condition is on the inner winding side, the ZS flux path includes the off-core paths in parallel to the leakage channel.
4. If the unbalance condition is on the outer winding side, the ZS flux path includes the off-core paths in series to the leakage channel.

8.2 Future works

The model presented in this thesis can be further studied for future works with the following considerations:

I. Calculation of the tuning factors

As presented in this thesis, all the tuning factors are estimated through the fitting to the zero sequence impedance and losses measurements. In the case of lacking such extended zero sequence measurements, the tuning factors must be estimated through numerical simulations of the transformer such as 3D-FEM simulations, as shown for the simple 2D examples in this thesis.

It would be useful if analytical formulas could be obtained for the tuning factors through sensitivity analysis of the 3D-FEM simulations.

II. Benchmarking of the thermal model

To this purpose, the temperature of the tank walls as well as top and bottom oil temperatures should be measured during zero sequence tests. This temperature data can be used in addition to the impedance and losses to verify the overall model.

III. Verifying the overall model with GIC measurements

Having a 3-legged transformer of simple design with plain tank walls and two windings, DC response of the transformer can be measured/obtained in terms of magnetizing current, reactive power consumption, core and winding losses, temperatures in the oil and ambient nodes as well as in the tank walls. Such comprehensive measurements can be used for verifying the overall electromagnetic/thermal model presented in this thesis.

IV. Inclusion of the tie-bars and the core clamping in the modeling

As presented in the thesis, the tie-bars and the core clamping parts see the power frequency off-core flux that leaks from the core during the GIC event. Thus, the losses increase is potentially higher in those parts. As a further development of the proposed

model, these metallic parts can be considered in the modeling process as non-linear branch parallel to the linear inductances of L_1, as shown in Figure 8.1.

V. Inclusion of the magnetic shunts and magnetic shields

Another important issue especially in large power transformers concerns the magnetic shunts and the magnetic shields that can be added to the off-core equivalent circuit, as shown in Figure 8.1.

As concluded in the thesis, the shield acts like the flux-tangential boundary condition forcing the magnetic flux in the gap between the winding excited and the wall (represented with L_1). Thus, the shield can be considered as a resistance connected in parallel to the wall branch through an ideal transformer with turn ratio of one.

In contrast to this, the shunts act like the flux-normal boundary condition sharing the magnetic flux with the wall. Thus, it can be considered as a non-linear branch connected in series to the wall.

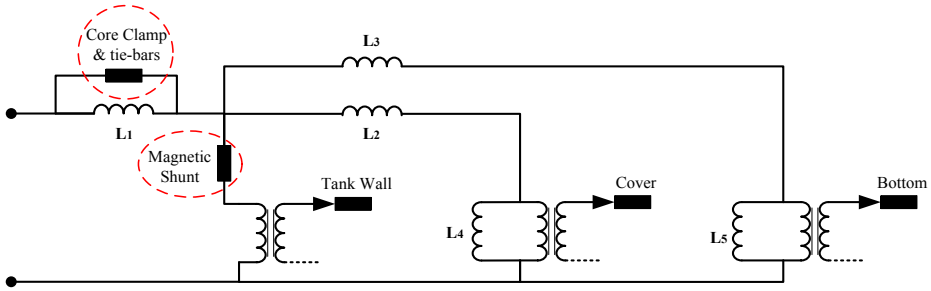

a) The magnetic shunt and the core clamp added to the presented off-core model

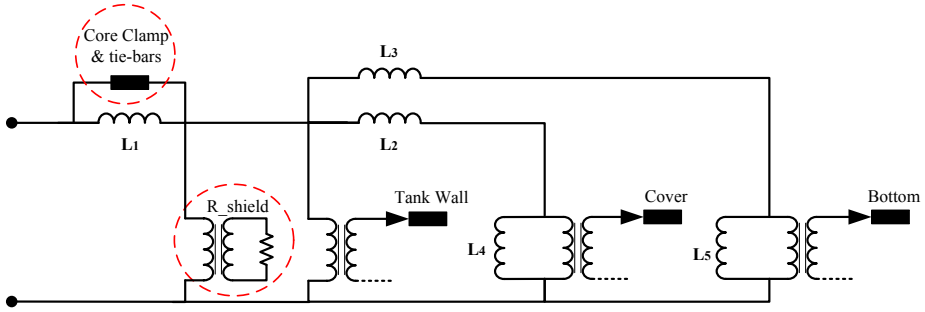

b) The magnetic shield and the core clamp/tie-bars added to the presented off-core model

Figure 8.1 Future developments of the off-core model proposed in the thesis to include the core clamps, tie bars, magnetic shields and magnetic shunts

Bibliography

[1] M. Heathcote, J&P Transformer Book, Newnes, 2007.

[2] S. V. Kulkarni and S. A. Khaparde, Transformer engineering: design, technology, and diagnostics, CRC Press, Taylor and Francis Group, 2012.

[3] NERC, "Effects of geomagnetic disturbances on the bulk power system," North American Electric Reliability Corporation (NERC), Atlanta, 2012.

[4] J. G. Kappenman and V. D. Albertson, "Geomagnetic storms and their impact on power systems," *IEEE Power Engineering Review,* 1996.

[5] D. H. Boteler, R. J. Pirjola and H. Nevanlinna, "Effects of geomagnetic disturbances on electrical systems at the earth's surface," *Advances in Space Research,* vol. 22, pp. 17-27, 1998.

[6] A. Vilianen and R. Pirjola, "Finnish geomagnetically induced currents project," *IEEE Power Engineering Review,* vol. 15, pp. 20-21, 1995.

[7] P. R. Price, "Geomagnetically induced current effects on transformers," *IEEE Trans. Power Delivery,* vol. 17, no. 4, pp. 1002-1008, 2002.

[8] L. Trichtchenko and D. H. Boteler, "Response of power systems to the temporal characteristics of geomagnetic storms," in *Canadian Conference on Electrical and Computer Engineering*, Ottawa, Canada, 2006.

[9] J. . E. Berge, *Impact of geomagnetically induced currents on power transformers,* London, Ontario, Canada: Electronic Thesis and Dissertation Repository. 132, Western University, http://ir.lib.uwo.ca/etd/132, 2011.

[10] N. Takasu, "An experimental analysis of DC excitation of transformers bygeo-magnetic induced currents," *IEEE Trans. Power Delivery,* vol. 9, no. 2, pp. 1173-1182, 1994.

[11] L. Marti, A. Rezaei-Zare and A. Narang, "Simulation of transformer hot-spot heating due to geomagnetically induced currents," *IEEE Trans. Power Delivery,* vol. 28, no. 1, pp. 320-327, 2013.

[12] S. Mousavi, *Electromagnetic modelling of power transformers with dc magnetization,* Stockholm: KTH university, PhD thesis, QC 20121121, 2012.

[13] F. Sui, A. Rezaei-Zare, M. Kostic and P. Sharma, "A method to assess GIC impact on zero sequence overcurrent protection of transmission lines," in *IEEE Power & Energy*

Society General Meeting, Vancouver, 2013.

[14] N. Chiesa , A. Lotfi, H. K. Hoidalen, B. Mork, Ø. Rui and T. Ohnstad, "Five-leg transformer model for GIC studies," in *International Power Systen Transient Conference* , Vancouver, 2013.

[15] R. Girgis and K. Vedante, "Effects of GIC on power transformers and power systems," in *Transmission and Distribution Conference and Exposition, IEEE PES*, Orlanda, 2012.

[16] SIEMENS, "GIC effects on power transformers," NERC Taskforce GMDTF Meeting, Atlanta, USA, 2013.

[17] R. S. Girgis and K. B. Vedante, "Impact of GICs on power transformers: overheating is not the real issue," *IEEE Electrification Magazine,* vol. 3, no. 4, pp. 8-12, 2015.

[18] S. Guillon, P. Toner, L. Gibson and D. Boteler, "A colorful blackout," *IEEE power and Energy magazine,* vol. 14, no. 6, pp. 59-71, 2016.

[19] R. Horton, S. Dahman, T. Overbye and R. Walling, "Magnetohydrodynamic electromagnetic pulse assessment of the continental U.S. electric grid-geomagnetically induced current and transformer thermal analysis," EPRI, 3002009001, Palo Alto, CA, 2017.

[20] B. Røen, *Master thesis-geomagnetic induced current effects on power transformers,* Trondheim: Norwegian Univeristy of Science and Technology (NTNU), 2016.

[21] A. Greenwood, Electrical transients in power systems, Newyork: John Wiley and Sons, Inc., 1971.

[22] H. K. William, H. P. W and C. Wayne, "A new approach to modeling three-phase transformer connections," *IEEE TRANS. INDUSTRY APPLICATIONS,* vol. 35, no. 1, pp. 169-175, 1999.

[23] IEC std. 60076-1, *Power transformers, Part 1: General,* International Electrotechnical Commission, 2011.

[24] C57.12.90, IEEE standard test code for liquid-immersed distribution, power and regulating transformers, IEEE Standard, 2010.

[25] A. Carlson, J. Fuhr, G. Schemel and F. Wegscheider, Testing of power transformers: routine tests, type tests and special tests, Zurich: ABB AG, 2003.

[26] A. Ramos and J. C. Burgos, "Influence of tertiary stabilizing windings on zero-sequence performance of three-phase three-legged YNynd transformers. Part I: Equivalent circuit models," *Electric Power System Research ,* vol. 144, pp. 32-40,

2017.

[27] A. Ramos and J. C. Burgos, "Influence of tertiary stabilizing windings on zero-sequence performance of three-phase three-legged YNynd transformers. Part II: Tank overheating hazard and short-circuit duty," *Electric Power System Research,* vol. 145, pp. 149-156, 2017.

[28] E. Sorrentino and J. C. Burgos, "Comparison of methods for measuring zero sequence impedances in 3-phase core-type transformers," in *International Universities Power Engineering Conference (UPEC)*, London, 2012.

[29] M. Kamel, H. Saeed, A. Karrar, A. Eltom, M. Bowman, T. Womack and P. Cooper, "On-site low voltage determination of zero sequence impedances for station auxiliary transformers," in *IEEE Power and Energy Society General Meeting (PESGM)*, Boston, 2016.

[30] G. Rosselli, "Transformer test to calculate Z0 for interconnected windings transformers using symmetrical sequence components," in *IEEE Power Engineering Society General Meeting*, San Francisco, 2005.

[31] F. Sulla and O. Samuelsson, "Estimation of the zero sequence voltage on the D-Side of a DY transformer by using one voltage transformer on the D-Side," in *IET 9th International Conference on Developments in Power System Protection (DPSP)*, Glasgow, 2008.

[32] A. Ramos, J. C. Burgos, A. Moreno and E. Sorrentino, "Determination of parameters of zero-sequence equivalent circuits for three-phase three-legged YNynd transformers based on onsite low-voltage tests," *IEEE Trans. power delivery,* vol. 28, no. 3, pp. 1618-1625, 2013.

[33] A. Lotfi, Zero sequence impedance calculation of different transformers with using 3D-FEM, Zanjan: University of Zanjan, Master thesis, 2007.

[34] R. Allcock, S. Holland and L. Haydock, "Calculation of zero phase sequence impedance for power transformers using numerical methods," *IEEE Trans. Magnetics,* vol. 31, no. 3, pp. 2048 - 2051, 1995.

[35] S. Elmer and J. C. Burgos, "Application of 2D linear models for computing zero-sequence magnetizing impedances of 3-phase core-type transformers," *Electric Power System research ,* vol. 117, pp. 123-133, 2014.

[36] T. Ngnegueu, M. Mailhot, A. Munar and M. Sacotte, "Zero phase sequence impedance and tank heating model for three phase three leg core type power transformers coupling magnetic field and electric circuit equations in a finite element software," *IEEE Trans magnetics,* vol. 31, no. 3, pp. 2068 - 2071, 1995.

[37] P.-D. Patricia, A.-M. Casimiro and M. L.-F. Xose, "Transformer tertiary stabilizing windings part II: overheating hazard on tank walls," in *International Conference on Electrical Machines*, Marsielle, 2012.

[38] A. Eyup and S. Dilara, "Calculation of zero sequence inductance of a three-phase reactor," in *International Conference on Electrical and Electronics Engineering (ELECO)*, Bursa, 2017.

[39] S. Elmer and C. B. Juan, "Rules to estimate the expected values of zero-sequence impedances in 3-phase core-type transformers," *Electric Power System Research ,* vol. 165, pp. 94-101, 2018.

[40] IEC std. 60076-8, *Power transformers, Part 8: Application guide,* International Electrotechnical Commission, 2011.

[41] S. Elmer and C. B. Juan, "About the difference between zero-sequence magnetizing impedances of a 3-phase core-type transformer," *Electric Power System Reseach (EPSR),* vol. 116, pp. 439-443, 2014.

[42] N. Chiesa, Power transformer modeling for inrush current calculation, Trondheim: PhD thesis at Norwegian University of Science and Technology (NTNU), 2010.

[43] D. L. Stuehm, B. A. Mork and D. D. Mairs, "Five-legged core transformer equivalent circuit," *IEEE Trans. Power delivery,* vol. 4, no. 3, pp. 1786-1793, 1989.

[44] J. A. Martinez and B. A. Mork, "Transformer modeling for low- and mid-frequency transients—a review," *IEEE Trans. Power delivery,* vol. 20, no. 2, pp. 1625-1632, 2005.

[45] F. de Leon and A. Semlyen, "Complete transformer model for electromagnetic transients," *IEEE Trans. Power Delivery,* vol. 9, no. 1, pp. 231-239, 1994.

[46] E. C. Cherry, "The duality between interlinked electric and magnetic circuits and the formation of transformer equivalent circuits," *Proceedings of the Physical Society. Section B,* vol. 62, pp. 101-111, 1949.

[47] A. P. Morando and S. Leva, "Topological transition from magnetic networks to the electric equivalent ones when iron losses are present," in *43rd IEEE Midwest Symposium on Circuits and Systems*, 2000.

[48] G. R. Slemon, "Equivalent circuits for transformers and machines including non-linear effects," *Proceedings of the Institution of Electrical Engineers,* vol. 100, no. 1, pp. 129-153, 1953.

[49] S. Jazebi, S. E. Zirka, M. Lambert, A. Rezaei-Zare, N. Chiesa, Y. Moroz, X. Chen, M. Martinez-Duro, C. M. Arturi, E. P. Dick, A. Narang, R. A. Walling, J. Mahseredjian, J.

A. Martinez and F. de León, "Duality derived transformer models for low-frequency electromagnetic transients—part I: topological models," *IEEE Trans. Power Delivery,* vol. 31, no. 5, pp. 2410-2419, 2016.

[50] S. Jazebi, S. E. Zirka, M. Lambert, A. Rezaei-Zare, N. Chiesa, Y. Moroz, X. Chen, M. Martinez-Duro, C. M. Arturi, E. P. Dick, A. Narang, R. A. Walling, J. Mahseredjian, J. A. Martinez and F. de León, "Duality-derived transformer models for low-frequency electromagnetic transients—part II: complementary modeling guidelines," *IEEE Trans. Power Delivery,* vol. 31, no. 5, pp. 2420-2430, 2016.

[51] S. E. Zirka, Y. I. Moroz, H. K. Høidalen, A. Lotfi, N. Chiesa and C. M. Arturi, "Practical experience in using a topological model of a core-type three-phase transformer—no-load and inrush conditions," *IEEE Trans. Power Delivery,* vol. 32, no. 4, pp. 2081-2090, 2017.

[52] W. Watson and E. P. Dick , "Transformer models for transient studies based on field measurement," *IEEE Trans. Power Delivery,* Vols. PAS-100, no. 1, pp. 401-419, 1981.

[53] C. M. Arturi, "Transient simulation and analysis of a five-limb generator step-up transformer following an out-of-phase synchronization," *IEEE Trans. Power Delivery,* vol. 6, no. 1, pp. 196-207, 1991.

[54] A. Narang and R. H. Brierley, "Topology based magnetic model for steady-state and transient studies for three phase core type transformers," *IEEE Trans. Power delivery ,* vol. 9, no. 3, pp. 1337-1349, 1994.

[55] B. A. Mork, "Five-legged wound-core transformer model: Derivation, parameters, implementation, and evaluation," *IEEE Trans. Power Delivery,* vol. 14, no. 4, pp. 1519-1526, 1999.

[56] R. Yacamini and H. Bronzead, "Transformer inrush calculations using a coupled electromagnetic model," *IEE Proc. Inst. Elect. Eng., Sci. Meas.,* vol. 141, pp. 491-498, 1994.

[57] J. Arrillaga, W. Enright, N. R. Watson and A. R. Wood, "Improved simulation of HVDC converter transformers in electromagnetic transient programs," *IEE Proc. Inst. Elect. Eng., Gen. Transm. Distrib.,* vol. 144, pp. 100-106, 1997.

[58] E. Fuchs and Y.You, "Measurement of lamda-i characteristics of asymmetric three-phase transformers and their applications," in *Ninth International Conference on Harmonics and Quality of Power. Proceedings*, Orlando, USA, 2000.

[59] B. A. Mork, F. Gonzalez, D. Ishchenko, D. L. Stuehm and J. Mitra, "Hybrid transformer model for transient simulation—part II: laboratory measurements and

benchmarking," *IEEE Trans. Power Delivery,* vol. 22, no. 1, pp. 256-262, 2007.

[60] B. A. Mork, F. Gonzalez, D. Ishchenko, D. L. Stuehm and J. Mitra, "Hybrid transformer model for transient simulation-part I: development and parameters," *IEEE Trans. Power Delivery,* vol. 22, no. 1, pp. 248-255, 2007.

[61] H. K. Hoidalen, B. A. Mork, F. Gonzalez , D. Ishchenko and N. Chiesa, "Implementation and verification of the hybrid transformer model in ATPDraw," *Electric Power System Reseach,* vol. 79, no. 3, pp. 454-459, 2009.

[62] V. Brandwajn, H. Donnel and I. Dommel, "Matrix representation of three-phase N-winding transformers for steady-state and transient studies," *IEEE TRPAS, PAS-101,* pp. 1369-1378, 1982.

[63] B. A. Mork, F. Gonzalez and D. Ishchenko, "Leakage inductance model for autotransformer transient simulation," in *International Conference on Power Systems (IPST)*, Montreal, 2005.

[64] H. K. Høidalen, N. Chiesa, A. Avendaño and B. A. Mork, "Developments in the hybrid transformer model – Core modeling and optimizations," in *International Conference on Power Systems (IPST)*, Delft, 2011.

[65] A. Avendaño, B. A. Mork, D. Ishchenko and F. Gonzalez, "Advanced leakage inductance model for transformer transient simulation," in *EEE Power & Energy Society General Meeting (PESGM)*, Portland, 2018.

[66] F. de León and J. A. Martinez, "Dual three-winding transformer equivalent circuit matching leakage measurements," *IEEE Trans. Power Delivery,* vol. 24, no. 1, pp. 160-168, 2009.

[67] S. Jazebi, F. de León, A. Farazmand and D. Deswal, "Dual reversible transformer model for the calculation of low-frequency transients," *IEEE Trans. Power Delivery,* vol. 28, no. 4, pp. 2509-2517, 2013.

[68] S. Jazebi and F. de León, "Duality-based transformer model including eddy current effects in the windings," *IEEE Trans. Power Delivery,* vol. 30, no. 5, pp. 2312-2320, 2015.

[69] S. E. Zirka, Y. I. Moroz and C. M. Arturi, "Accounting for the Influence of the tank walls in the zero-sequence topological model of a three-phase three-Limb transformer," *IEEE Trans. Power Delivery,* vol. 29, no. 5, pp. 2172-2179, 2014.

[70] S. E. Zirka, Y. I. Moroz, A. J. Moses and C. M. Arturi, "Static and dynamic hysteresis models for studying transformer transients," *IEEE TRANS. POWER DELIVERY,* vol. 26, no. 4, pp. 2352-2362, 2011.

[71] S. E. Zirka , Y. I. Moroz and E. Rahimpour, "Towards a transformer transient model as a lumped-distributed parameter system," *COMPEL - The international journal for computation and mathematics in electrical and electronic engineering,* vol. 36, no. 3, pp. 741-750, 2017.

[72] A. Rezaei-Zare, "Enhanced transformer model for low- and mid-frequency transients—part I: model development," *IEEE Trans. Power Delivery,* vol. 30, no. 1, pp. 307-315, 2015.

[73] A. Rezaei-Zare, "Enhanced transformer model for low and mid-frequency transients—part II: validation and simulation results," *IEEE Trans. Power Delivery,* vol. 30, no. 1, pp. 316-325, 2015.

[74] WG A2.38, "TB659-Transformer thermal modeling," Cigre, ISBN 978-2-85873-362-0, 2016.

[75] S. T. M. Djamali, "Hundred years of experience in the dynamic," *The institute of Engineering and Technilogy,* vol. 11, no. 11, pp. 2731-2739, 2016.

[76] A. Najafi and I. Iskender, "An improved thermal model for distribution transformer underunbalanced voltage conditions," *International Journal of Thermal Sciences,* vol. 104, pp. 373-385, 2016.

[77] J. F. Lindsay, "Temperature rise of an oil-filled transformer with varying load," *IEEE Trans. Power Apparatus and Systems,* Vols. PAS-103, no. 9, pp. 2530-2536, 1984.

[78] N. Chiesa and H. K. Hoidalen, "Hysteretic iron-core inductor for transformer inrush current modeling in EMTP," in *Power System Computation Conference (PSCC)*, Glasgow, Scotland, 2008.

[79] J. Lammeraner and M. Stafl, Eddy currents, London: Iliffe Books Ltd., 1966.

[80] Y. Sakaki and S.-i. Imagi, "Relationship among eddy current loss, frequency, maximum flux density and a new parameter concerning the number of domain walls in polycrystalline and amorphous soft magnetic materials," *IEEE Trans. Magnetic,* vol. 17, pp. 1478-1480, 1981.

[81] G. Bertotti, Hysteresis in magnetism: for physicists, materials scientists, and engineers, Academic Press, 1998.

[82] G. Bertotti, "Space-time correlation properties of the magnetization process and eddy current losses: Theory," *Journal of Applied Physics,* vol. 54, p. 5293, 1983.

[83] W. Chandrasena, P. G. McLaren, U. D. Annakkage and R. P. Jayasinghe, "An improved low-frequency transformer model for use in GIC studies," *IEEE TRANS.*

POWER DELIVERY, vol. 19, no. 2, pp. 643-651, 2004.

[84] S. Magdaleno-Adame, J. C. Olivares-Galvan, R. Escarela, O. Raichenko and A. G. Kladas , "Hot Spots Mitigation on Tank Wall of a Power Transformer using Electromagnetic Shields," in *International Conference on Electrical Machines (ICEM)*, Berlin, 2014.

[85] R. SITAR and Ž. JANIĆ, "Determination of local losses and temperatures in power transformer tank," *Journal of Energy,* vol. 67, no. 3, pp. 9-13, 2018.

[86] J. H. L. IV and J. H. L. V, A Heat transfer textbook, Forth Edition, Newyork, USA: Dover Publication Inc., 2011.

[87] F. P. Incropera, D. P. DeWitt, T. L. Bergman and A. S. Lavine, Fundamentals of Heat and Mass Transfer, John Wiley & Sons Inc., 2007.

[88] A. Bar-Kohen and W. M. Rohsenow, "Thermally optimum spacing of vertical natrual convection cooled parallel plates," *Transaction of the american society of mechanical engineering,* vol. 106, no. 1, pp. 116-123, 1984.

[89] M. Ahmadi, M. Fakoor-Pakdaman and M. Bahrami, "Natural convection from vertical parallel plates: an integralmethod solution," *Journal of Thermophysics and Heat Transfer,* vol. 29, no. 1, pp. 140-149, 2015.

[90] P. GHOSHDASTIDAR, Heat transfer, New Delhi, India: Oxford university press, 2012.

[91] I. Faria, R. Salustiano and M. Martinez, "A prediction of distribution transformers aging based on tank infrared temperature measurements," in *International Conference on Electricity Distribution (22nd)*, Stockhom, Sweden, 2013.

[92] Y. Shabany, "Radiation heat transfer from plate-fin heat sinks," in *24th Annual IEEE Semiconductor Thermal Measurement and Management Symposium*, San Jose, CA, USA, 2008.

[93] B. Yazıcıoğlu, Performance of rectangular fins on a vertical base in free convection heat transfer, Ankara: MIDDLE EAST TECHNICAL UNIVERSITY, 2005.

[94] R. Siegel and J. Howell, Thermal radiation heat transfer, Tokyo: McGraw-Hill, 1972.

[95] "Rautaruukki Corporation," [Online]. Available: http://www.ruukki.com/Steel/Hot-rolled-steels. [Accessed 2015].

[96] "Rautaruukki Corporation," [Online]. Available: http://www.ruukki.com/Steel/Cold-rolled-steels. [Accessed 2015].

[97] "Brockhaus Measurement," 2018. [Online]. Available: https://brockhaus.com/measurements/products/softmagnetic/est-series/mpg-100/.

[98] IEC 60404-3, "Magnetic materials - Part 3: Methods of measurement of the magnetic properties of magnetic sheet and strip by means of a single sheet tester," International Electrotechnical Commission, 1992.

[99] S. E. Zirka, Y. Moroz, P. Marketos and A. Moses, "Loss separation in non-oriented electrical steels," *IEEE Trans. Magnetics,* vol. 46, no. 2, pp. 286-289, 2010.

[100] A. Lotfi, H. K. Hans, E. Agheb and A. Nysveen, "Characterization of magnetic losses in the transformer tank steel," *IEEE Trans. Magnetics,* vol. 52, no. 5, p. 6301104, 2015.

[101] S. E. Zirka, Y. Moroz, P. Marketos and A. Moses, "Viscosity-based magnetodynamic model of soft magnetic materials," *IEEE Trans. Magnetics,* vol. 42, no. 9, pp. 2121-2132, 2006.

[102] J. Chen, D. Wang, S. Cheng, Y. Wang, Y. Zhu and Q. Liu, "Modeling of temperature effects on magnetic property of non-oriented silicon steel lamination," *IEEE Trans. Magnetics,* vol. 51, no. 11, 2015.

[103] D. Negre and M. Gotti, *Transformer model benchmarking,* Milano: Master thesis in Electrical Engineering, Politecnico di Milano, 2007.

[104] Ansys, [Online]. Available: https://www.ansys.com/products/electronics/ansys-maxwell. [Accessed 15 November 2018].

[105] C. Álvarez-Mariño, F. de León and X. M. López-Fernández, "Equivalent Circuit for the Leakage Inductance of Multiwinding Transformers: Unification of Terminal and Duality Models," *IEEE Trans. Power Delivery,* vol. 27, no. 1, pp. 353-361, 2012.

[106] N. G. T. Force, "Application guid, computing geomagnetically-induced current in the bulk-power System," North American Reliability Corporation (NERC), Atlanta, USA, December, 2013.

[107] A. Schellmanns, J. P. Keradec and J. L. Schanen, "Electrical equivalent circuit for frequency dependant impedance: minimum lumped elements for a given precision," in *Annual Meeting and World Conference on Industrial Applications of Electrical Energy*, Rome, Italy, 2000.

[108] B. A. Mork, F. Gonzalez, D. Ishchenko, D. L. Stuehm and M. Joydeep , "Hybrid transformermodel for transient simulation: Part I: development and parameters," *IEEE Trans. Power Delivery,* vol. 22, no. 1, pp. 248-255, 2007.

[109] J. H. Lienhard, A Heat Transfer Textbook, Massachusetts: Phlogiston press Cambridge, 2017.

[110] D. Susa, M. Lehtonen and H. Nordman, "Dynamic thermal modelling of power transformers," *IEEE Trans. Power Delivery,* vol. 20, no. 1, pp. 197 - 204, 2005.

Appendix 1

In the following formulas, θ is temperature in °C and p is the atmospheric pressure in mmHg [109] [110] [74].

Air physical properties:

1. Density [kg/m3]

   $(1.2722 - 0.0049175\,\theta + 0.000019709\,\theta^2 - 0.00000004382\,\theta^3)(\frac{p}{760})$

2. Kinematic viscosity [m/s^2]

   $(0.000013373 + 0.000000086408\,\theta + 0.00000000010711\,\theta^2)(\frac{760}{p})$

3. Thermal expansion coefficient [1/ °C]

   $0.0036581 - 0.00001427\,\theta + 0.000000059234\,\theta^2 - 0.00000000013609\,\theta^3$

4. Thermal conductivity [W/m °C]

   $0.024465 + 0.000076664\,\theta - 0.000000024834\,\theta^2$

5. Specific heat capacity [Ws/kg °C]

   $1006 + 0.05\,\theta$

Oil physical properties:

1. Density

   $1098.72 - 0.712\,\theta$

2. Kinetic viscosity

   $0.08467 - 0.0004\,\theta + 5 \times 10^{-7}\,\theta^2$

3. Thermal expansion coefficient

   0.00086

4. Thermal conductivity

   $0.1509 - 7.101 \times 10^{-5}\,\theta$

5. Specific heat capacity

   $807.163 + 3.5\,\theta$

Appendix 2

The equivalent circuit of the off-core path when only the wall and the bottom are considered is shown in Figure A2.1. The black boxes are the wall and the bottom models, which are discussed in detail in Chapter 3, Section 3.3. This circuit is coupled to the thermal equations through the losses in the wall and the bottom with the approach presented in Chapter 3, Section 3.4.

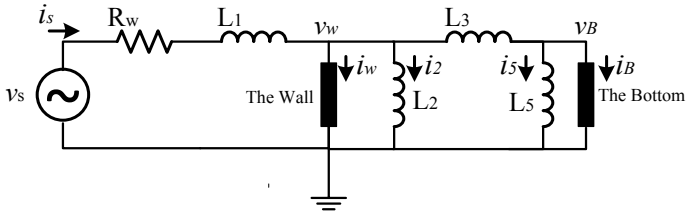

Figure A2.1 Circuit diagram of the off-core path with only the wall and the bottom included

From the circuit topology, it can be written as:

$$v_w = v_s - R_w i_s - L_1 \frac{di_s}{dt} \tag{A2.1}$$

$$v_B = v_w - L_3\left(\frac{di_5}{dt} + \frac{di_B}{dt}\right) \tag{A2.2}$$

$$v_B = L_5 \frac{di_5}{dt} \tag{A2.3}$$

$$v_w = L_2 \frac{di_2}{dt} \tag{A2.4}$$

$$i_s = i_w + i_2 + i_B + i_5 \tag{A2.5}$$

$$\frac{di_s}{dt} = \frac{di_w}{dt} + \frac{di_2}{dt} + \frac{di_B}{dt} + \frac{di_5}{dt} \tag{A2.6}$$

Substituting (A2.3) in (A2.2) results in:

$$v_B = v_w - L_3\left(\frac{v_B}{L_5} + \frac{di_B}{dt}\right) \rightarrow \left(1 + \frac{L_3}{L_5}\right) v_B = v_w - L_3 \frac{di_B}{dt} \rightarrow$$
$$v_B = \left(\frac{L_5}{L_5+L_3}\right) v_w - \left(\frac{L_5 L_3}{L_5+L_3}\right) \frac{di_B}{dt} \tag{A2.7}$$

Substituting (A2.6) and (A2.5) in (A2.1) and using (A2.3) and (A2.4), it follows:

$$v_w = v_s - R_w\left(i_w + \frac{1}{L_2}\int v_w + i_B + \frac{1}{L_5}\int v_B\right) - L_1\left(\frac{di_w}{dt} + \frac{v_w}{L_2} + \frac{di_B}{dt} + \frac{v_B}{L_5}\right) \tag{A2.8}$$

Figure A2.2 shows the implementation of this equation in MATLAB-SIMULINK. The currents i_w and i_B are obtained through the wall and the bottom models, as shown in Figure A2.3-a and Figure A2.3-c. The thermal model is shown in Figure A2.3-b and Figure A2.3-d. As can be seen, the power losses in the wall and the bottom are calculated with formula $\int_t^{t+20\mu s} v_w \cdot i_w dt$ and $\int_t^{t+20\,\mu s} v_B \cdot i_B dt$ where 20 µs is the fundamental period of the 50 Hz voltage, that are used as inputs for thermal models. The total losses of the circuit are also calculated with $\int_t^{t+20\mu s} v_s \cdot i_s dt$.

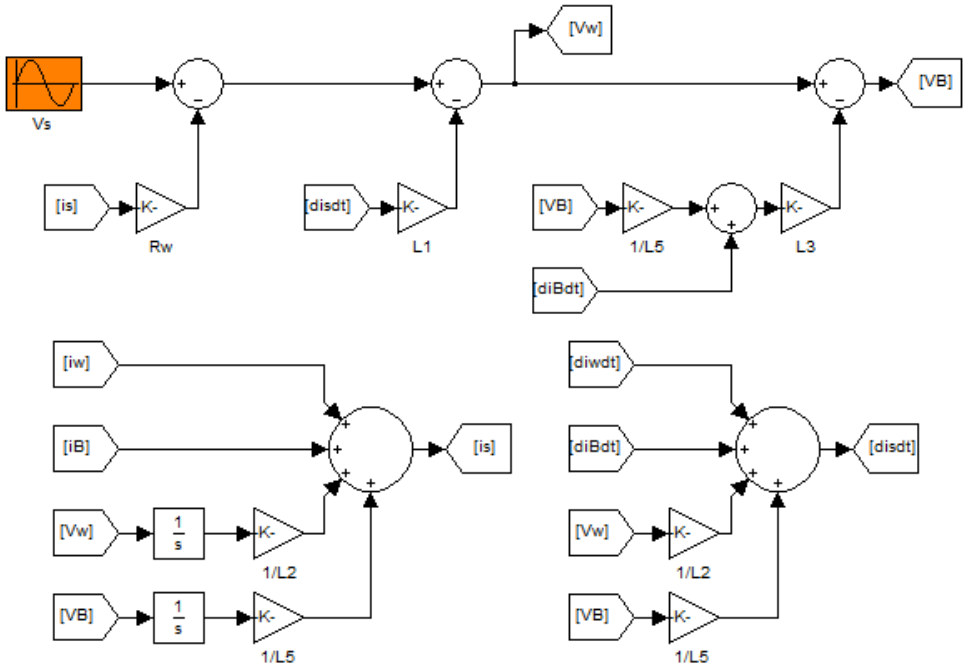

Figure A2.2 Implementation of (A2.8) in MATLAB-SIMULINK

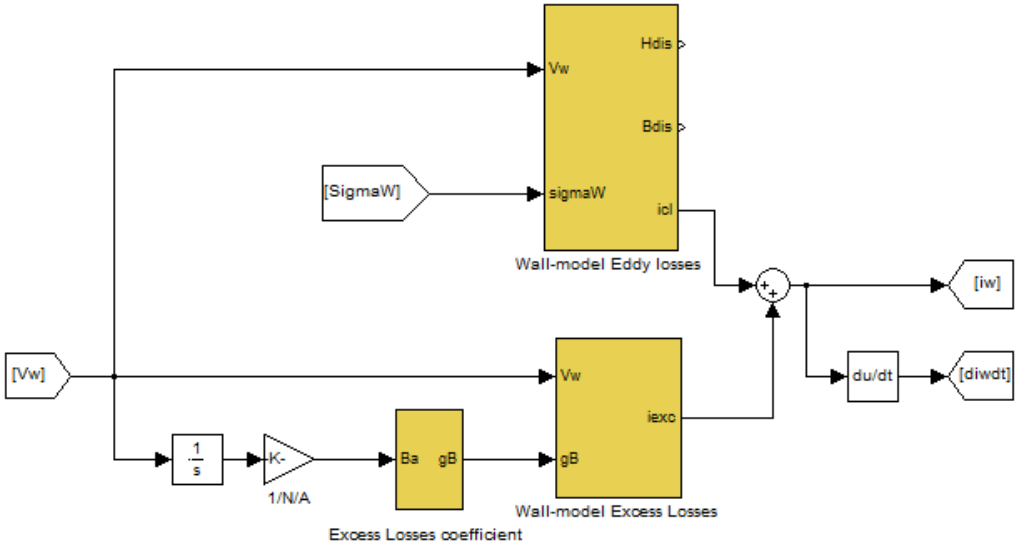

a) The classical eddy current and the excess losses model of the wall

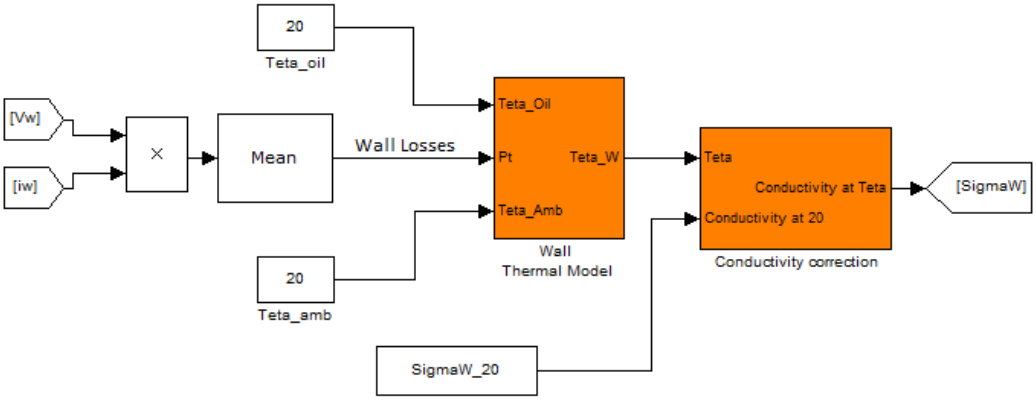

b) Thermal model of the wall

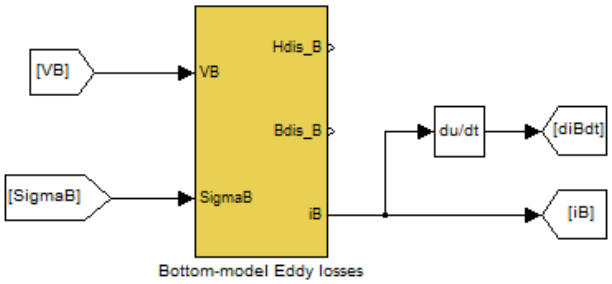

c) The classical eddy current model of the bottom

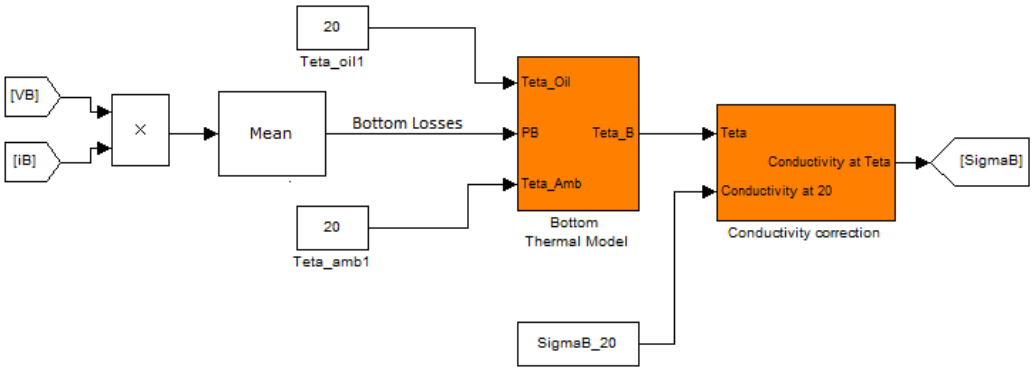

d) Thermal model of the Bottom

Figure A2.3 Implementation of the circuit Figure A2.1 together with thermal equations in MATLAB-SIMULINK

Appendix 3

I. Calculation of SC-ZS inductance using 3D-FEM

The inductance matrix of the windings is calculated with 3D-FEM and expressed with $\bar{L}=\begin{bmatrix} [\bar{L}_{HV}]_{3\times3} & [\bar{L}_{HV\text{-}LV}]_{3\times3} \\ [\bar{L}_{LV\text{-}HV}]_{3\times3} & [\bar{L}_{LV}]_{3\times3} \end{bmatrix}_{6\times6}$ (see Section 5.1.3). Using the inverse matrix $\bar{L}^{-1} = \bar{\Gamma}$, the current of the excited phases can be expressed by following equations.

The HV side excited with V_0 and the LV side is short-circuited:

$$DI_i = \Gamma_{i1} \cdot V_0 + \Gamma_{i2} \cdot V_0 + \Gamma_{i3} \cdot V_0 \rightarrow \Gamma^0_{sc,HV,i} = \Gamma_{i1} + \Gamma_{i2} + \Gamma_{i3},\ i = 1..3 \quad \text{(A3.1)}$$

Using the same method for the excited LV side, it follows:

$$\Gamma^0_{sc,LV,i} = \Gamma_{i4} + \Gamma_{i5} + \Gamma_{i6},\ i = 4..6 \quad \text{(A3.2)}$$

where Γ_{ik} is the element of i^{th} row and k^{th} column of the $\bar{\Gamma}$, I_i is the current of the i^{th} winding, $\Gamma^0_{sc,HV,i}$ and $\Gamma^0_{sc,LV,i}$ (of phase i) are the inverse SC-ZS inductance seen from HV and from LV sides, respectively.

II. Calculation of SC-ZS impedance using the equivalent circuit

The SC-ZS impedance is calculated for each simulation of Case 1 through Case 5 with the equations given in Table A3.1. In these cases, the off-core inductances are linear, and the input inductance can be analytically obtained. All the parameters are referred to the exciting side. When the non-linear models of the tank walls are included, the overall circuits of Figure 6.11 and Figure 6.12 are used for calculation of the SC-ZS impedance and losses.

Table A3. 1 Calculation of the SC-ZS inductance for the lossless models

	Equivalent circuit	Equation
LV	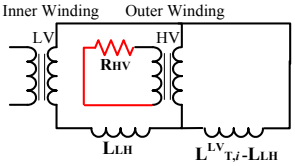	$L^0_{sc,LV,i} = L_{LH} + \frac{(L^{LV}{}_{T,i} - L_{LH}) R'^{2}_{HV}}{\omega^2 (L^{LV}{}_{T,i} - L_{LH})^2 + R'^{2}_{HV}}$ $R^0_{sc,LV,i} = R_{LV} + \frac{\omega^2 (L^{LV}{}_{T,i} - L_{LH})^2 R'_{HV}}{\omega^2 (L^{LV}{}_{T,i} - L_{LH})^2 + R'^{2}_{HV}}$
HV	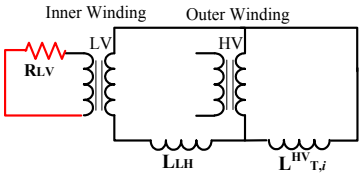	$L^0_{sc,HV,i} = \frac{\omega^2 L^{HV}{}_{T,i} L_{LH} (L^{HV}{}_{T,i} + L_{LH}) + L^{HV}{}_{T,i} R'^{2}_{LV}}{\omega^2 (L^{HV}{}_{T,i} + L_{LH})^2 + R'^{2}_{LV}}$ $R^0_{sc,HV,i} =$ $R_{HV} +$ $\frac{\omega^2 (L^{HV}{}_{T,i} (L^{HV}{}_{T,i} + L_{LH}) R'_{LV} - L^{HV}{}_{T,i} L_{LH} R'_{LV})}{\omega^2 (L^{HV}{}_{T,i} + L_{LH})^2 + R'^{2}_{LV}}$

III. Calculation of SC-PS inductance using 3D-FEM

Using the reverse inductance matrix $\bar{\Gamma} = \bar{L}^{-1} = \begin{bmatrix} [\bar{L}_{HV}]_{3\times3} & [\bar{L}_{HV-LV}]_{3\times3} \\ [\bar{L}_{LV-HV}]_{3\times3} & [\bar{L}_{LV}]_{3\times3} \end{bmatrix}^{-1}_{6\times6}$, the current of the winding i at HV side is:

$$DI_i = \sum_{k=1}^{6} \Gamma_{ik} \cdot V_k \,, i = 1..3 \tag{A3.3}$$

Having symmetrical three-phase voltage applied to HV side ($V_1 + V_2 + V_3 = 0 \rightarrow V_2 + V_3 = -V_1$) and short circuit at LV side ($V_4 = V_5 = V_6 = 0$), the current of phase 1 is expressed as:

$$DI_1 = \Gamma_{11} \cdot V_1 - (\Gamma_{12} + \Gamma_{13}) \cdot V_1 \rightarrow \Gamma^{+}_{sc,HV,1} = \Gamma_{11} - (\Gamma_{12} + \Gamma_{13}) \tag{A3.4}$$

On the same way, $\Gamma^{+}_{sc,HV,2} = \Gamma_{22} - (\Gamma_{21} + \Gamma_{23})$ and $\Gamma^{+}_{sc,HV,3} = \Gamma_{33} - (\Gamma_{31} + \Gamma_{32})$.

For the LV side PS inductances, following the same approach:

$$\Gamma^{+}_{sc,LV,4} = \Gamma_{44} - (\Gamma_{45} + \Gamma_{46})$$

$$\Gamma^{+}_{sc,LV,5} = \Gamma_{55} - (\Gamma_{54} + \Gamma_{56}) \tag{A3.5}$$

$$\Gamma^{+}_{sc,LV,6} = \Gamma_{66} - (\Gamma_{65} + \Gamma_{64})$$